

Collective behavior of biological aggregates

Author

Rafael González Albaladejo

A dissertation submitted in partial fulfillment of the
requirements for the degree of Doctor of Philosophy in

Mathematical Engineering

Universidad Carlos III de Madrid

Advisors

Luis L. Bonilla

Ana Carpio

March 2023

This thesis is distributed under license “Creative Commons **Atribution - Non Commercial - Non Derivatives**”.



A mi familia

Acknowledgements

No hay mejor manera de terminar una tesis que recordar y agradecer todo lo pasado. Aunque cueste plasmar las emociones en palabras, en las siguientes líneas voy a intentar expresar mi agradecimiento.

Antes que nada, me gustaría mencionar que esta tesis se ha realizado durante la pandemia de Covid-19. Quiero poner en valor el esfuerzo de todas aquellas personas que han contribuido a que el trabajo siga adelante pese al confinamiento y todas sus dificultades. La importancia del avance tecnológico y científico se ha visto evidenciada como nunca antes. No puedo continuar sin recordar a una gran persona, padre y abuelo que nos dejó por culpa de la pandemia: mi abuelo Pepe. Una persona que solo me ha mostrado cosas buenas de la vida. Sobre todo, gracias por enseñarme a querer y amar como tú lo hacías.

A mis supervisores, maestros y directores de tesis: Ana Carpio y Luis Bonilla. Gracias por confiarme este proyecto. Habéis puesto a mi disposición todos vuestros conocimientos, que no son pocos, y a través del trabajo que realizáis me habéis inculcado vuestra pasión por la ciencia. En definitiva, me habéis concedido recursos para moverme en un campo que me apasiona.

Agradezco el apoyo del Ministerio de Economía y Competitividad de España a través de las ayudas del programa de Formación de Doctores, PRE2018-083807, cofinanciada por el Fondo Social Europeo. También agradezco al apoyo de FEDER /Ministerio de Ciencia, Innovación y Universidades - Agencia Estatal de Investigación por medio de los proyectos MTM2017-84446-C2-1-R y PID2020-112796RB-C21. Gracias a ello y a mis supervisores, he podido ir a diferentes congresos internacionales y asistir a cursos importantes en mi campo de estudio.

Special thanks for the three-month stay in the Physics of Complex Biosystems group of the Institute for Theoretical Physics at the University of Heidelberg. Thanks to Professor Ulrich Schwarz for accepting me into his group, for his kindness and for opening

the doors for me to learn from the best researchers in this field. Without a doubt, I will remember this stay as one of the best experiences of my life thanks to Professor Falko Ziebert, my tutor at the University of Heidelberg. Thank you for your teachings and conversations, and for working and collaborating with me on such an interesting project. But, above all, thank you for welcoming me as you did, for helping me as much as possible in my first stay outside Spain, for introducing me to new people and for making me feel at home. Also, I thank my fellow students Robert, Dennis and Jaime for the time spent with me and for the valuable and interesting conversations.

A mi familia. A lo más importante de mi vida. Gracias a vosotros soy lo que soy. Esta tesis obviamente es un logro de todos. Si no fuese por mi feliz infancia, la educación que me habéis dado, todas las enseñanzas vitales y guiarme como lo habéis hecho, no hubiese conseguido este gran hito. Soy gracias a lo que somos, y cada logro individual que consiga será una mera representación de lo que somos. Esto involucra tanto a los que estamos en vida: mi abuela Pilín, mi abuela Elisa, mi madre, mi padre, mis tías Pepa y Amalia, mis tíos José Amalio y Antonio, mis otros tíos y tías (si os nombro no termino nunca), mi hermana Pilarina y mi hermano Joselito, mis primos y primas (esto da para una tesis entera) y mi novia Leire; como los que se han ido: mis antepasados que no he llegado a conocer, pero son eternos en nuestras vidas, familiares que sí he conocido y serán eternos, mi querido abuelo Pepe, mis queridas tías abuelas Matildita y Amalita, y mis queridas tías Matilde, Pepa y Salud. Gracias por todo.

¡Cómo olvidarme de mis amigos! Los que me aportan energía y momentos positivos. No os voy a citar uno a uno, y los detalles mejor dejarlos para unas cervezas. Gracias. También quiero agradecer a mis compañeros del doctorado: Carolina, Emanuel, Rocío, Valle, Marc, Gloria y Antonio; y a los profesores del departamento: Filippo, Aurora, Manuel y Eduardo; por los buenos momentos, el gran compañerismo, las risas y las conversaciones que hemos tenido durante estos años. Siendo tan importantes como el propio trabajo, gracias. Tampoco me puedo olvidar de mi equipo de fútbol Potathinaikos. Momentos importantes de desconexión que hay que cuidar. ¡Gracias shavales!

Los últimos son los primeros. Este último párrafo es para una persona muy especial en mi vida, Leiritz. Gracias por todo tu apoyo, PACIENCIA, cariño y comprensión. Aunque ya te he nombrado antes, quiero destacar lo importante y esencial que has sido en estos años. Como he dicho al inicio, no puedo transmitirte mis sentimientos y agradecimientos en palabras, ¡así que vamos a celebrarlo!

Published and submitted content

- Items included in this report

1. Ana Carpio and Rafael González-Albaladejo, *Immersed Boundary Approach to Biofilm Spread on Surfaces*. Communications in Computational Physics **31**, 257-292 (2022). Fully included in Chapter 4.
2. Rafael González-Albaladejo, Ana Carpio, and Luis L. Bonilla, *Scale free chaos in the confined Vicsek flocking model*. Phys. Rev. E **107**, 014209 (2023). Fully included in Chapters 2 and 3.

- Items not included in this report

1. Ana Carpio and Rafael González Albaladejo, Chapter *Immersed Boundary Models of Biofilm Spread* of the Book *Progress in Industrial Mathematics at ECMI 2021*. Springer, 53-59
2. Rafael González-Albaladejo, Falko Ziebert and Ana Carpio, *Two-fluid variable length model for cell crawling*. *Work in progress*
3. Rafael González-Albaladejo and Luis L. Bonilla, *Mean field theory of chaotic insect swarms*. *Work in progress*

I have been involved in all roles. In particular I have participated in the realization of the model, in the theoretical studies, I have done all the numerical codes, I have analyzed the data and discussed the results. Copyright statement includes the use of all or parts of the article for the authors' or their employers educational or research purposes, which is the case of this thesis.

Abstract

The behavior of living systems can exhibit emergent phenomena that are not present in their individual components. Living systems are far from equilibrium, may lack conservation laws and using tools from statistical physics and thermodynamics is challenging. However, quantitative observations and experiments yield a wealth of data that allow to design models capturing important aspects of the behavior of these systems. This thesis focuses on two topics, the collective behavior of midge swarms and the collective behavior of bacterial biofilms. Prior studies of insect swarms have focused on their formation as an ordering phase transition, which fails to capture many qualitative and quantitative features. In this thesis we study the Vicsek model confined by a harmonic potential. By using dynamical systems and statistical mechanics tools, we have discovered a novel phase transition characterized by *scale free chaos*, which exhibits power laws and present qualitative features compatible with observations of swarms of male midges in nature and in the laboratory. On the second topic, bacterial biofilms pose a challenge to theorists, who must model elements on different spatial and temporal scales. We present a hybrid model based on an architecture of immersed boundaries with a dynamic energy budget metabolism. The model captures geometric differences between bacteria, being able to reproduce varied patterns depending on their shapes and competence phenomena between different types. We can study antibiotic resistance in biofilms and test cocktails to eradicate them.

El comportamiento de los sistemas vivos puede mostrar fenómenos emergentes que no están presentes en sus componentes individuales. Los sistemas vivos están alejados del equilibrio, pueden carecer de leyes de conservación y es todo un reto emplear herramientas de la física estadística y la termodinámica. Experimentos y observaciones cuantitativas producen una gran cantidad de datos que permiten diseñar modelos que expliquen aspectos importantes del comportamiento de estos sistemas. Esta tesis se centra en dos temas, el comportamiento colectivo de los enjambres de insectos voladores como los mosquitos y el

comportamiento colectivo de las biopelículas bacterianas. Los estudios previos de enjambres de insectos se han centrado en su formación como una transición orden-desorden, lo que no explica muchos aspectos tanto cualitativos como cuantitativos. En esta tesis estudiamos el modelo de Vicsek confinado por un potencial armónico. Usando herramientas de sistemas dinámicos y de mecánica estadística hemos descubierto una nueva transición de fase caracterizada por *caos libre de escalas*, que presenta leyes de potencias y tiene rasgos cualitativos compatibles con las observaciones y experimentos de laboratorio de enjambres de dípteros. Por otro lado, las biopelículas bacterianas plantean un reto teórico, pues se debe modelar elementos a diferentes escalas espaciales y temporales. Presentamos un modelo híbrido basado en una arquitectura de fronteras inmersas con un metabolismo de presupuesto de balance energético. El modelo captura las diferencias geométricas entre bacterias, generando patrones diversos según su forma y competencia entre bacterias de distintos tipos. Permite estudiar la resistencia de biopelículas a antibióticos y el diseño de cócteles para erradicarlos.

Contents

Acknowledgements	i
Published and submitted content	iii
Abstract	v
1 Introduction	3
1.1 Swarms of midges and the Vicsek model	3
1.2 Bacterial biofilms	7
1.3 Outline	10
2 Transition from single-cluster to multi-cluster chaos in the confined Vicsek Model	11
2.1 Introduction	11
2.2 Confined Vicsek model	12
2.3 Deterministic and noisy chaos	14
2.4 Phase transition and topological data analysis.	15
2.5 Summary	20
Appendix 2.A Nondimensionalized equations of the confined Vicsek model .	20
Appendix 2.B Chaotic and noisy dynamics	21
2.B.1 Benettin algorithm.	22
2.B.2 Scale dependent Lyapunov exponents	22
2.B.3 Largest Lyapunov exponent from high dimensional reconstructions of CM motion	25

3	Scale free chaos phase transition	27
3.1	Introduction	27
3.2	Phase transitions within regions of chaos	28
3.2.1	Critical confinement from correlation time	29
3.2.2	Critical confinement from the static correlation.	36
3.3	Subtracting rotation and dilation from CM velocity and flocking black hole phase transition	37
3.3.1	Critical exponents from confined VM simulations	39
3.3.2	Flatness function.	40
3.4	Discussion	41
3.5	Summary	47
	Appendix 3.A Dynamic and static connected correlation functions	49
	Appendix 3.B Susceptibility and correlation time	56
4	Immersed boundary approach to biofilm spread on surfaces	59
4.1	Introduction	59
4.2	Model	60
4.2.1	Immersed boundary representation.	60
4.2.2	Forces	61
4.2.3	Cellular activity	63
4.3	Nondimensionalization of the equations.	65
4.4	Computational model for unconstrained spread.	69
4.4.1	Discretization.	70
4.4.2	Rules for division and death	72
4.4.3	Initialization and boundary conditions	74
4.4.4	Dynamics of incipient biofilms	76
4.5	Computational model in the presence of barriers	80
4.6	Biofilm extinction	85
4.7	Summary	88
5	Overall conclusions	89
	Bibliography	95

Introduction

In the present work, we explore collective biological behavior from a biophysics and mathematics perspective. We show how mathematical models, computational tools, continuum mechanics and statistical physics can be used to better understand the principles behind the dynamics of some biological systems. Our study focuses on the collective behavior of different biological aggregates, namely insect swarms and bacterial biofilms.

Insect swarms can be considered examples of active matter because these systems comprise self-driven units (active particles), each capable of converting stored or ambient free energy into systematic movement (Marchetti et al. 2013). Studies of active matter often use tools from statistical physics, dynamical systems, continuum mechanics and assorted mathematics.

Motile bacteria can also form swarms. However, we analyze here the biofilm habitat. In them, cells are embedded in a self-produced polymeric matrix and cannot move by themselves. However, their biological activity responds to environmental conditions and mechanical processes, which, in turn, respond to collective cell behavior. They are usually considered as living soft matter and modeled as live deformable materials (Costerton et al. 1995; Parsek et al. 2005; H. C. Flemming et al. 2016).

1.1 Swarms of midges and the Vicsek model

The collective behavior of animal groupings, such as insect swarms, fish schools, bird flocks, and human crowds (Okubo 1986; Parrish et al. 1999; Sumpter 2010; Vicsek and Zafeiris 2012; Ouellette 2022) has always fascinated people. These groupings share com-

mon characteristics that suggest there may be fundamental principles at play beyond just their biological details. Opinions about what these principles might be have often reflected fashions of the times. At the end of the XIX century and beginning of the XXth, alleged causes of collective behavior of animal groupings have been collective hypnosis, (Le Bon 1895; Le Bon 1897), telepathy, (Long 1919), or the formation of a collective individual, (Huxley 1912), or superorganism, (Wilson et al. 1989). In the same period, researchers closer to observations argued that the spread of impulse within well-organized groups was enough to explain the apparent existence of a collective consciousness, (Miller 1921). Recently, technological advancements in stereo videography and calibration have provided a wealth of quantitative data for studying collective biological motion (Theriault et al. 2014). Better data and the more recent methodologies associated to phase transitions in statistical mechanics, chaos theory, continuum mechanics and active matter allow for more quantitative analyses that may lead to better understanding of flocking phenomena. The example of mating swarms of male midges that we consider in this thesis leads to a particular model of active particles that exhibits novel phase transitions between different forms of chaotic attractors, as we shall explain below.

Active matter encompasses all scales of living beings, from bacteria and biopolymers to groups of people, as illustrated by Figure 1.1. We distinguish ordered patterns and disordered but strongly correlated behavior in this figure: some bacteria, flocks of birds, fish schools and groups of people form ordered patterns, whereas no order is apparent in other bacteria, swarms of midges and snails. Several disordered groupings have nevertheless strong correlations between active particles, as shown by observations of midge swarms in nature (Attanasi, Cavagna, L. Del Castello, et al. 2014; Attanasi, Cavagna, L. D. Castello, et al. 2014).

To understand the formation of animal flocks, a paradigmatic model is due to Vicsek *et al.*, (Vicsek, Czirók, et al. 1995). The Vicsek model (VM) consists of N self-propelled particles moving with constant speed in a box with periodic boundary conditions. The particle dynamics is discrete in time, and the direction of the velocity of each particle is given by the average velocity of particles in its neighborhood plus an alignment noise (Vicsek and Zafeiris 2012; Vicsek, Czirók, et al. 1995). The VM describes *dry active matter* in which active particles are not immersed in a moving medium or fluid (Chaté 2013; Marchetti et al. 2013). For large enough boxes, the VM undergoes an ordering transition for noise below a critical value (or particle density above a critical value) in which a gas of disordered particles filling the box evolves to ordered patterns such as traveling bands, which then form an ordered “liquid” for noise below another threshold (Chaté 2013). For smaller boxes, the phase of ordered bands does not appear, and the transition is from gas to liquid (Chaté 2013). The order parameter of the flocking transition is the polarization, i.e., the average velocity of all particles divided by their common speed.

Insect swarms provide particularly rich empirical data and peculiar critical behavior (Attanasi, Cavagna, L. Del Castello, et al. 2014; Attanasi, Cavagna, L. D. Castello, et al. 2014; Okubo 1986; Okubo and Levin 2001; Kelley et al. 2013; Puckett et al. 2014;

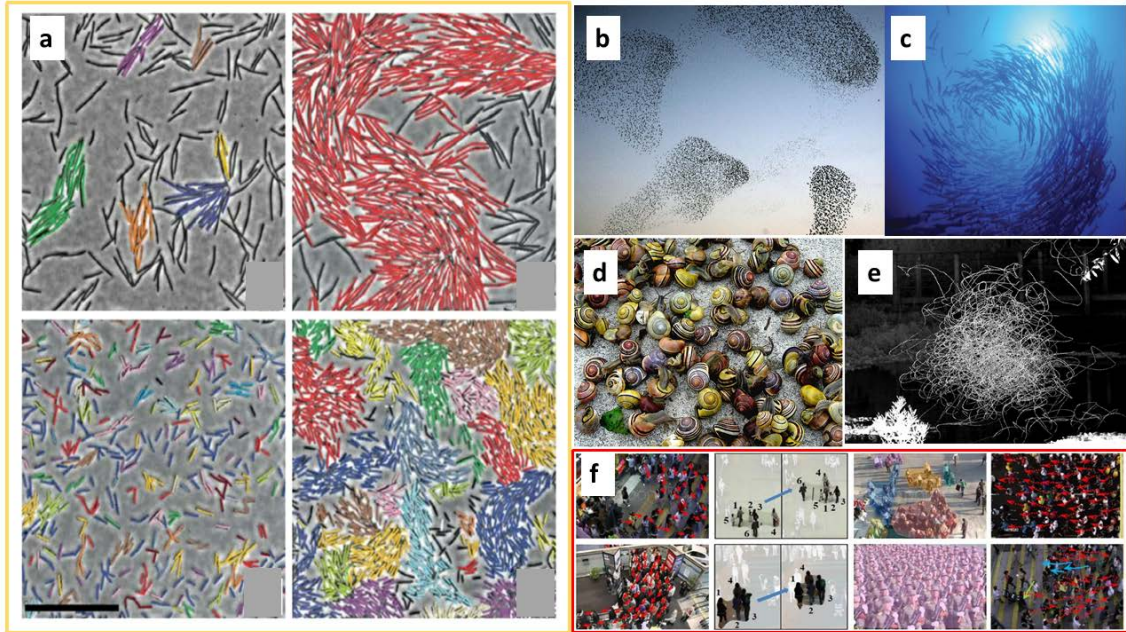


Figure 1.1: (a) Active bacteria groupings from (Be’er et al. 2015). (b) Flocks of birds taken from the website <https://www.science.org/content/article/how-bird-flocks-are-liquid-helium> (“How bird flocks are like liquid helium” 2014). (c) Fish schools taken from (Lopez et al. 2012). (d) Snail swarms taken from (Silvertown et al. 2011). (e) Trajectories of midges in the wild taken from (Cavagna, Conti, et al. 2017), in <https://physics.aps.org/articles/v7/120>, (“Insect Swarms Go Critical” 2014). (f) Groups of people, taken from the website <https://crowdbehaviordotorg.wordpress.com/>, (“Scene-Independent Group Profiling in Crowd” 2014).

Cavagna, Conti, et al. 2017; Gorbonos et al. 2016; Sinhuber et al. 2017). Male midges and other diptera form swarms near visual markers to attract females for reproductive purposes (Okubo 1986; Okubo and Levin 2001; Puckett et al. 2014). While small swarms track the marker shape, larger swarms are more isotropic and shape independent (Puckett et al. 2014). In laboratory experiments, swarms form far from the walls of the enclosure that contains them (Kelley et al. 2013). Topological data analysis of experiments shows that the swarm can be thought of as a condensed phase (the swarm nucleus) surrounded by a vapor phase (insects leaving and entering the nucleus (Sinhuber et al. 2017)).

Natural swarms present collective behavior and strong correlations but not global order. The polarization order parameter is quite small but the correlation length (measuring the largest distance between two insects whose velocity fluctuations still influence each other) is proportional to the swarm size (Cavagna, Conti, et al. 2017). It is also much larger than all other length scales, such as insect size, average separation between insects, etc. Macroscopic variables, such as the correlation length, the susceptibility to polarization changes and the dynamic correlation, follow power laws as functions of the

distance to criticality, with critical exponents that differ from those of equilibrium and many nonequilibrium phase transitions (Huang 1987; Attanasi, Cavagna, L. Del Castello, et al. 2014; Attanasi, Cavagna, L. D. Castello, et al. 2014; Cavagna, Conti, et al. 2017). Cavagna and coworkers have shown that the characteristic timescale, static and dynamic connected correlation functions depend on the control parameters (density, noise, ...) only through the correlation length. This is the finite-size scaling hypothesis, which is similar to that found in second-order equilibrium phase transitions (Huang 1987). Finite-size scaling allows us to extrapolate power laws of macroscopic variables obtained for finite N to the case of infinitely many particles, which characterize phase transitions (Amit et al. 2005). Attempts to use the ordering transition of the three-dimensional (3D) VM to explain observed critical exponents produced exponent values quite different from experimental ones (Attanasi, Cavagna, L. D. Castello, et al. 2014; Cavagna, Conti, et al. 2017).

A line of theoretical research intends to attain critical exponents close to those measured in natural swarms of midges by performing renormalization group calculations in modified versions of the Toner-Tu hydrodynamic equations (Toner and Tu 1995; Toner, Tu, et al. 2005; Chen, Toner, et al. 2015; Chen, Lee, et al. 2018; Cavagna, Carlo, Giardina, Grigera, and Pisegna 2021; Cavagna, Carlo, Giardina, Grigera, Melillo, et al. 2021). The idea is that critical exponents obtained from the fixed points of an appropriate renormalization group belong to the same universality class, no matter their peculiar features. However, the symmetric phase of the modified Toner-Tu equations is far from observed insect swarms.

In this thesis, we introduce more realistic features in the VM and study its underlying phase transitions. In particular, (Gorbonos et al. 2016) proposed a self-gravitating model of swarms that accounts for many observations in the laboratory (Ouellette 2022), such as their effective Young modulus (Ni and Ouellette 2016). Inside a self-gravitating sphere, particles are subject to a harmonic potential and we propose replacing the confining periodic box of the VM by a linear spring force. A harmonic potential for swarms was proposed earlier by (Okubo 1986; Kelley et al. 2013) and, in relation with the VM, by (Attanasi, Cavagna, L. D. Castello, et al. 2014; Cavagna, Conti, et al. 2017). Unlike these later authors, we do not focus in the usual VM ordering transition. Instead, we have found hitherto unsuspected new states in the harmonically confined VM: periodic, quasiperiodic and chaotic attractors modified by the VM alignment noise. Depending on the scale-dependent Lyapunov exponents, we can distinguish deterministic chaos, noisy chaos and predominantly noisy states (Gao, Hu, et al. 2006). Within the parameter region of noisy chaos, we have found a new phase transition with scale free chaos that presents many of the observed features of natural swarms and critical exponents compatible with observations (González-Albaladejo et al. 2023). For finitely many particles, the confined VM has a transition between single and multicluster swarms at which the correlation length is proportional to the swarm size. We study this transition using numerical simulations, the finite size scaling hypothesis and the tools of the statistical mechanics of phase

transitions. Correlation length and susceptibility obey power laws with critical exponents compatible with those observed in nature and correlation time and correlation length scale with a dynamical exponent that is close to one. We find that the confining strength at the critical line goes to zero as the number of particles goes to infinity. The largest Lyapunov exponent is positive but it also goes to zero as a power law with a novel critical exponent. Thus, we have discovered and analyzed the novel nonequilibrium phase transition of scale free chaos (González-Albaladejo et al. 2023). The specifics of our study are explained in Chapters 2 and 3. We have also found another phase transition with the same critical exponents as in gravitational collapse, and we have called the resulting phase a *flocking black hole*.

1.2 Bacterial biofilms

The other part of the thesis deals with soft matter or soft condensed matter, which is a subfield of condensed matter related to systems with deformable elements. These systems live on the energy scale of the ambient temperature, (Kleman et al. 2003), and are composed of liquids, colloids, granular materials, polymers, liquid crystals, etc., within them. The attempt to understand this matter came from Albert Einstein's work on Brownian motion, being the beginning of the work on colloids, (Einstein 1905). Later Pierre-Gilles de Gennes, who is considered to be the main creator of this matter, gathered all the works to find the universality of these materials by considering the phase transitions from disorder to order of simple systems in these complex systems, (De Gennes 1974). One of the most curious examples or anecdotes of this type of matter is explained by Pierre-Gilles de Gennes himself in (De Gennes 1991) where he tells that the indigenous people living in the Amazon already discovered the potential of this material. They coated their feet with tree sap and left it to dry. At first the polymeric chains are independent and flexible, but when left in the air for a while, oxygen enters the material, creating bridges between the chains. In this way we go from a liquid structure to a network structure that resists tension, being what we now call rubber.

One of the systems within the large number of soft matter biomaterials are bacterial biofilms, (Costerton et al. 1995; Parsek et al. 2005; H. C. Flemming et al. 2016), which are important for human health such as the development of various infectious diseases and their resistance to antibiotics, (Ciofu et al. 2022). The term biofilm was introduced in 1995 by Bill Costerton, recognised as the founder of the field, (Lappin-Scott et al. 2014). In this first work we will focus on biofilms on a surface, i.e. the biofilm is deformable and changes in the number of bacteria, which organise themselves keeping the whole group practically static, see Fig. 1.2. If self-propelled bacteria were to be studied, they would be treated as soft active matter, which we do not address in the present work. The great difficulty of these systems is to model and capture their characteristics, so we will focus on making a computational model that simulates this complex system in Chapter 4.

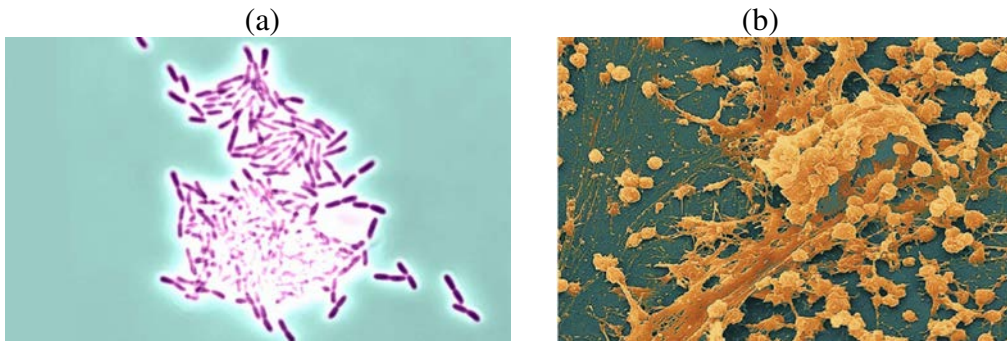


Figure 1.2: Experimental views of incipient biofilms on surfaces. Bacteria plus polymeric slime for (a) rod-like bacteria (Courtesy of Professor Vernita Gordon, University of Texas at Austin (Kirsch 2017)) and (b) spherical bacteria (reprinted from (Scherberger 2018)).

Biofilms are formed by bacteria glued together by a self-produced polymeric matrix and attached to a moist surface (H. Flemming et al. 2010). The polymeric envelop makes biofilms extremely resistant to antibiotics, disinfectants and chemical or mechanical aggressions (Høiby et al. 2010). Experiments reveal that their structure varies according to environmental conditions. When they grow in flows (Drescher et al. 2013; Laspidou et al. 2014; Lardon et al. 2011; Sudarsan et al. 2016), we see scattered bacteria immersed in large chunks of polymer. When they form on interfaces with air or tissue, volume fractions of polymer are very small (Seminara et al. 2012; Storck et al. 2014; Grant et al. 2014) and biofilms resemble aggregates of spherical or rod-like particles, see Figure 1.2 for a view of very early stages. As they mature, three dimensional sheets are formed, see Figure 1.3.



Figure 1.3: Scheme of a vertical slice of a biofilm seed spreading on a surface, see (Seminara et al. 2012; Asally et al. 2012; Wilking et al. 2013).

Modeling bacterial growth in the biofilm habitat is a complex task due to the need to couple cellular, mechanical and chemical processes acting on different times scales. Many approaches have been proposed, ranging from purely continuous models (Seminara et al. 2012) to agent based descriptions (Laspidou et al. 2014; Rodriguez et al. 2012; Lardon et al. 2011; Sudarsan et al. 2016; Storck et al. 2014; Grant et al. 2014) and hybrid models combining both (Carpio, Cebrián, and Vidal 2019; Carpio and Cebrián 2020). Complexity increases when we aim to take bacterial geometry into account, issue that we intend to address here borrowing ideas from immersed boundary (IB) methods (Peskin 2002). These methods have already been adapted to simulate different aspects of biofilms

in flows, such as finger deformation (Sudarsan et al. 2016), attachment of floating bacteria (Dillon, Fauci, et al. 1996), and viscoelastic behavior (Stotsky et al. 2016). Cell growth and division were addressed by removing the incompressibility constraint on the surrounding flow and including ‘ad hoc’ inner sources (Li et al. 2012). Recent extensions to multicellular growth consider closely packed deformable cells attached to each other (Rejniak 2007; Dillon, Owen, et al. 2008). Biofilms growing on interfaces differ from multicellular tissues in several respects. First, bacterial shapes are more rigid, usually spheres or rods. Second, bacteria remain at a short, but variable, distance of each other. To describe their evolution we need to take into account at least:

- Bacterial activities, such as growth, division and death in response to the environmental conditions.
- Chemical processes, such as diffusion of oxygen, nutrients, and toxicants (waste products, antibiotics) and production of autoinducers.
- Mechanical processes, such as the interaction of the fluid with the immersed structures and the interaction between the structures themselves.

These processes evolve in different time scales. Compared to cellular processes, which develop in a time scale of hours, mechanical and chemical processes are quasi-stationary. The inherent time scale for them would be seconds. Fast flow processes like adhesion or motion carried by a flow are not relevant for biofilms spreading on a surface. Instead, water absorption from the substrate in the time scale of growth is a factor to consider. Variations in the biofilm are driven by cellular activities, in a time scale of hours, through changes in the immersed boundaries due to cell growth, division, and death (Seminara et al. 2012; Chai et al. 2011; Carpio, Cebrián, and Vidal 2019). These processes are influenced by the secretion of autoinducers and the production of waste products and polymers (Seminara et al. 2012; Chai et al. 2011; Carpio, Cebrián, and Vidal 2019).

Understanding the mechanisms of biofilm growth and spread is important for developing strategies to prevent or control the spread of infections caused by biofilms. In this thesis, we present a mathematical model based on the immersed boundary method for simulating the spread of biofilms on surfaces, with a numerical approach for solving fluid dynamics problems that involves representing the boundaries of complex geometries as a series of points immersed in the fluid. We use this method to simulate the growth and spread of biofilms on surfaces and investigate the effects of different parameters such as the fluid flow rate and the initial distribution of the biofilm. We also add an dynamic energy budget model to each bacterium that governs internal biological behaviours such as cell division and cell death, and a system of equations that simulate different chemical or complex substances concentrations that exist in the environment such as nutrients, polymers and toxins. The results of the simulations provide insight into the mechanisms of biofilm spread and could be used to develop new strategies for controlling the spread of biofilms on surfaces.

1.3 Outline

The thesis is organized as follows. Chapters 2 and 3, are devoted to study the confined Vicsek model as applied to midge swarms, whereas bacterial biofilms are analyzed in Chapter 4. Thus, in Chapter 2 we discuss the Vicsek model confined by a harmonic potential and a novel chaotic transition for a finite number of particles, which is scale free. Different qualitative features of single and multicluster chaotic states separated by this transition are studied by Topological Data Analysis. In Chapter 3, we use the finite size scaling hypothesis to study the scale-free-chaos phase transition and find different critical exponents for order parameter, correlation length, susceptibility and largest Lyapunov exponent. We find that, for finitely many particles, there is an extended criticality region beyond the line separating single and multicluster chaos. This region collapses to zero confinement strength as the number of particles goes to infinity. A different phase transition for large confinement strength consists of finite regions containing an increasing number of particles, the flocking holes. The material presented in Chapters 2 and 3 is contained in our publication (González-Albaladejo et al. 2023). Chapter 4 is based on our publication (Carpio and González-Albaladejo 2022). In it, we model bacterial biofilms representing bacteria by boundaries immersed in a viscous fluid and the polymeric matrix by a friction term. The interactions of the bacteria among themselves are modeled by additional forces on the immersed boundaries. Bacterial metabolism and response to antibiotics is described by a dynamic energy budget approach. The computational model is solved numerically by parallelizing the codes when possible and used to investigate antibiotic resistance. In Chapter 5 we discuss the overall results in comparison with other theoretical models and experiments, and comment on some conclusions. Finally, at the end we collect all the references of the thesis in alphabetical order.

Transition from single-cluster to multi-cluster chaos in the confined Vicsek Model

2.1 Introduction

In this chapter, we study the 3D VM confined by a harmonic potential (Attanasi, Cavagna, L. Del Castello, et al. 2014; Attanasi, Cavagna, L. D. Castello, et al. 2014; Cavagna, Conti, et al. 2017). Confining harmonic potentials have long been proposed as models for swarm behavior (Okubo 1986; Okubo and Levin 2001; Gorbonos et al. 2016; Ni and Ouellette 2016). We have made a number of discoveries. As the confinement parameter β decreases, the VM changes from a period 2 attractor at large confinement values to other periodic, quasiperiodic and chaotic attractors. Using β as control parameter, there are windows of chaotic solutions followed by intervals of non-chaotic behavior. For β and η small but nonzero, a line in the noise- β plane separates chaotic single cluster from multicluster swarms. Similar to observations (Sinhuber et al. 2017), the single cluster swarm consists of a ‘condensed’ nucleus and particles leaving and entering it.

The rest of the chapter is as follows. We present the confined Vicsek model in Section 2.2 and find different attractors as the confinement parameter decreases from a large value. Among them, period 2, period 4, periodic solutions, quasiperiodic solutions, large period solutions, and chaotic attractors with positive Lyapunov exponents. Section 2.3 discusses algorithms to calculate the largest Lyapunov exponent (LLE) and how to distinguish deterministic and noisy chaos from noise, using Gao *et al*’s scale dependent Lyapunov exponents (Gao, Hu, et al. 2006). Section 2.4 uses topological data analysis to characterize the phase transitions from single cluster to multicluster chaotic attractors. Section 2.5

contains our conclusions whereas the Appendices are devoted to technical matters. Appendix 2.A describes our nondimensionalization of the confined Vicsek model. Appendix 2.B describes the Benettin algorithm (Benettin et al. 1980; Ott 1993; Cencini et al. 2010), scale dependent Lyapunov exponents (Gao, Hu, et al. 2006) and the Gao-Zheng algorithm to extract the largest Lyapunov exponent from high dimensional reconstructions of the chaotic attractor using lagged coordinates (Gao and Zheng 1994).

2.2 Confined Vicsek model

We have nondimensionalized the VM governing equations using data from natural swarms (see Appendix 2.A):

$$\begin{aligned} \mathbf{x}_i(t+1) &= \mathbf{x}_i(t) + \mathbf{v}_i(t+1), \\ \mathbf{v}_i(t+1) &= v_0 \mathcal{R}_\eta \left[\Theta \left(\sum_{|\mathbf{x}_j - \mathbf{x}_i| < R_0} \mathbf{v}_j(t) - \beta \mathbf{x}_i(t) \right) \right], \end{aligned} \quad (2.1)$$

where $i = 1, \dots, N$, $v_0 = 1$ is a constant speed, $R_0 = 1$, β is the confinement strength. The position and velocity of the i th particle at time t are $\mathbf{x}_i(t)$ and $\mathbf{v}_i(t)$, respectively. In (2.1), $\Theta(\mathbf{x}) = \mathbf{x}/|\mathbf{x}|$ and $\mathcal{R}_\eta(\mathbf{w})$ rotates the unit vector \mathbf{w} randomly within a spherical cone centered at its origin and spanning a solid angle in $(-\frac{\eta}{2}, \frac{\eta}{2})$. The 2D VM is defined similarly. Initially, the particles are randomly placed within a sphere with unit radius and the particle velocities point outwards.

The VM exhibits a variety of attractors for different values of confinement β and alignment noise η , as depicted in Fig. 2.1 for $\eta = 0$ and $N = 128$. For large β , the swarm occupies the unit sphere and it is pulsating with period 2: all particles reverse their velocities at each time step. The center of mass (CM) of the swarm occupies two positions ($\beta = 60000$) or four ($\beta = 300$, period 4 attractor) as shown in Fig. 2.1(a). As β decreases, there appear quasiperiodic attractors interspersed with periodic attractors with higher periods, and chaotic attractors, cf. Fig. 2.1(b)-(f).

Fig. 2.2(a)-(b) show how different attractors in Fig. 2.1 appear as the parameter β changes. Periodic and quasiperiodic attractors exist for large confinement values and quasiperiodicity turns into chaos below $\beta \approx 30$. The chaotic attractor first looks like a torus and its central hole is filled as β decreases, cf. Figs. 2.1(d)-(f). As shown in cf. Fig. 2.2(c), the alignment noise increases LLE values, there are parameter regions where noise induces chaos and there are the transition from chaos single-cluster to chaos multi-cluster which will be discussed later.

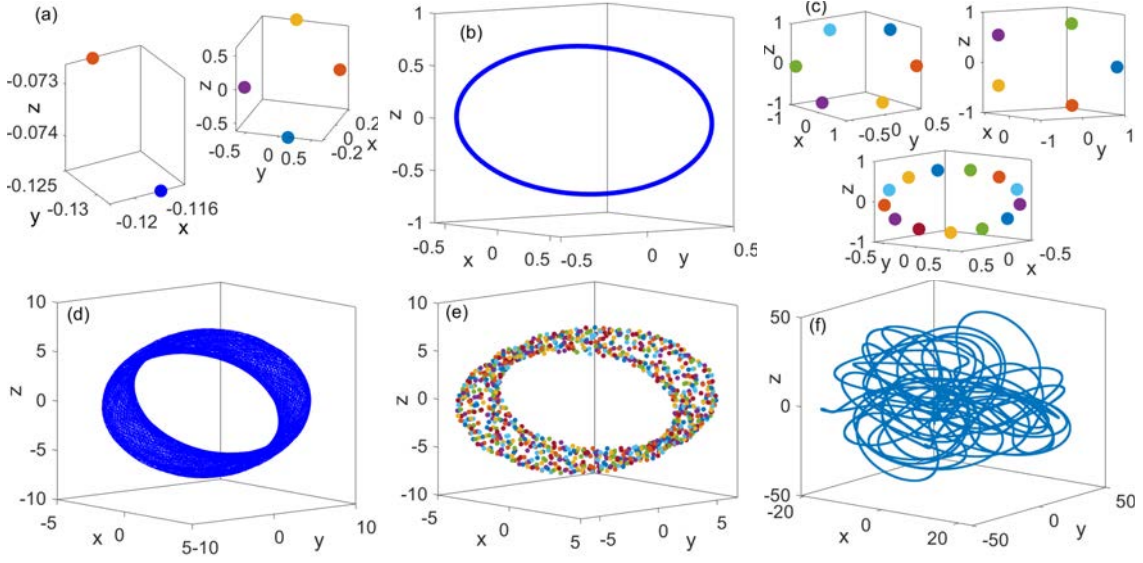


Figure 2.1: Center of mass trajectories of different attractors for $N = 128$, $R_0 = v_0 = 1$, $\eta = 0$ and different β . **(a)** Period 2 ($\beta = 60000$) and period 4 ($\beta = 300$) attractors. **(b)** Quasiperiodic attractor that appears at $\beta = 2N = 256$. **(c)** Periodic solutions with larger periods: 6 ($\beta = N = 128$), 5 ($\beta \approx 177$), and 13 ($\beta \approx 225$). **(d)-(e)** Torus-like chaotic attractor for $\beta = 1$ depicted for a long and a shorter time interval. **(f)** Chaotic attractor for $\beta = 0.01$: the center-of-mass trajectory will fill a sphere-like body if depicted for much longer times. Note that increasing β confines the motion to smaller volumes.

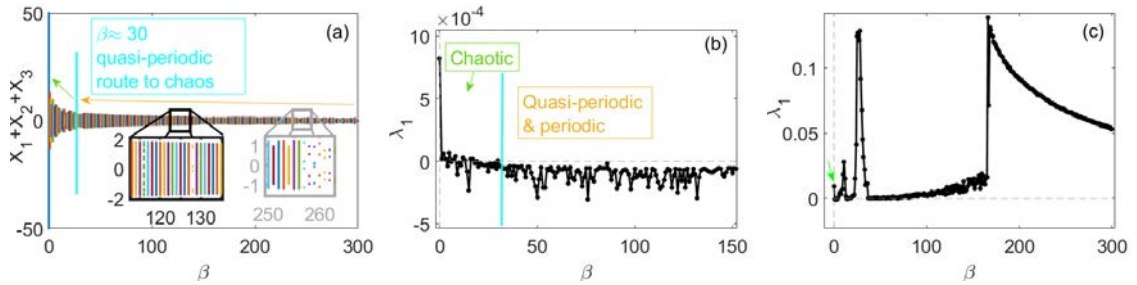


Figure 2.2: **(a)** Bifurcation diagram of the sum of CM coordinates in nondimensional units and **(b)** largest Lyapunov exponent (LLE) versus β for $\eta = 0$. The boxes in Panel (a) about $\beta = N$ and $\beta = 2N$ correspond to period 6 solutions and others interspersed with quasiperiodic solutions, and a period 4 to quasiperiodic transition, respectively. Chaotic solutions appear following the quasiperiodic route to chaos. In panel (a), note the large increase of the range of CM values as β decreases. **(c)** Same as Panel (b) for $\eta = 0.5$. Note how noise increases the value of the LLE and induces chaos for confinement values that correspond to quasiperiodic attractors for $\eta = 0$. The area marked by green arrow in Panel (c) corresponds to the change of chaos single-cluster to chaos multi-cluster. Other parameters are as in Fig. 2.1.

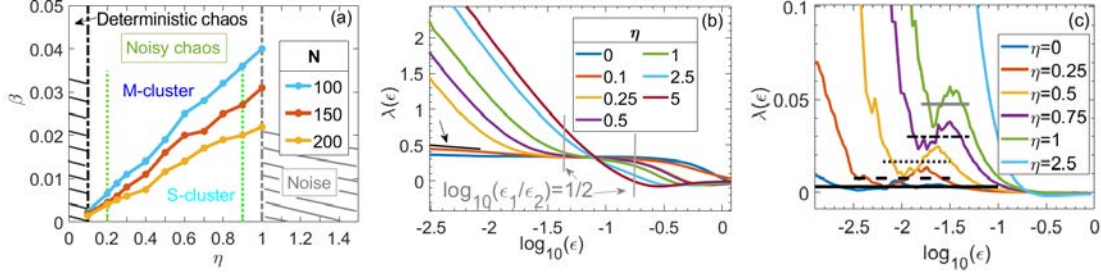


Figure 2.3: **Transition from chaos single-cluster to chaos multi-cluster.** (a) Phase diagram β vs η exhibiting regions of deterministic and noisy chaos, and of noisy disorder. The vertical lines at $\eta = 0.2$ and 0.9 correspond to the maximum correlation length observed in experiments and to the noise for which the dynamic correlation function ceases to be flat near $t = 0$, respectively. Noise swamps chaos for $\eta \geq 1$. The three lines of critical points in the noisy chaos region correspond to critical confinement $\beta_c(N, \eta)$ for $N = 100, 150, 200$. They separate multicluster (M-cluster) from single cluster (S-cluster) chaos. This Panel is closely related to Chapter 3 defining the transition as **scale-free chaos**. (b) Largest scale-dependent Lyapunov exponent as a function of the scale parameter ϵ for $N = 100$, different values of η , two lagged coordinates $m = 2$ and $\beta = \beta_c(N, \eta)$, see Appendix 2.B. The LLE is the value of $\lambda(\epsilon)$ at a plateau (ϵ_1, ϵ_2) whose width satisfies $\log_{10}(\epsilon_2/\epsilon_1) \geq 1/2$ (Appendix 2.B). The vertical lines mark the width of the critical plateau at which: $\log_{10}(\epsilon_2/\epsilon_1) = 1/2$ and correspond to the grey vertical dot-dashed line in Panel (a). The black line and arrow mark the very small slope of the SDLE for noise values close to deterministic chaos. By convention (Gao, Hu, et al. 2006), noise swamps chaos when $\log_{10}(\epsilon_2/\epsilon_1) < 1/2$. (c) Largest scale-dependent Lyapunov exponent as a function of the scale parameter ϵ for $N = 100$, different values of η , and $\beta = \beta_c(N, \eta)$ with $m = 6$, instead of $m = 2$ as in Panel (b). The averages of the oscillations corresponding to the plateau region in Panel (b) increase with the noise η indicating that so does the LLE: $\lambda_1(0) \sim 0.003$, $\lambda_1(0.25) \sim 0.0075$, $\lambda_1(0.5) \sim 0.0165$, $\lambda_1(0.75) \sim 0.03$, $\lambda_1(1) \sim 0.0476$.

2.3 Deterministic and noisy chaos

For small confinement values and appropriate noise, the VM exhibits chaotic attractors characterized by positive values of the largest Lyapunov exponent (LLE). It is important to assess the role of noise. As explained in Appendix 2.B, three methods to calculate the LLE produce the same values and yield complementary information: (i) applying the Benettin algorithm to Eq. (2.1) (Benettin et al. 1980; Ott 1993; Cencini et al. 2010); (ii) using the Gao-Zheng test (Gao and Zheng 1994) on time traces of the swarm center-of-mass (CM) motion $\mathbf{X}(t)$ (which could be acquired from measurements of natural swarms); (iii) scale-dependent Lyapunov exponents from time traces, which discriminate between chaos and noise (Gao, Hu, et al. 2006).

Fig. 2.3(a) is the phase diagram (η, β) displaying phases of deterministic, noisy chaos and noise. Inside the noisy chaos phase we have indicated the critical lines of the transition

from chaos s-cluster to chaos m-cluster for different N . Chaos is scale free on those lines because the correlation length defined in the next chapter is proportional to the swarm size for all values of N . To distinguish chaotic and noise phases, we have plotted in Fig. 2.3(b) the scale-dependent Lyapunov exponent (SDLE) $\lambda(\epsilon)$. For $\epsilon_t = \epsilon$, the SDLE satisfies $\ln \lambda(\epsilon_t) = (\ln \epsilon_{t+\Delta t} - \ln \epsilon_t) / \Delta t$, where ϵ_t and $\epsilon_{t+\Delta t}$ are the average separation between nearby trajectories at times t and $t + \Delta t$. Appendix 2.B explains how to calculate $\lambda(\epsilon)$ from time traces of center-of-mass motion with m -dimensional lagged vectors (Gao, Hu, et al. 2006). If $m = 2$, Fig. 2.3(b) shows that for $\eta = 0$, $\lambda(\epsilon)$ is flat at small scale and decreases for $\epsilon \approx 1$. For nonzero noise, $\lambda(\epsilon)$ decreases, reaches a plateau and decreases again as the scale ϵ increases. As noise increases, the curves $\lambda(\epsilon)$ permit distinguishing regions in the phase plane (η, β) of Fig. 2.3(a) where chaos is either mostly deterministic, substantially altered or even induced by noise (noisy chaos), and swamped by noise; see Appendix 2.B and (Gao, Hu, et al. 2006). The noise level used in the numerical simulations of Refs. (Attanasi, Cavagna, L. Del Castello, et al. 2014; Attanasi, Cavagna, L. D. Castello, et al. 2014; Cavagna, Conti, et al. 2017) is 5.65 in our units. Thus, it is fully inside the noise region of Fig. 2.3(a), far from the noisy chaos parameter values we consider here.

When two lagged coordinates are sufficient to reconstruct the chaotic attractor from CM data, the value of the SDLE $\lambda(\epsilon)$ at the plateau coincides with the LLE calculated directly from the equations of the model. This occurs for the Lorenz or Rossler attractors, as explained in (Gao, Hu, et al. 2006). However, to reconstruct safely a chaotic attractor, the dimension of the lagged vectors should surpass twice the fractal dimension D_0 (Ott 1993; Cencini et al. 2010). For the VM, we have found that properly reconstructing the chaotic attractor requires at least 6 lagged coordinates. Six-dimensional CM trajectories contain self-intersections in dimension 2. Fig. 2.3(c) shows that the SDLE $\lambda(\epsilon)$ with $m = 6$ displays oscillations for different noise values, not a single plateau as in Fig. 2.3(b). Thus, we need a different algorithm to calculate the LLE from data. We have used the Gao-Zheng algorithm (Gao and Zheng 1994) that requires constructing a quantity $\Lambda(k)$ whose slope near the origin produces the LLE, see Appendix 2.B. These LLE yield the horizontal lines in Fig. 2.3(c), which coincide with the average values of the SDLE oscillations. The latter coincide with LLE calculated from Eq. (2.1) and increase with noise. Thus, noise enhances chaos in the noisy chaos region of Fig. 2.3(a), where there are the critical lines of the transition from chaos S-cluster to chaos M-cluster, $\beta = \beta_c(N, \eta)$. In the next section, we study the differences between these two chaotic regions. We note that there are independent characteristics of N so in the limit of infinite N it will be a phase transition defined in Chapter 3 as scale-free-chaos phase transition.

2.4 Phase transition and topological data analysis

The structure of clusters changes as β surpasses β_c , the critical confinement calculated from relaxation time. Fig. 2.4(a) shows the swarm particles and their short time trajec-

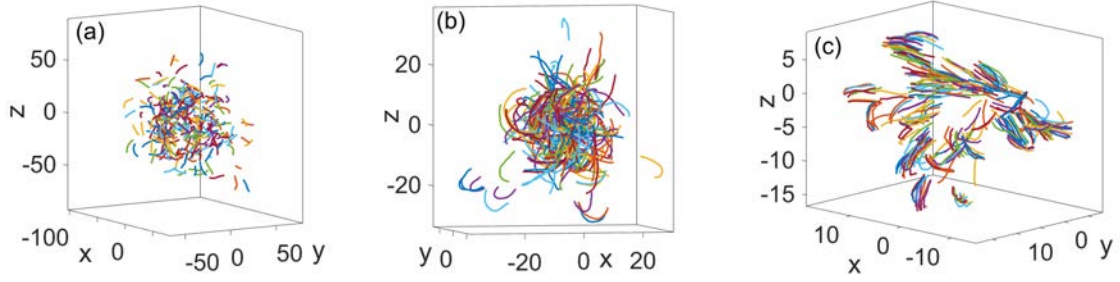


Figure 2.4: Chaotic swarms of $N = 300$ particles showing short trajectories of the particles for confinements near its critical value, $\beta = \beta_c(N; \eta)$ and $\eta = 0.5$: **(a)** Sparse single cluster chaos for $\beta < \beta_c(N; \eta)$, **(b)** compact single cluster chaos at $\beta = \beta_c(N; \eta)$, multi-cluster chaos for **(c)** $\beta > \beta_c(N; \eta)$.

ries for $\beta < \beta_c(N; \eta)$: the particles form a single cluster. Figs. 2.4(b) and 2.4(c) correspond to $\beta = \beta_c(N; \eta)$ and $\beta > \beta_c(N; \eta)$, respectively. For $\beta = \beta_c(N; \eta)$, the particles form a single cluster and fill a smaller volume, whereas for $\beta > \beta_c(N; \eta)$, the swarm has split in several clusters. The average polarization is very small for sparse single-cluster chaos, $\beta < \beta_c(N; \eta)$, and it increases with β in the multicluster chaotic region, $\beta > \beta_c(N; \eta)$, see Fig. 3.6.

These findings can be rendered more precise by *topological data analysis* (TDA) (Zomorodian et al. 2005; Edelsbrunner et al. 2010; Sinhuber et al. 2017). TDA borrows ideas from persistent homology, traditionally used to distinguish structures in low dimensional topological spaces (e.g., circle, annulus, sphere, torus, etc) by quantifying their connected components, topological circles, trapped volumes. For instance, given a point cloud $\mathbf{x}_1, \dots, \mathbf{x}_N$ in \mathbb{R}^3 , we can infer whether it represents a sphere or a torus by calculating the homologies H_0, H_1, H_2 , and the corresponding Betti numbers b_0, b_1, b_2 . The different homologies can be calculated regardless of the dimension of the underlying space, as long as a distance or metric is defined (Zomorodian et al. 2005).

We consider midges (or particles) as data points from a sampling of the underlying topological space of the swarm. Thus, we have a finite set of data points from a sampling of the underlying topological space. We measure data homology by creating connections between nearby data points, varying the scale over which these connections are made (as given by the *filtration parameter*), and looking for features that persist across scales (Zomorodian et al. 2005; Edelsbrunner et al. 2010). This can be achieved by building the *Vietoris-Rips complex* from all pairwise distances between points in the dataset. Assume spheres of diameter r circle each particle. For each value of the filtration parameter $r > 0$, we form a simplicial complex S_r by finding all gatherings of $k + 1$ points such that all pairwise distances between these points are smaller than r . Each such gathering is a k -simplex. The simplicial complex S_r comprises finitely many simplices such that (i) every nonempty subset of a simplex in S_r is also in S_r , and (ii) two k -simplices in S_r are either disjoint or intersect in a lower dimensional simplex. In S_r , 0-simplices are the data points, 1-simplices are edges, connections between two data points, 2-simplices are

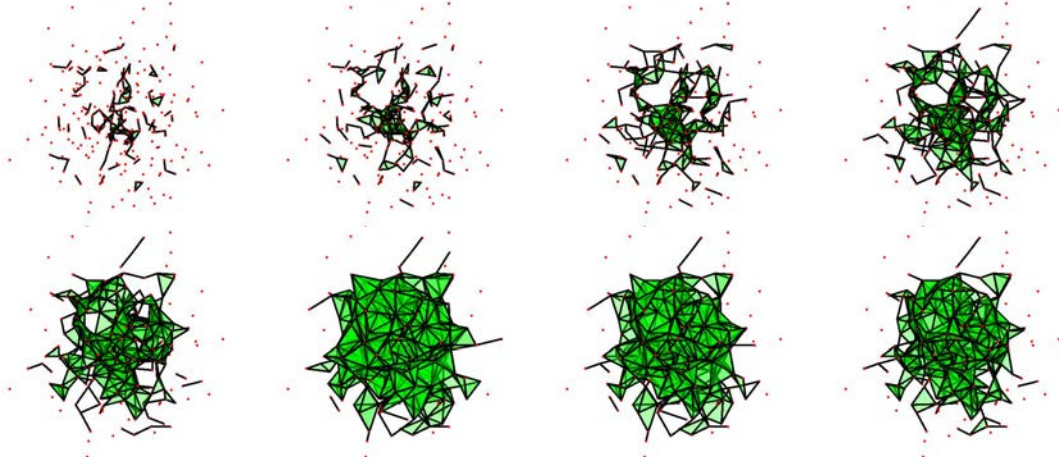


Figure 2.5: Simplices for filtration values $r = \frac{r_M}{2}\tilde{r}$, $\tilde{r} = 0.05, 0.06, 0.07, 0.08, 0.09, 0.1, 0.11, 0.12$ at a representative time of the swarm evolution. Here $r_M = 150.22$ is the maximum distance between two points in the cloud, $\beta = 0.001 < \beta_c(300) = 0.0075$. As r increases, a single dominant cluster absorbs neighboring points and small components becoming a large ‘compact’ component.

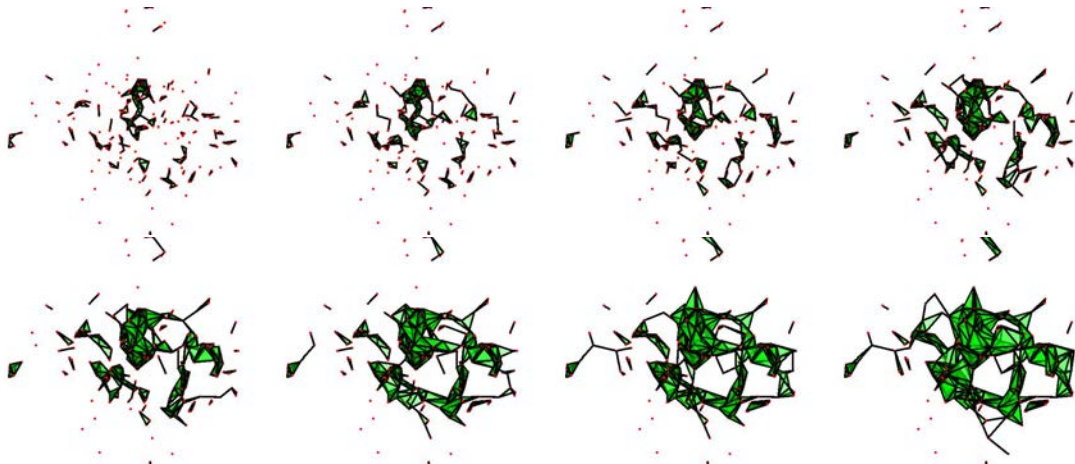


Figure 2.6: Same as Fig. 2.5 for $\beta = 0.025 > \beta_c(300)$ with $r_M = 33.48$. As r increases, small separated components form and eventually connect leaving large holes.

triangles formed by joining 3 data points through their edges, 3-simplices are tetrahedra, and so on. See Figs. 2.5 and 2.6, which are the counterparts of Figs. 2.4(a) and 2.4(c), respectively. These figures illustrate how TDA automatically characterizes the formation of a loose single swarm for $\beta < \beta_c$ and of several tight smaller clusters for $\beta > \beta_c$. In the latter case, the single cluster resulting for sufficiently large filtration parameter contains large holes.

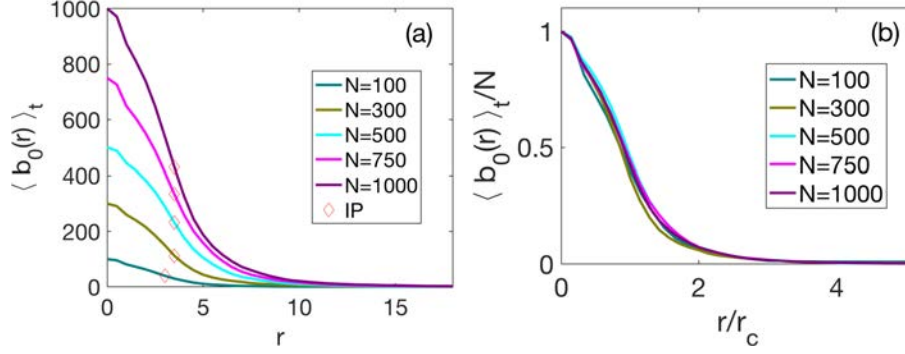


Figure 2.7: **(a)** Time averaged Betti number $\langle b_0 \rangle_t$ versus filtration parameter r for $\beta_c(N; \eta)$ and different N ; **(b)** Same for scaled averaged Betti number $\langle b_0 \rangle_t / N$ versus scaled filtration parameter r/r_c where $r_c(N)$ is the inflection point of each curve marked with diamonds in Panel (a). Here $\eta = 0.5$.

To quantify the topological structure of the swarm data points, the Betti numbers depicted in Fig. 2.7 are useful. Within the set of all k -simplices in S_r , we can distinguish closed submanifolds called k -cycles, and cycles called *boundaries* because they are also the boundary of a submanifold. A *homology class* is an equivalence class of cycles modulo boundaries. A homology class H_k is the set of independent topological holes of dimension k , represented by cycles which are not the boundary of any submanifold. The dimension of H_k is the k th *Betti number* b_k . For instance, b_0 is the number of connected components shown in Fig. 2.7, b_1 is the number of topological circles, b_2 is the number of trapped volumes, and so on. See Refs. (Zomorodian et al. 2005; Edelsbrunner et al. 2010) for precise definitions. At critical confinement, we can depict average Betti numbers, $\langle b_0 \rangle_t$ (number of connected clusters averaged over several time snapshots of the swarm), versus r for different N . These Betti numbers collapse when we rescale them using the inflection point of each curve (Sinhuber et al. 2017), $r_c(N)$; see Figs. 2.7(a) and 2.7(b).

Fig. 2.8 illustrates the trend to a more compact single swarm and to swarm splitting as β increases past its critical value. As r increases, the number of clusters with a single particle decrease monotonically, as seen in the upper panel of Fig. 2.8(a). However, the upper panel of Fig. 2.8(b) shows that the number of particles in the largest cluster increase monotonically for $\beta < \beta_c$ but it increases with plateaus and abrupt jumps for $\beta > \beta_c$. These abrupt features indicate that the largest cluster absorbs single particles as r increases if $\beta < \beta_c$, whereas several large clusters form and are abruptly absorbed by the largest

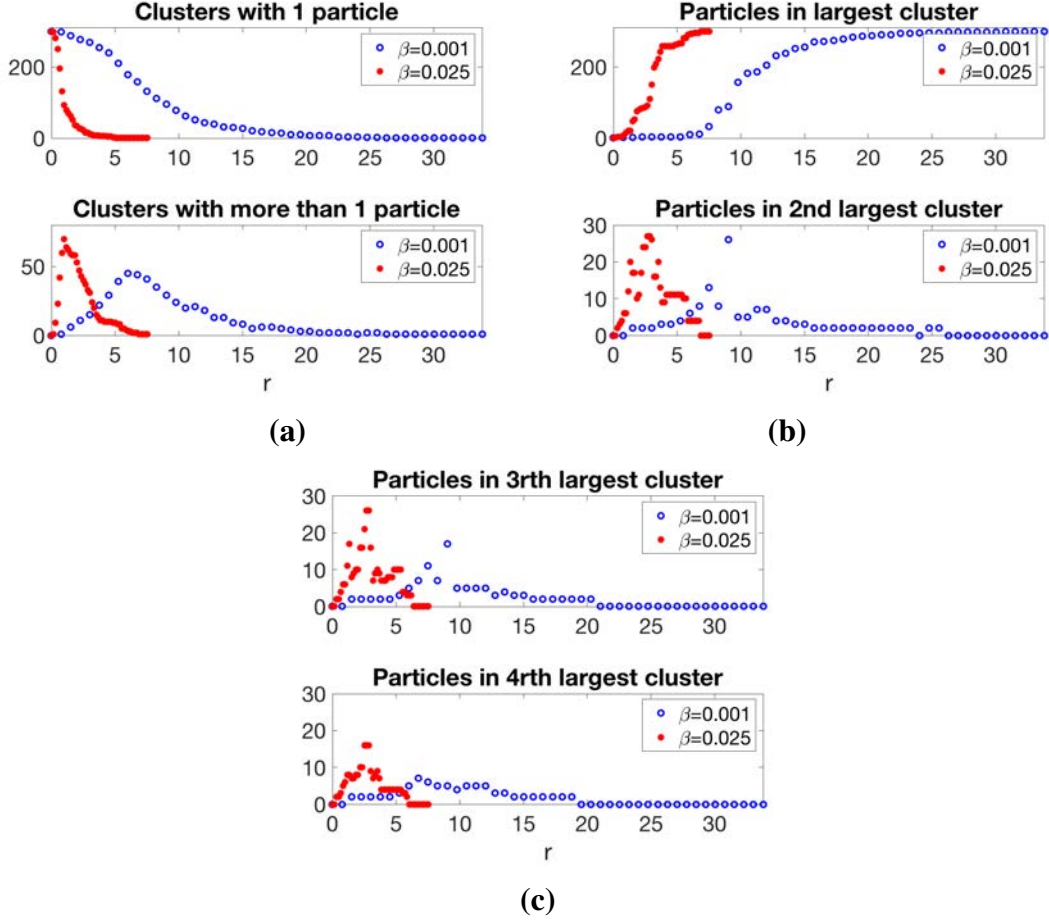


Figure 2.8: Hierarchical TDA clustering. **(a)** Number of clusters with 1 particle (up) and with more than 1 particle (down) for $\beta = 0.025$ (left red points) and $\beta = 0.001$ (right blue points) vs filtration parameter r at a single time. **(b)** Number of particles in (up) the largest cluster and (down) the second largest cluster vs r . **(c)** Number of particles in (up) the third largest cluster and (down) the fourth largest cluster vs r . Here $N = 300$ and $\eta = 0.5$.

cluster at particular values of r for $\beta > \beta_c$. The lower panels in Figs. 2.8(a)-2.8(b) confirm these observations. Clusters with more than one particle form gradually if $\beta < \beta_c$ and abruptly if $\beta > \beta_c$. The plateaus and jumps in the number of particles within the second, third and fourth largest clusters in Figs. 2.8(b) and 2.8(c) indicate absorption thereof by the largest cluster. These figures also illustrate the different cluster structure below and above the critical confinement β_c . When $\beta > \beta_c$, we observe the presence of several relevant clusters with a large number of particles. These clusters persist as the filtration parameter increases. Note that it is possible to have more than one cluster with the same number of particles.

2.5 Summary

In this chapter we use dynamical systems tools to understand the 3D VM confined by a harmonic potential. As the confinement strength decreases, the VM with fixed number of particles N displays a variety of periodic, quasiperiodic and chaotic attractors, which may be strongly modified by alignment noise. To distinguish chaos, we have calculated the largest Lyapunov exponent directly from the VM using the Benettin algorithm (Benettin et al. 1980). This is particularly well adapted to the discrete time dynamics of the VM. We have also calculated the LLE by reconstructing the attractor from time traces of the center of mass motion using lagged coordinates. Using only two lagged coordinates, scale-dependent Lyapunov exponents help distinguishing deterministic and noisy chaos from parameter regions where noise is dominant (Gao, Hu, et al. 2006). This is important because this transition exist within the noisy chaos region. While scale-dependent Lyapunov exponents give qualitative information, we need six lagged coordinates to faithfully reconstruct the chaotic attractor and obtain (by the Gao-Zheng algorithm in (Gao and Zheng 1994) the same LLEs as provided by the Benettin algorithm. This methodology will be important to ascertain whether a real system in nature exhibits chaotic dynamics, and even if it displays the transition from chaos S-cluster to chaos M-cluster and scale-free-chaos phase transitions as in the next chapter.

We find a transition from chaos to chaos never seen before. This transition for finite N changes from a scattered swarm to a swarm with different clusters. We characterise this transition with the TDA and observe that there is a collapse of the Betti number as a function of the filtering parameter with respect to different N . Moreover, its inflection point is invariant for large values of N . Thus in the limit $N \rightarrow \infty$ we conjecture that there is a phase transition with these characteristics. Works linking equilibrium phase transitions to topological changes of appropriate manifolds in the thermodynamic limit are (Franzosi et al. 2007a; Franzosi et al. 2007b; G. Pettini et al. 2019; Gori, Franzosi, G. Pettini, et al. 2022); see also (Kastner et al. 2011; Gori, Franzosi, and M. Pettini 2018).

Appendix 2.A Nondimensionalized equations of the confined Vicsek model

We consider the three-dimensional confined Vicsek model:

$$\begin{aligned} \mathbf{x}_i(t + \Delta t) &= \mathbf{x}_i(t) + \Delta t \mathbf{v}_i(t + \Delta t), \\ \mathbf{v}_i(t + \Delta t) &= v \mathcal{R}_\eta \left[\frac{\sum_{|\mathbf{x}_j - \mathbf{x}_i| < r_1 R_0} \mathbf{v}_j(t) - \beta_0 \mathbf{x}_i(t)}{\left| \sum_{|\mathbf{x}_j - \mathbf{x}_i| < r_1 R_0} \mathbf{v}_j(t) - \beta_0 \mathbf{x}_i(t) \right|} \right], \end{aligned} \quad (2.2)$$

where $\mathcal{R}_\eta(\mathbf{w})$ rotates the unit vector \mathbf{w} randomly within a spherical cone centred at it and spanning a solid angle in $(-\frac{\eta}{2}, \frac{\eta}{2})$ (Wang 1992). Initially, the particles are randomly placed within a sphere with unit radius and the particle velocities are pointing outwards.

We nondimensionalize the model using data from the experiments on midges reported in the supplementary material of Refs. (Attanasi, Cavagna, L. Del Castello, et al. 2014; Attanasi, Cavagna, L. D. Castello, et al. 2014; Cavagna, Conti, et al. 2017). We select the event labeled 20120910_A1 in Table I (Cavagna, Conti, et al. 2017). We measure times in units of $\Delta t = 0.24$ s, lengths in units of the time-averaged nearest-neighbor distance of the 20120910_A1 swarm, which is $r_1 = 4.68$ cm, and velocities in units of $r_1/\Delta t$, whereas $v = 0.195$ m/s. Then Eq. (2.1) is the nondimensional version of Eq. (2.2) with $\Delta t = 1$ and

$$v_0 = v \frac{\Delta t}{r_1}, \quad \beta = \beta_0 \Delta t. \quad (2.3)$$

For the example we have selected, $v_0 = 1$, whereas other entries in the same table produce order-one values of v_0 with average 0.53. For these values, the confined Vicsek model has the same behavior as described here. Thus, the Vicsek model describing midge swarms is far from the continuum limit $v_0 \ll 1$. Cavagna *et al* consider a much smaller speed, $v_0 = 0.05$, closer to the continuum limit where derivatives replace finite differences (Cavagna, Conti, et al. 2017).

Collective consensus is quantified by the polarization $W \in [0, 1]$:

$$W(t; \eta, \beta) = \left| \frac{1}{N} \sum_{j=1}^N \frac{\mathbf{v}_j(t)}{|\mathbf{v}_j(t)|} \right|. \quad (2.4)$$

The time average $\langle W \rangle_t$ coincides with the ensemble average of (2.4) by ergodicity.

Effect of the boundary conditions. In the standard VM, the particles are enclosed in a cubic box, the boundary conditions are periodic and the system is invariant under translations. On the other hand, in the confined VM, there are no boundaries, the particles are confined by a harmonic potential, and translation invariance is broken. There are many studies of the standard VM, which is not the case for the confined VM. In fact, the confined VM has time-dependent attractors that are different from those of the standard VM. Among them, chaotic attractors. Another qualitative difference between both VMs is that broken translation symmetry precludes particles filling uniformly the available space for the confined VM. Thus, the ordering transition of the periodic-box VM cannot be the same for the confined VM.

Appendix 2.B Chaotic and noisy dynamics

We calculate the LLE in different ways that are complementary to each other: (i) directly from the equations by using the Benettin *et al* (BA) algorithm (Benettin et al. 1980; Ott 1993; Cencini et al. 2010), (ii)-(iii) using from time traces of the center-of-mass motion or the NDCCF to reconstruct the phase space of the chaotic attractor. We need model equations to use the BA whereas time traces can be obtained from numerical simulations of equations or from experiments and observations. To obtain the LLE from time traces,

we have used (ii) the scale-dependent Lyapunov exponent (SDLE) algorithm (Gao, Hu, et al. 2006) and (iii) the Gao-Zheng algorithm (Gao and Zheng 1994). The SDLE algorithm is useful to separate the cases of mostly deterministic chaos from noisy chaos and mostly noise even in the presence of scarce data and a reconstruction of the attractor that is not very precise (Gao, Hu, et al. 2006) whereas the Gao-Zheng algorithm requires more data points (Gao and Zheng 1994). We now describe these different algorithms and illustrate the results they provide for the confined VM. In all cases, we eliminate the effects of initial conditions by leaving out the first 30000 time steps before processing the time traces.

2.B.1 Benettin algorithm

We have to simultaneously solve Eqs. (2.1) and the linearized equations

$$\delta\tilde{\mathbf{x}}_i(t+1) = \delta\tilde{\mathbf{x}}_i(t) + \delta\tilde{\mathbf{v}}_i(t+1), \quad i = 1, \dots, N, \quad (2.5a)$$

$$\delta\tilde{\mathbf{v}}_i(t+1) = v_0 \mathcal{R}_\eta \left[\left(\mathbb{I}_3 - \frac{[\sum_{|\mathbf{x}_j - \mathbf{x}_i| < R_0} \mathbf{v}_j(t) - \beta \mathbf{x}_i(t)]^T [\sum_{|\mathbf{x}_j - \mathbf{x}_i| < R_0} \mathbf{v}_j(t) - \beta \mathbf{x}_i(t)]}{|\sum_{|\mathbf{x}_j - \mathbf{x}_i| < R_0} \mathbf{v}_j(t) - \beta \mathbf{x}_i(t)|^2} \right) \cdot \frac{\sum_{|\mathbf{x}_j - \mathbf{x}_i| < R_0} \delta\tilde{\mathbf{v}}_j(t) - \beta \delta\tilde{\mathbf{x}}_i(t)}{|\sum_{|\mathbf{x}_j - \mathbf{x}_i| < R_0} \mathbf{v}_j(t) - \beta \mathbf{x}_i(t)|} \right], \quad (2.5b)$$

in such a way that the random realizations \mathcal{R}_η are exactly the same for Eqs. (2.1) and (2.5). The initial conditions for the disturbances, $\delta\tilde{\mathbf{x}}_i(0)$ and $\delta\tilde{\mathbf{v}}_i(0)$, can be randomly selected so that the overall length of the vector $\delta\chi = (\delta\tilde{\mathbf{x}}_1, \dots, \delta\tilde{\mathbf{x}}_N, \delta\tilde{\mathbf{v}}_1, \dots, \delta\tilde{\mathbf{v}}_N)$ equals 1. After each time step t , the vector $\delta\chi(t)$ has length α_t . At that time, we renormalize $\delta\chi(t)$ to $\hat{\chi}(t) = \delta\chi(t)/\alpha_t$ and use this value as initial condition to calculate $\delta\chi(t+1)$. With all the values α_t and for sufficiently large l , we calculate the Lyapunov exponent as

$$\lambda_1 = \frac{1}{l} \sum_{t=1}^l \ln \alpha_t, \quad (2.6)$$

$$\alpha_t = |\delta\chi(t)| = |(\delta\tilde{\mathbf{x}}_1(t), \dots, \delta\tilde{\mathbf{x}}_N(t), \delta\tilde{\mathbf{v}}_1(t), \dots, \delta\tilde{\mathbf{v}}_N(t))|,$$

Fig. 2.9 plots λ_1 versus l at critical confinement $\beta = \beta_c(N)$ showing convergence of the exponent for different values of N . For $N = 750$, Fig. 2.10(a) depicts the LLE versus l for different values of β whereas Fig. 2.10(b) fixes $\beta = \beta_c(750) = 0.0035$ and shows the LLE versus l for different values of N , including $N = 750$. The insets of these figures indicate that the LLE is not a monotonic function of either β or N .

2.B.2 Scale dependent Lyapunov exponents

We use scale dependent Lyapunov exponents (SDLE) from the CM motion to characterize deterministic and noisy chaos as different from noise (Gao, Hu, et al. 2006).

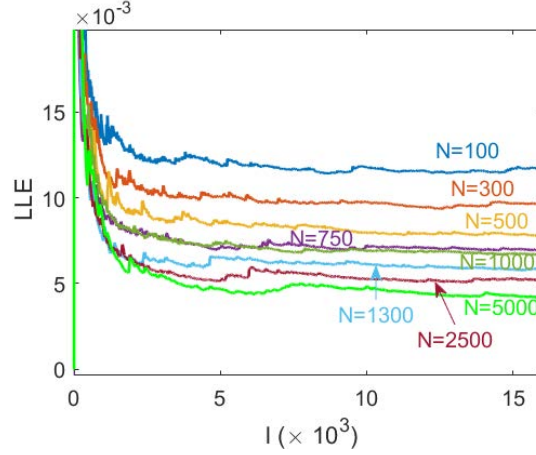


Figure 2.9: Largest Lyapunov exponent as a function of l as given by Eq. (2.6) for $\eta = 0.5$, $\beta = \beta_c(N)$ and different N

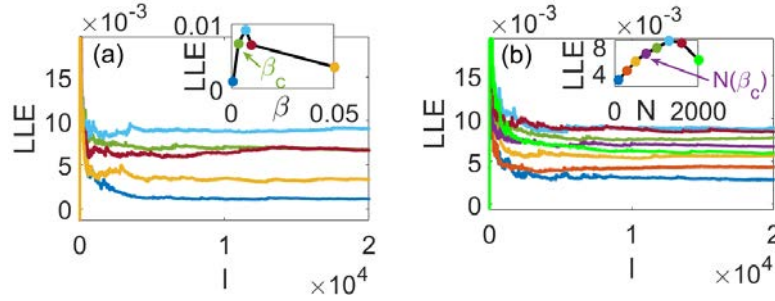


Figure 2.10: (a) LLE versus l as in Eq. (2.6) for $N = 750$ and $\beta = 0.001, 0.0035, 0.007, 0.01, 0.05$. Inset: LLE vs β ; marked: $\beta_c = 0.0035$. (b) LLE vs l for $\beta = 0.0035$ and $N = 100, 300, 500, 750, 1000, 1300, 1600, 2000$. Inset: LLE vs N for $\beta_c = 0.0035$; marked: $N = 750$. Here $\eta = 0.5$.

Adding the components of $\mathbf{X}(t)$, we form the time series $x(t) = X_1(t) + X_2(t) + X_3(t)$. To calculate the SDLE, we construct the lagged vectors: $\mathbf{X}_\alpha = [x(\alpha), x(\alpha + \tilde{\tau}), \dots, x(\alpha + (m-1)\tilde{\tau})]$. The simplest choice is $m = 2$ and $\tilde{\tau} = 1$ (other values can be used, see below). From this dataset, we determine the maximum ε_{\max} and the minimum ε_{\min} of the distances between two vectors, $\|\mathbf{X}_\alpha - \mathbf{X}_\beta\|$. Our data is confined in $[\varepsilon_{\min}, \varepsilon_{\max}]$. Let ε_0 , ε_t and $\varepsilon_{t+\Delta t}$ be the average separation between nearby trajectories at times 0, t , and $t + \Delta t$, respectively. The SDLE is

$$\ln \lambda(\varepsilon_t) = \frac{\ln \varepsilon_{t+\Delta t} - \ln \varepsilon_t}{\Delta t}. \quad (2.7a)$$

The smallest possible Δt is of course the time step $\tilde{\tau} = 1$, but Δt may also be chosen as an integer larger than 1. Gao *et al* introduced the following scheme to compute the SDLE (Gao, Hu, et al. 2006). Find all the pairs of vectors in the phase space whose distances are initially within a shell of radius ε_k and width $\Delta\varepsilon_k$:

$$\varepsilon_k \leq \|\mathbf{X}_\alpha - \mathbf{X}_\beta\| \leq \varepsilon_k + \Delta\varepsilon_k, \quad k = 1, 2, \dots \quad (2.7b)$$

We calculate the Lyapunov exponent as follows:

$$\lambda(\varepsilon_t) = \frac{\langle \ln \|X_{\alpha+t+\Delta t} - X_{\beta+t+\Delta t}\| - \ln \|X_{\alpha+t} - X_{\beta+t}\| \rangle_k}{\Delta t}, \quad (2.7c)$$

where $\langle \rangle_k$ is the average within the shell $(\varepsilon_k, \varepsilon_k + \Delta\varepsilon_k)$. The shell dependent SDLE $\lambda(\varepsilon)$ in Fig. 2.3(b) displays the dynamics at different scales for $\tilde{\tau} = 1$ and $m = 2$. (Gao, Hu, et al. 2006) Using 2 lagged coordinates produces plateaus having a value of $\lambda(\varepsilon)$ equal to the LLE of deterministic chaos. This value differs from the LLE calculated using the BA or a more appropriate reconstruction of the phase space involving more lagged coordinates (see below). However, the SDLE with $m = 2$ yields a qualitative idea of the effects of noise on chaos. In deterministic chaos, $\lambda(\varepsilon) > 0$ presents a plateau with ends $\varepsilon_1 < \varepsilon_2 \ll 1$, in noisy chaos, this plateau is preceded and succeeded by regions in which $\lambda(\varepsilon)$ decays as $-\gamma \ln \varepsilon$, whereas it shrinks and disappears when noise swamps chaos. As η increases, $\lambda(\varepsilon)$ first decays to a plateau for $\eta = 0.1$. A criterion to distinguish (deterministic or noisy) chaos from noise is to accept the largest Lyapunov exponent as the positive value at a plateau $(\varepsilon_1, \varepsilon_2)$ satisfying

$$\log_{10} \frac{\varepsilon_2}{\varepsilon_1} \geq \frac{1}{2}. \quad (2.7d)$$

For $\eta = 0.5$, the region where $\log_{10}(\varepsilon_2/\varepsilon_1) = 1/2$ is marked in Fig. 2.3(b) by vertical lines. Plateaus with smaller values of $\log_{10}(\varepsilon_2/\varepsilon_1)$ or their absence indicate noisy dynamics (Gao, Hu, et al. 2006). This occurs for $\eta = 1$. The ends of the interval $(0.1, 1)$ of noisy chaos are marked by two vertical dashed lines in Fig. 2.3(a).

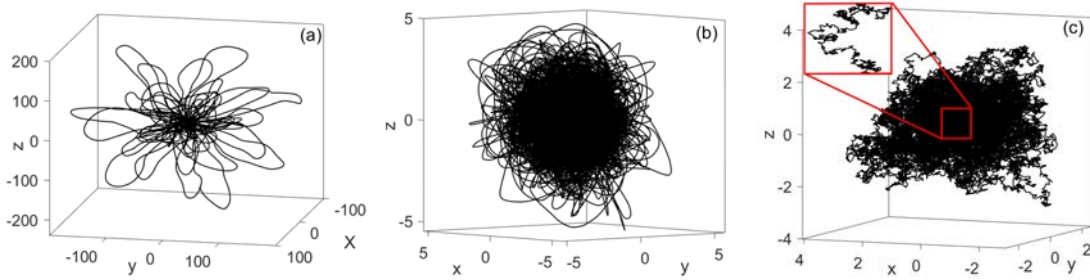


Figure 2.11: **(a)** Trajectory of the center of mass for $\eta = 0.01$, which corresponds to deterministic chaos with flower shape phase portrait. **(b)** Same for $\eta = 0.3$, which corresponds to noisy chaos: the trajectories of the center of mass cover more densely part of the space. **(c)** Predominantly noisy motion for $\eta = 5.5$. The trajectories from $t_0 = 1000$ to $t_f = 50000$ are depicted. Here, $N = 100, \beta = \beta_c$ for each η .

The chaotic dynamics of the swarm is reflected in quantities that depend on the positions and velocities of the particles. Important global quantities are the motion of the CM and the NDCCF of Eq. (3.1). Figs. 2.11 displays the CM trajectory, thereby visualizing the dynamics of the swarm. For increasing values of noise corresponding to the different

regions in Fig 2.3(a), the CM motion goes from deterministic chaos, Fig. 2.11(a), to noisy chaos, Fig. 2.11(b), to mostly noise, Fig. 2.11(c).

Note that all the plateaus in Fig. 2.3(b) produce the same positive value of the LLE $\lambda(\epsilon)$. This is not very realistic because the BA yields different values of the LLE depending on the noise strength η . Why? Recall that we have used $m = 2$ (two lagged coordinates) in the reconstruction of the attractor from the time traces. However, as shown in Fig. 3.3, the CM chaotic attractor has fractal dimension D_0 between 2 and 3, and we need $m \geq 2D_0$ to faithfully reconstruct the chaotic attractor (Ott 1993; Cencini et al. 2010). Thus, we need at least $m = 6$ to reconstruct it. Using $m = 6$ and its optimal value of $\tilde{\tau}$ (Gao and Zheng 1994) produces Fig. 2.3(c). Now $\lambda(\epsilon)$ presents large oscillations whose averages in the plateau regions coincide with the LLE as calculated by the Gao-Zheng algorithm (Gao and Zheng 1994).

2.B.3 Largest Lyapunov exponent from high dimensional reconstructions of CM motion

As explained above, the previous reconstruction of the phase space for CM motion used to calculate SDLE considers 2D lagged vectors ($m = 2$). This produces useful qualitative phase diagrams with flat plateaus, but the dimension of this vector space is too small to reconstruct faithfully the attractor. More realistic CM trajectories in higher dimension contain self-intersections in dimension 2. This explains the different values of the LLE found in the SDLE plateaus of Fig. 2.3(b) as compared with those found by the BA of Eq. (2.6). To reconstruct safely a chaotic attractor, the dimension of the lagged vectors should surpass twice the fractal dimension D_0 . (Ott 1993) For the confined VM, $m = 6$ is sufficient. However, the SDLE $\lambda(\epsilon)$ presents oscillations as indicated in Fig. 2.3(c) and their average values replace the plateaus in Fig. 2.3(b). In contrast with Fig. 2.3(b), the averaged oscillations produce LLEs that increase with noise. Averaging oscillations is not going to produce precise values of the LLE. Thus, we calculate the LLE from the lagged coordinates with $m = 6$ using the Gao-Zheng algorithm (Gao and Zheng 1994). This requires constructing the quantity $\Lambda(k)$ whose slope near the origin gives the LLE (Gao and Zheng 1994)

$$\Lambda(k) = \left\langle \ln \frac{\|X_{i+k} - X_{j+k}\|}{\|X_i - X_j\|} \right\rangle. \quad (2.8)$$

Here the brackets indicate ensemble average over all vector pairs with $\|X_i - X_j\| < r^*$ for an appropriately selected small distance r^* . Fig. 2.12 displays the graph of $\Lambda(k)$ given by Eq. 2.8. The slopes of $\Lambda(k)$ for different values of N at $\beta_c(N)$ equal the LLEs, increase with β and agree with the averaged oscillations marked in Fig. 2.3(c).

For different particle numbers with $\eta = 0.5$, Table 2.1 lists the LLEs calculated using the BA for the complete system as in Eq. (2.6), and using Eq. (2.8) for CM motion and

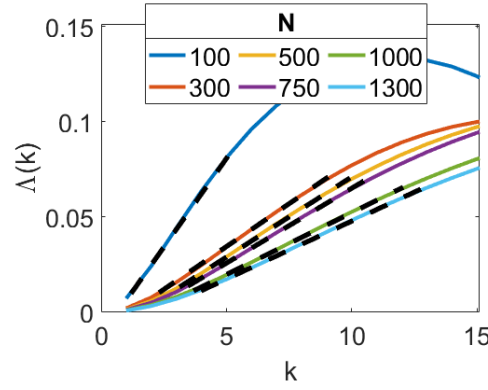


Figure 2.12: Plot of $\Lambda(k)$ vs k for different values of β . Thick dashed lines mark the slope of $\Lambda(k)$ for different values of N at $\beta_c(N)$.

N	100	300	500	750	1000	1300
BA	0.0118	0.0095	0.0078	0.0070	0.0067	0.0058
CM	0.017	0.0092	0.008	0.007	0.0063	0.0059
g(t)	0.0055	0.0044	0.0041	0.0038	0.0035	0.0033

Table 2.1: LLE for $\eta = 0.5$ and different N at $\beta_c(N; \eta)$ as calculated using the BA for the complete VM equations, Eq. (2.6), and Eq. (2.8) for CM motion and for the NDCCF $g(t)$ defined in Chapter 3. Note that the LLE as calculated using the BA and Eq. (2.8) for CM motion are similar whereas the LLE corresponding to the NDCCF $g(t)$ is smaller.

for the NDCCF $g(t)$ defined in Chapter 3. We observe that the LLE values calculated from the CM motion are similar to those found by the BA, whereas they are noticeably smaller if calculated for the NDCCF. While the NDCCF is still chaotic, we speculate that the subtraction of the CM motion and ensemble average involved in two-time NDCCF $g(t)$ dilute chaos by lowering the LLE. We observe that the difference between LLEs calculated from BA and CM motion and those from $g(t)$ in Table 2.1 decreases as N increases. Thus, it could happen that both sets of LLEs eventually converge to similar smaller values as $N \rightarrow \infty$ and chaos disappear.

Scale free chaos phase transition

3.1 Introduction

In the previous chapter we found and characterised a new transition. This critical line changes from single-cluster to multi-cluster, where both regions are chaotic. While this change is for finite N , there may be something similar in the thermodynamic limit uncovering a new chaotic phase transition.

In this chapter, we study the same 3D VM confined with large N . As the number of particles N increases, the first chaotic window begins at smaller values of β . Inside this window, we have found scale free chaos, for which the correlation length is proportional to the size of the swarm for increasing N , the polar order parameter is small and macroscopic quantities such as correlation length, susceptibility, dynamic correlation and the largest Lyapunov exponent exhibit power laws. The single-to-multicluster chaos line and critical region move to $\beta = 0$ as $N \rightarrow \infty$. Thus, we have found a scale-free-chaos phase transition. At the end of the first chaotic window, we have found a different phase transition to infinitely dense clusters of finite size that is reminiscent of gravitational collapse (Gundlach et al. 2007; Alberti et al. 2020; Chavanis et al. 2020). The finite size clusters of infinitely many particles may be termed *flocking black holes*. As $N \rightarrow \infty$, the critical line for collapse to them occurs for $\beta \rightarrow \infty$.

The rest of the chapter is as follows. Section 3.2 uses ideas from statistical physics, modified correlation functions, and finite-size scaling to obtain the main results of the first topic of the thesis: the existence of a line of phase transitions within the noisy chaos region of the parameter space. Section 3.3 describes a different phase transition from multicluster chaos to the formation of clusters of finite size and infinite particle density reminiscent

of gravitational collapse (Gundlach et al. 2007; Alberti et al. 2020; Chavanis et al. 2020). Section 3.4 discusses our findings and it contains our conclusions. Section 3.5 contains a summary of the chapter. The Appendices are devoted to technical matters. Appendix 3.A discusses dynamic and static correlation functions, how to calculate them and different definitions of critical lines at finite number of particles. Appendix 3.B discusses two solvable examples illustrating the relation between susceptibility and correlation time.

3.2 Phase transitions within regions of chaos

Insect swarms have a small polarization order parameter and exhibit strong correlations (Attanasi, Cavagna, L. Del Castello, et al. 2014; Attanasi, Cavagna, L. D. Castello, et al. 2014). To previous authors, this suggests that insect swarms may be on the disordered side, close to the ordering transition of the standard VM with periodic boundary conditions for sufficiently small box size (Attanasi, Cavagna, L. Del Castello, et al. 2014; Attanasi, Cavagna, L. D. Castello, et al. 2014). Beyond a certain box size, the ordering transition changes from continuous to discontinuous (Grégoire et al. 2004; Chaté and Mahault 2019; Chaté 2013). The reason is that the uniform ordered phase issuing continuously from the uniform disordered phase (Bertin et al. 2006; Ihle 2011; Bonilla and Trenado 2018; Bonilla and Trenado 2019) is unstable for wavenumbers below a certain value (Bertin et al. 2009). Consideration of the standard VM for small boxes implies an almost uniform disordered ‘gas’ phase (Chaté and Mahault 2019; Chaté 2013), despite experimental evidence that real insect swarms form a ‘condensed nucleus’ far from walls surrounded by a ‘vapor’ phase (Sinhuber et al. 2017). We shall show later that swarms described by the confined VM near scale-free-chaos phase transitions also have a small polarization, have a condensed nucleus surrounded by a particle ‘vapor’, and exhibit strong correlations.

Cavagna *et al* have used data extracted from observations of natural swarms to calculate static and dynamic correlation functions and found power law behavior for susceptibility, correlation length and the dynamic correlation function (Attanasi, Cavagna, L. Del Castello, et al. 2014; Attanasi, Cavagna, L. D. Castello, et al. 2014; Cavagna, Conti, et al. 2017). Their work indicates that the Fourier transform of the dynamic connected correlation function (DCCF) is the key tool to find power laws and critical exponents from experimental data (Cavagna, Conti, et al. 2017; Cavagna, Giardina, et al. 2018):

$$\hat{C}(k, t) = \left\langle \frac{1}{N} \sum_{i,j=1}^N \frac{\sin(kr_{ij}(t_0, t))}{kr_{ij}(t_0, t)} \delta \hat{\mathbf{v}}_i(t_0) \cdot \delta \hat{\mathbf{v}}_j(t_0 + t) \right\rangle_{t_0} \quad (3.1)$$

Here k , $r_{ij}(t_0, t)$, \mathbf{V} , $\delta \mathbf{v}_i = \mathbf{v}_i - \mathbf{V}$, $\delta \hat{\mathbf{v}}_i = \delta \mathbf{v}_i / \sqrt{\frac{1}{N} \sum_j |\delta \mathbf{v}_j|^2}$ are the wavenumber, the distance between particles i and j at different times (particle positions are calculated in the center of mass reference frame), the center of mass velocity, the relative velocity, and the dimensionless velocity fluctuation of the i th particle, respectively. The brackets in (3.1)

indicate an average over the earlier time t_0 and an ensemble average over random initial conditions (Cavagna, Conti, et al. 2017). See Appendix 3.A for details.

For natural swarms and their numerical simulations, conservation of the number of particles requires adapting the statistical mechanics definitions of equilibrium correlation functions, correlation length and susceptibility, (Huang 1987; Amit et al. 2005); see (Cavagna, Giardina, et al. 2018). The equilibrium static connected correlation function (SCCF) $\hat{C}(k, 0)$ reaches a maximum at $k = 0$, which is the susceptibility (Amit et al. 2005). However, Eq. (3.1) yields $\hat{C}(0, 0) = 0$. For finite N and near a phase transition, $\hat{C}(k, 0)$ reaches a maximum at a critical wavenumber $k_c > 0$. This maximum is the susceptibility χ , which tends to infinity as $N \rightarrow \infty$ at the critical point (Cavagna, Giardina, et al. 2018). The FSS hypothesis implies that $k_c \xi$ (ξ is the correlation length) is a number of order 1 and a possible choice is $\xi = 1/k_c$ (Cavagna, Giardina, et al. 2018).

How do we obtain the critical confinement $\beta_c(N, \eta)$? From the theory of equilibrium phase transitions, we would expect: (i) the maximum and the inflection point of the SCCF versus β tend to infinity as $N \rightarrow \infty$ for fixed alignment noise; (ii) the correlation (relaxation) time of the DCCF at wavenumber k_c tends to infinity as $N \rightarrow \infty$ (critical slowing down). See two solvable examples illustrating the relation between susceptibility and correlation time in Appendix 3.B. We will use criteria (i) and (ii) to identify lines of transitions in the chaotic phases of the confined VM.

Numerical evidence for $100 \leq N \leq 5000$ suggests that these lines move to $\beta = 0$ as $N \rightarrow \infty$. Without confinement, the LLE vanishes and chaos disappears. This is corroborated by a different argument (Bohr 1990). The correlation length ξ is bound by the finite velocity of propagation c multiplied by the time it takes two points to move exponentially far from each other, i.e., $1/\lambda_1$:

$$\xi \leq \frac{c}{\lambda_1}. \quad (3.2)$$

Thus, a phase transition with infinite correlation length can only occur for $\lambda_1 = 0$ (Bohr 1990; Cross et al. 1993). As $N \rightarrow \infty$, these lines all go to $\beta = 0$ at the same rate, thereby characterizing a unique scale-free-chaos phase transition at $N = \infty$. By an abuse of notation, we also denote $\beta_c(N, \eta)$ and the other critical lines (see below) at finite N as “lines of phase transitions”.

3.2.1 Critical confinement from correlation time

Correlation time

For the DCCF, the dynamic scaling hypothesis implies

$$\frac{\hat{C}(k, t)}{\hat{C}(k, 0)} = f\left(\frac{t}{\tau_k}, k\xi\right) = g(k^\zeta t, k\xi); \quad g(t) = \frac{\hat{C}(k_c, t)}{\hat{C}(k_c, 0)}, \quad (3.3)$$

with $k_c = \text{argmax}_k \hat{C}(k, 0)$. Here z is the dynamic critical exponent and $\tau_k = k^{-z} \phi(k\xi)$ is the correlation time of the normalized DCCF (NDCCF) (3.3) at wavenumber k obtained by solving the equation: (Cavagna, Conti, et al. 2017; Halperin et al. 1969)

$$\sum_{t=0}^{t_{max}} \frac{1}{t} \sin\left(\frac{t}{\tau_k}\right) f\left(\frac{t}{\tau_k}, k\xi\right) = \frac{\pi}{4}. \quad (3.4)$$

In Eq. (3.4), t_{max} is the maximum time in experiments or in VM simulations (Cavagna, Conti, et al. 2017). For pure exponential relaxation near an equilibrium phase transition, τ_k obtained by solving Eq. (3.4) equals the relaxation time (Cavagna, Conti, et al. 2017; Halperin et al. 1969). The NDCCF of a chaotic attractor first relaxes rapidly and then it exhibits damped oscillations as time elapses, cf. Fig. 3.1(a). The rapid relaxation of $g(t)$ at short times is reminiscent of behavior near equilibrium phase transitions captured by Eq. (3.4).

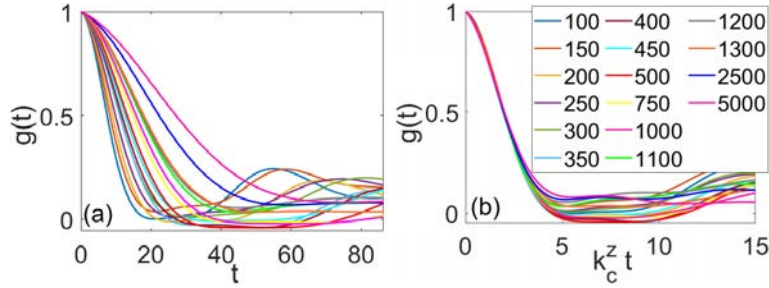


Figure 3.1: Dynamic scaling of the NDCCF. $g(t)$ versus (a) t , and (b) $k_c^z t$, for $\beta = \beta_c$ and the different values of N listed in the inset and $z \approx 1$. Here $\eta = 0.5$.

In simple models such as a damped harmonic oscillator forced by white noise, the DCCF has poles whose real parts also appear as reciprocal relaxation times in time dependent exponentials; see Appendix 3.B. The SCCF contains the same poles and one of them has zero real part at the beginning of instabilities. In second order equilibrium phase transitions, one vanishing pole corresponds to a diverging susceptibility maximum and marks the critical temperature in the thermodynamic limit. Similarly, the reciprocal relaxation-correlation time of the DCCF vanishes at the critical temperature and can also be used to find it. Thus, in principle we could find the critical value of the confinement by finding the susceptibility maximum or, equivalently, the maximum correlation time. At the thermodynamic limit, the susceptibility becomes infinite and so does the correlation time (critical slowing down). We now use the same ideas to find the equivalent correlation time for the confined VM. A caveat is in order. Due to conservation of particles, $\hat{C}(0, 0) = 0$ and the definition of susceptibility used in equilibrium statistical mechanics has to be changed for the VM; see Appendix 3.A. That the real parts of the poles of the susceptibility are proportional to reciprocal correlation times is no longer guaranteed; see Appendix 3.B.

Let us endeavor to give a physical interpretation of τ_{k_c} , the correlation time at $k_c \sim 1/\xi$. At fixed noise η , Fig. 3.2(a) displays the smallest time $t_m(\beta, N)$ at which $\hat{C}(k_c, t) = 0$ and the correlation time τ_{k_c} as functions of β for $N = 100, 200, 400$. The time $t_m(\beta, N)$ seems a reasonable choice for the correlation time but it varies with β . The maximal possible correlation time $t_m(\beta, N)$ would correspond to the largest negative real part of the eigenvalue posed by our hypothetical linear stability criterion. It turns out that $t_m(\beta, N)$ increases abruptly for a certain value β_c at which τ_{k_c} is essentially minimum; see Fig. 3.2(a). Thus, $\beta = \beta_c$ marks the largest possible correlation time based on the extension of $t_m(\beta, N)$ for $\beta \leq \beta_c$. Alternatively, the minimum value of τ_{k_c} given by Eq. (3.4) and reached for $\beta = \beta_c$, marks the same correlation time. Fig. 3.2(b) shows that the minimum of τ_{k_c} follows a power law $\tau_{k_c} \sim k^{-z}$, with exponent $z = 1.01 \pm 0.01$. For $N = 100$, Fig. 3.2(c) shows that, at β slightly larger than β_c , the first local minimum of $\hat{C}(k_c, t)$ becomes positive and the minimum t_m having $\hat{C}(k_c, t) = 0$ jumps to a much larger value. This explains the abrupt jump of $t_m(\beta, N)$ at $\beta = \beta_c$, which corresponds to the dashed line in Fig. 3.2(a). As $N \rightarrow \infty$, $\beta_c \rightarrow 0$ and the characteristic timescale tends to infinity (critical slowing down). Fig. 3.2(c) also shows that the correlation length decreases and the time averaged polarization $\langle W \rangle_t$, where W is defined by

$$W(t; \eta, \beta) = \left| \frac{1}{N} \sum_{j=1}^N \frac{\mathbf{v}_j(t)}{|\mathbf{v}_j(t)|} \right|, \quad (3.5)$$

(cf Appendix 2.A), decreases as the confinement decreases.

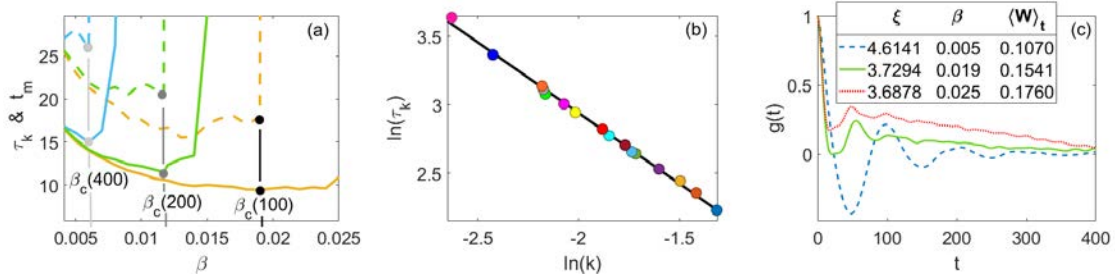


Figure 3.2: **(a)** Smallest time $t_m(\beta; N)$ such that $g(t_m) = 0$ (dashed curves) and characteristic timescale $\tau_{k_c}(\beta; N)$ (continuous curves) as functions of β for $N = 100, 200, 400$. The minimum characteristic timescale is close to the abrupt growth of $t_m(\beta; N)$ and marks the scale-free-chaos phase transition. **(b)** Characteristic timescale, τ_k , computed at $k_c = 1/\xi$ for different N , as a function of k (log-log scale): $\tau_{k_c} \sim k_c^{-z}$ with $z = 1.01 \pm 0.01$. **(c)** Normalized DCCF vs nondimensional time for different confinement values marked and $N = 100$. The inset lists the values of β , correlation length ξ and time averaged polarization $\langle W \rangle_t$ for the three curves $g(t)$. In this figure, $\eta = 0.5$.

Collapse of the NDCCF

We have obtained a power law $\tau_{k_c} \sim k_c^{-z}$ with $z = 1.01 \pm 0.01$ for $k_c \xi = 1$, as shown in Fig. 3.2(b). For this value of z , Fig. 3.1(b) illustrates how NDCCF curves $g(t)$ collapse to

a single one in terms of $k_c^z t$ at the scale-free chaos line for $0 < k_c^z t < 4$. Moreover, NDCCF curves drop to values close to zero for $k_c^z t > 5$ but they do not collapse for those larger times unlike critical behavior near equilibrium phase transitions. *What happens?* We surmise that some regions of the chaotic attractors are much more frequently visited than others, which indicates that different length and time scales coexist within the attractor. This can be ascertained by finding the multifractal dimension D_q . After a long transient (30000 time steps), a set of M values of the CM position $\vec{x}_i = \mathbf{X}(t_i)$, $i = 1, \dots, M$, form a Poincaré map of the attractor. Then we define the multifractal dimension D_q (Grassberger et al. 1983; Pawelzik et al. 1987; Bulashenko et al. 1999),

$$D_q = \frac{1}{q-1} \lim_{r \rightarrow 0} \frac{\ln[C_q(r)]}{\ln(r)}, \quad (3.6)$$

$$C_q(r) = \frac{1}{M} \sum_{i=1}^M \left[\frac{1}{M} \sum_{j=1}^M \theta(r - |\vec{x}_i - \vec{x}_j|) \right]^{q-1}, \quad (3.7)$$

where $\theta(x)$ is the Heaviside unit step function, $M \approx 70000$, and $C_q(r)$ is the generalized correlation function. D_0 , D_1 and D_2 are the box counting (capacity) dimension, the information dimension and the correlation dimension, respectively. As we vary q , different regions of the attractor will determine D_q . D_∞ corresponds to the region where the points are mostly concentrated, while $D_{-\infty}$ is determined by the region where the points have the least probability to be found. If D_q is a constant for all q , the CM trajectory will visit different parts of the attractor with the same probability and the point density is uniform in the Poincaré map. This type of attractor is called trivial, whereas a non constant D_q characterizes a nontrivial attractor with multifractal structure. Fig. 3.3 shows that the box-counting dimension D_0 and D_q for $q > 0$ undergo a downward trend with increasing N (decreasing β_c). Then the dimension of the more commonly visited sites of the attractor decreases. Furthermore, we shall see below that the positive LLE tends to zero and chaos disappears as $\beta \rightarrow 0$. However, the chaotic attractor remains multifractal: different time scales persist (Cencini et al. 2010). Thus, a single rescaling of time as in Fig. 3.1(b) cannot collapse the full NDCCF in our simulations. Curiously, the same collapse of the NDCCF as a function of $k_c^z t$ only for $0 < k_c^z t < 4$ occurs using data from natural swarms, as shown in Figures 2a and 2b of (Cavagna, Conti, et al. 2017) for $z = 1.2$ (experimental data yield $z = 1.12 \pm 0.16$, using the power law $\tau_{k_c} \sim k_c^{-z}$, (Cavagna, Conti, et al. 2017)).

Critical exponents

Having found the critical confinement $\beta_c(N; \eta)$ as the value of β for which τ_{k_c} is minimum, we can find the power laws and the critical exponents for the correlation length, susceptibility, time-averaged polarization order parameter, and the LLE λ_1 in terms of $\beta = \beta_c(N; \eta)$:

$$\chi(\beta, N, \eta) \equiv \max_r Q(r) \sim \beta^{-\gamma}, \quad \xi \equiv \operatorname{argmax}_r Q(r) \sim \beta^{-\nu}, \quad (3.8)$$

$$\lambda_1 \sim \beta^\varphi \sim N^{-\frac{\varphi}{3\nu}}, \quad \langle W \rangle_t \sim \beta^b, \quad (3.9)$$

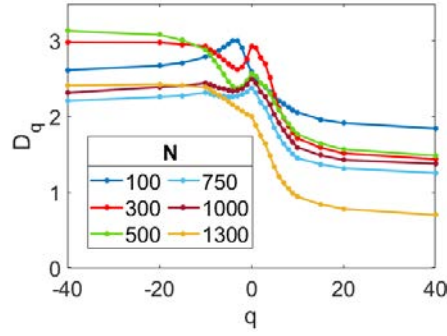


Figure 3.3: Multifractal dimension (Bulashenko et al. 1999) D_q vs q at $\beta_c(N; \eta = 0.5)$.

as $\beta = \beta_c(N; \eta) \rightarrow 0$ with $N \gg 1$. Here $Q(r)$ is the cumulative real-space correlation function, which we define below.

Real space susceptibility

To calculate the susceptibility, we have used the maximum of the cumulative real-space correlation function (corresponding to the first zero r_0 of the real-space correlation function, which is now the correlation length) at $\beta_c(N; \eta)$ (Attanasi, Cavagna, L. Del Castello, et al. 2014; Attanasi, Cavagna, L. D. Castello, et al. 2014):

$$Q(r) = \frac{1}{N} \sum_{i=1}^N \sum_{j \neq i}^N \delta \hat{\mathbf{v}}_i \cdot \delta \hat{\mathbf{v}}_j \theta(r - r_{ij}). \quad (3.10)$$

As shown in Appendix 3.A, selecting $\hat{C}(k_c, 0)$ as the susceptibility does not produce a monotonic function of β_c or of N . Thus, $\hat{C}(k_c, 0)$ cannot be used to fit a power law over an extended range. However, $1/k_c$ and r_0 are linearly related, and using either one as correlation length yields the same critical exponent ν ; see Appendix 3.A. A similar relation between $1/k_c$ and r_0 also holds for midge data; see Fig. SF1 of (Cavagna, Conti, et al. 2017). To calculate the LLE we can use the Benettin algorithm for the VM of Eq. (2.1) or a convenient time series obtained from the simulations, e.g., the CM evolution or the NDCCF; see Appendix 2.B.

Figs. 3.4(a) and 3.4(b) depict how correlation length and real-space susceptibility scale with β and Fig. 3.4(c) confirms that the correlation length is proportional to the size of the swarm. For $\eta = 0.5$, we obtain the critical exponents $\nu = 0.436 \pm 0.009$ and $\gamma = 0.92 \pm 0.05$, respectively. Fig. 3.4(d) shows that the correlation length decreases with alignment noise at critical confinement. Correlation length values in the region of noisy chaos are ξ times 4.68 cm, and they are compatible with observations of natural swarms (Attanasi, Cavagna, L. Del Castello, et al. 2014; Attanasi, Cavagna, L. D. Castello, et al. 2014; Cavagna, Conti, et al. 2017).

Another feature of swarm data compatible with our numerical simulations of the confined VM is that the NDCCF is flat at the origin. Referred to Eq. (3.3), we define the

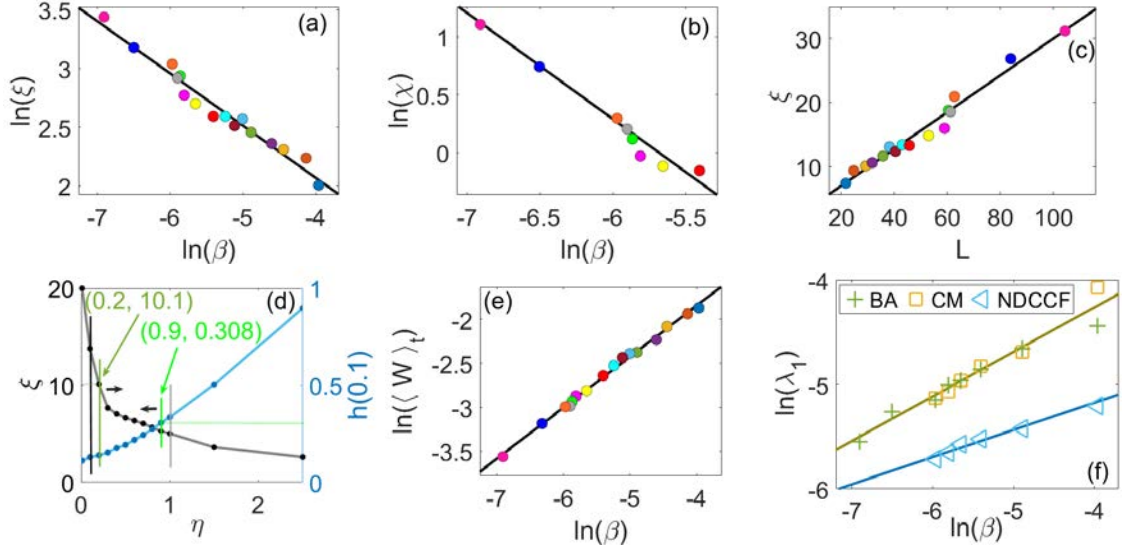


Figure 3.4: **(a)** Scaling of the dimensionless correlation length with β : $\xi \sim \beta^{-\nu}$, $\nu = 0.436 \pm 0.009$. **(b)** Scaling of the real-space susceptibility with β : $\chi \sim \beta^{-\gamma}$, $\gamma = 0.92 \pm 0.05$ for $N = 500, 750, 1000, 1100, 1200, 1300, 2500, 5000$. **(c)** The correlation length increases linearly with L . **(d)** Correlation length $\xi = r_0$ and NDCCF flatness $h(0.1)$ vs noise. Black vertical bars delimit the region of noisy chaos, occurring for smaller noise values than the ordering transition (Attanasi, Cavagna, L. Del Castello, et al. 2014; Attanasi, Cavagna, L. D. Castello, et al. 2014; Cavagna, Conti, et al. 2017). Green vertical bars are compatible with observations of natural swarms: the leftmost bar marks the largest observed correlation length and the rightmost bar marks when NDCCF flatness ends. **(e)** Time averaged polarization versus β : $\langle W \rangle_t \sim \beta^b$, $b = 0.58 \pm 0.01$. **(f)** LLE vs β for different N , $\lambda_1 \sim \beta^\varphi$, calculated by the Benettin algorithm (Benettin et al. 1980) for the complete system (crosses), from CM motion (squares) and from the NDCCF (triangles). We get $\varphi = 0.43 \pm 0.03$ (crosses and squares), and $\varphi = 0.24 \pm 0.02$ (triangles). In Panels (a), (c) and (e), N values are as in Fig. 3.1(b), $\eta = 0.5$.

‘flatness’ function as

$$h(x) = -\frac{1}{x} \ln f(x, 1), \quad x = \frac{t}{\tau_k}, \quad (3.11)$$

for a fixed value of the noise η . A perfectly flat NDCCF implies that $h(0) = 0$. However, $h(x)$ from experiments changes abruptly below $x = 0.1$ as shown in Fig. 3b of (Cavagna, Conti, et al. 2017). The same figure yields an upper value 0.3 of $h(0.1)$ for natural swarms, which we arbitrarily select as the transition value from flat to non-flat NDCCF. For the confined VM, the transition value occurs at $\eta = 0.9$ in Fig. 3.4(d), which is close to the change to noise from noisy chaos in Fig. 2.3(a). Fig. 3.4(d) shows that the correlation length decreases and $h(0.1)$ increases with increasing η . Thus, observed correlation lengths and flat NDCCFs occur in the region of noisy chaos of the confined VM that contains the scale-free-chaos phase transitions. Fig. 3.4(e) depicts the power law of the time-averaged polar order parameter $\langle W \rangle_t$ versus β , which shows the scale-free-chaos phase transition to be of second order with critical exponent $b = 0.58 \pm 0.01$.

Bound for the LLE critical exponent

The LLE λ_1 decreases as $\beta_c(N; \eta)$ does according to the power law (3.9) with critical exponent $\varphi = 0.43 \pm 0.03$ provided the LLE is calculated using the Benettin algorithm on Eq. (2.1) or time traces of the CM as explained in Appendix 2.B. See Fig. 3.4(f). For chaotic systems with short range interactions such as the confined VM, Eq. (3.2) together with Eqs. (3.8) and (3.9) imply that $\beta^{\varphi-\nu} \leq c$. To be consistent as $\beta \rightarrow 0$, this relation then implies

$$\varphi \geq \nu. \quad (3.12)$$

Were the dynamic scaling of (3.3) to hold for all time, $e^{\lambda_1 t}$ would be a function of $k^z t$; therefore $\lambda_1 \sim k_c^z \sim \beta^{z\nu}$, and $\varphi = z\nu$. Eq. (3.12) then produces $z \geq 1$, which agrees with all our simulations carried out with the Benettin algorithm or reconstructing the chaotic attractor from center of mass data. Thus, $\varphi \approx z\nu \geq \nu$ approximately holds for one-time functions such as the center of mass trajectory with $\eta = 0.5$. However, this relation fails for the two-time NDCCF, which has a smaller φ ; see Fig. 3.4(f).

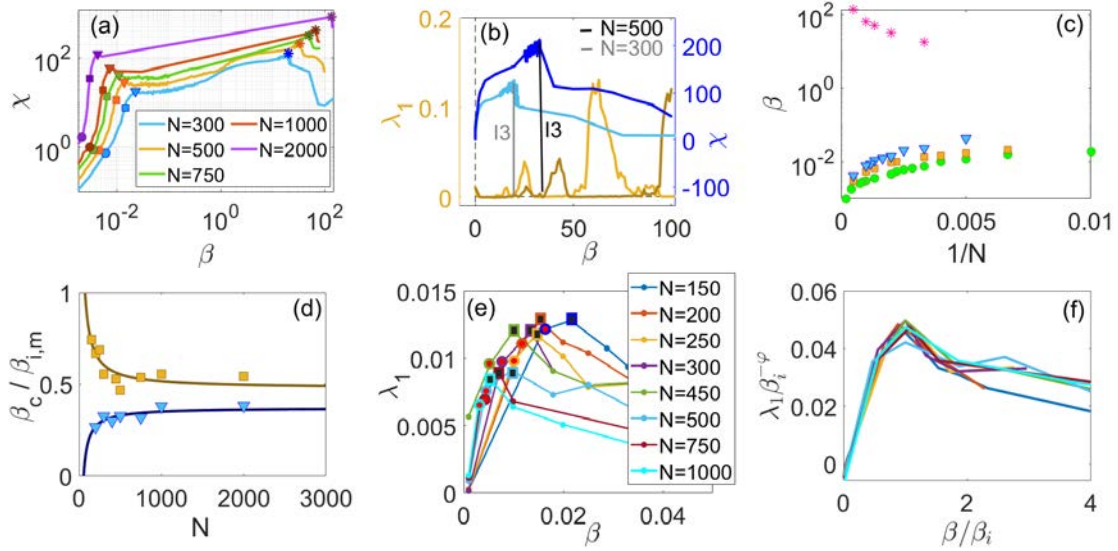


Figure 3.5: (a) Real-space susceptibility (log-log scale) for $N = 300, 500, 750, 1000, 2000$. (b) LLE and susceptibility versus β for $N = 300, 500$. Circles, squares, triangles and asterisks mark β_c , β_i , β_m (local χ maximum), and β_M (global χ maximum of the susceptibility, at the beginning of the third chaotic window, marked by I3 in Panel b), respectively. (c) β_c , β_i , β_m , and β_M versus $1/N$. (d) Ratios $\beta_c/\beta_i = 0.48 + 37.76/N$ and $\beta_c/\beta_m = 0.37 - 20.48/N$ as $N \gg 1$. (e) LLE versus β for N marked in the inset. (f) Same as Panel (e) with axes $\lambda_1/\beta_i^{\varphi_i}$ and β/β_i , $\varphi_i = 0.33$, showing collapse of curves. Circles correspond to the critical confinement $\beta_c(N; \eta)$, squares correspond to the inflection point of the susceptibility $\beta_i(N; \eta)$. Here $\eta = 0.5$.

3.2.2 Critical confinement from the static correlation

At critical confinement, the susceptibility $\chi = \max_r Q(r)$, given by Eqs. (3.8) and (3.10) for fixed $\beta_c(N; \eta)$, η and N , becomes infinity as $N \rightarrow \infty$. For given values of the alignment noise η , we can find other values of β , e.g., the local maximum and the inflection point of $\chi = \chi(\beta, N; \eta)$ as a function of β , which also tend to infinity as $N \rightarrow \infty$. At finite N , these confinement values, $\beta_i(N; \eta)$ (inflection) and $\beta_m(N; \eta)$ (local maximum), are different from $\beta_c(N; \eta)$, as shown in Fig. 3.5(a). Fig. 3.5(b) shows that there are different regions of positive LLE separated by non-chaotic regions. The first chaotic window starts at very small positive values of β that cannot be appreciated at the scale of the figure. The global maximum of the susceptibility is reached at large values of β corresponding to the beginning of the third chaotic window in Fig. 3.5(b), which is different from the scale-free chaos window of $\beta_c, \beta_i, \beta_m$. Unlike the isolated β_M , the values β_c, β_i and β_m tend to 0 as $N \rightarrow \infty$, as observed in Fig. 3.5(c). Fig. 3.5(d) shows that the ratios β_c/β_i and β_c/β_m tend to constant values (about 0.48 and 0.37, respectively) as $N \rightarrow \infty$. Thus, for sufficiently large N , the critical exponents are the same for the lines $\beta_c, \beta_i, \beta_m$ and therefore they correspond to the same phase transition.

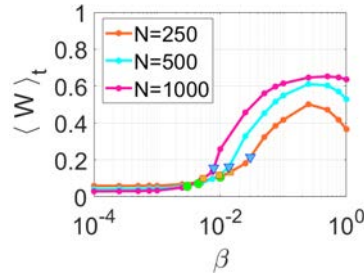


Figure 3.6: Time averaged polarization versus β for N marked in the inset, and $\eta = 0.5$. Circles correspond to the critical confinement $\beta_c(N; \eta)$, squares correspond to the inflection point of the susceptibility $\beta_i(N; \eta)$.

Figures 3.5(e) and 3.5(f) show that the LLE versus β curve reaches a local maximum at β_i . Thus, maximum ‘chaoticity’ is reached at the line of susceptibility inflection points. This qualitative feature of the line of inflection points is one of the reasons we have decided to use them to characterize the transition at finite N , at the same level as the line of local maxima usually selected in the statistical physics literature. The line of maxima of the LLE is also related to the location of the phase transition in the mean field Kuramoto model (Miritello et al. 2009). Fig. 3.6 shows the average polarization as a function of $\ln \beta$ for $N = 250, 500, 1000$. As N increases, $\beta_c, \beta_i, \beta_m$ simultaneously decrease to zero and so do the corresponding polarization order parameters, which suggest that these lines represent a second order phase transition at $N = \infty$.

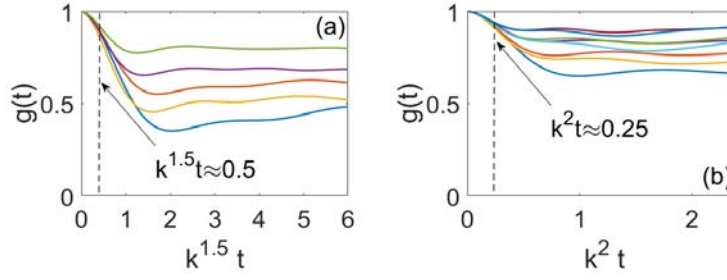


Figure 3.7: Collapse of NDCCF data as function of (a) $k^{1.5}t$ at the inflection point and of (b) k^2t at the local maximum of the susceptibility on the indicated narrow interval near $t = 0$. Here $\eta = 0.5$.

Figs. 3.7 (a) and 3.7(b) show NDCCF collapse of the NDCCF at $\beta_i(N; \eta)$ and $\beta_m(N; \eta)$, respectively. The respective dynamical critical exponents are $z_i = 1.5$ on $0 < k^z t < 0.5$ and $z_m = 2$ on $0 < k^z t < 0.25$. These exponents have been visually fitted because the correlation times obtained using Eq. (3.4) were unable to collapse data, unlike what happened for the transition from single cluster to muticluster chaos at β_c . Furthermore, the minima of $g(t)$ are all larger than 0.3, hence they are no longer close to zero as in Fig. 3.1. The different dynamical critical exponents at the different critical lines could be associated to different length scales in the multifractal chaotic dynamics at the three critical lines. The connection between dynamics and susceptibility in nonequilibrium phase transitions needs further study.

3.3 Subtracting rotation and dilation from CM velocity and flocking black hole phase transition

The confined VM is said to experience an ordering transition at high values of noise. In Refs. (Attanasi, Cavagna, L. D. Castello, et al. 2014; Cavagna, Conti, et al. 2017), the noise value chosen for numerical simulations is $\eta = 0.45 \times 4\pi = 5.65$ in our units. This value is well inside the noise region of Fig. 2.3(a). We can expect some remnants of coherent structures exhibiting rotation and dilation there. In equilibrium phase transitions, the order parameter is independent of time and space, and it is defined using ensemble averages. To mimic these transitions, in our definitions of DCCF and SCCF for large noise, it is convenient to subtract overall rotation and dilation from the CM velocity at each time step when defining fluctuations of the velocity, as explained in Appendix 3.A; see also Refs. (Attanasi, Cavagna, L. Del Castello, et al. 2014; Attanasi, Cavagna, L. D. Castello, et al. 2014). What is the effect of these operations?

Below the critical line $\beta_c(N; \eta)$ but close to it, the swarm occupies a single cluster and it is disperse. Fig. 3.8(a) shows that $\beta_c(N; \eta)$ and $\beta_i(N; \eta)$ do not change upon subtracting rotation and dilation from the CM velocity. However, the points on $\beta_m(N; \eta)$ are not local

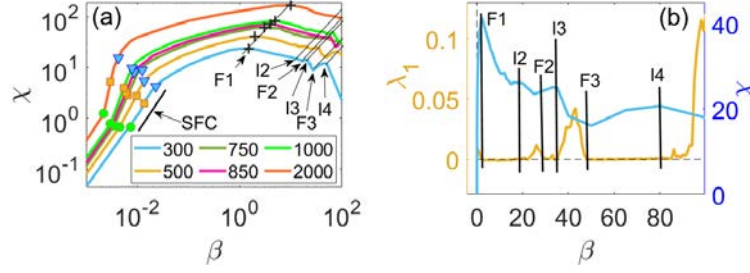


Figure 3.8: Real-space susceptibility (log-log scale) versus β for $N = 300, 500, 750, 850, 1000, 2000$. Circles and squares mark $\beta_c(N; \eta)$ and $\beta_i(N; \eta)$, which are the same with or without subtraction of rotation and dilation from CM motion. Triangles are the local maxima of susceptibility, β_m , without subtractions. Lines I_i, F_i ($i = 1, \dots, 4$) mark the initial and final β value of the i th chaotic window. Crosses mark β_M (global χ maximum of the susceptibility), which coincides with the line $F1$. **(b)** LLE and susceptibility versus β for $N = 500$. Note the different chaotic windows and the lines I_i, F_i .

maxima of χ vs β in Fig. 3.8(a). The line of global maxima of susceptibility versus β moves to the end of the first chaotic window of Fig. 3.5(b). The different chaotic windows for $N = 500$ are shown in Fig. 3.8(b). When the swarm splits into several clusters, they rotate and move with respect to each other. These effects are small at $\beta = \beta_i(N; \eta)$ (where the LLE reaches a local maximum) but the local maxima of the susceptibility versus β disappear. Thus, the lines $\beta_c(N; \eta)$ and $\beta_i(N; \eta)$ move to $\beta = 0$ as $N \rightarrow \infty$ at the same rate, thereby providing a finite size approximation of the scale-free-chaos phase transition. Using $\beta = \beta_c(N; \eta)$, the critical exponents $\nu = 0.43 \pm 0.01$ and $z = 1.00 \pm 0.03$ do not change when rotation and dilation are subtracted from CM motion in velocity fluctuations. We now have $\gamma = 0.85 \pm 0.04$. See Appendix 3.A. What about the line $\beta_M(N; \eta)$ of global maxima?

The correlation length is finite at $\beta_M(N; \eta)$, $\xi \approx 2.5$ for $\eta = 0.5$ and N values up to 2000. We have checked that the end of the first chaotic window (at which the LLE becomes zero again) and the β values of all successive chaotic windows increase with N . What happens? At the end of the chaotic window the clusters in the chaotic swarms are confined to regions of size $\xi \approx 2.5$ or smaller (recall that large β values confine all particles to a sphere of diameter 2 with period 2 motion in the deterministic case, $\eta = 0$). As N , and therefore $\beta_M(N; \eta)$, increase, more and more particles enter these regions, which implies that the average minimal distance between neighbors, x , decreases to zero as $N \rightarrow \infty$. Thus, confinement becomes infinitely strong, the average distance between neighbors tends to zero, and the particle density inside clusters becomes infinite. We call these clusters flocking black holes. Qualitatively, this situation resembles gravitational collapse of self-gravitating particles (Alberti et al. 2020; Chavanis et al. 2020). In particular, type II gravitational collapse to a zero mass black hole is analogous to second-order phase transitions with $x \rightarrow 0$ instead of $\xi \rightarrow \infty$ (Gundlach et al. 2007). By using $1/x$ instead of ξ , we can define critical exponents analogous to ν and γ for this flocking black hole phase

transition:

$$x \sim \beta^{-\nu}, \quad \chi \sim \beta^\gamma, \quad \tau_{k_c} \sim x^{-z}, \quad (3.13)$$

with $\beta = \beta_M(N; \eta) \rightarrow \infty$ as $N \rightarrow \infty$. Subtracting rotation and dilation from CM motion, we find the critical exponents, $\nu = 0.35 \pm 0.08$, $\gamma = 0.97 \pm 0.08$. Using fluctuations about the CM velocity without subtractions, $\beta_M(N; \eta)$ is larger and we can define similar critical exponents with it. We find $\nu = 0.33 \pm 0.02$, $\gamma = 1.03 \pm 0.03$. In both cases, the finite correlation length takes on the value 2.5, and the dynamical critical exponent is $z = 0$. The NDCCF decays at short times and it later oscillates. All curves for different N exhibit the same initial decay but the successive oscillations are irregular and displaced from one another.

3.3.1 Critical exponents from confined VM simulations

We have found a line of phase transitions $\beta_c(N; \eta)$ representing the change from scale-free single to multicluster chaos. See Chapter 2. The critical line is inside the confinement region where the NDCCF is flat at the origin, which corresponds to underdamped relaxation dynamics. For $\eta = 0.5$ (middle of the noisy chaos region), as $\beta = \beta_c(N; \eta) \rightarrow 0$, $N \rightarrow \infty$, we have obtained $\nu = 0.436 \pm 0.009$ (correlation length), $\gamma = 0.92 \pm 0.05$ (real-space susceptibility), and $z = 1.01 \pm 0.01$ (dynamic exponent). The critical exponent for the LLE law is approximately $\varphi = z\nu$. The critical exponents change little for $0.1 < \eta < 1$. Other critical lines based on the inflection points or local maxima of susceptibility versus β collapse to $\beta = 0$ at the same rate as $N \rightarrow \infty$ and therefore represent the same phase transition; cf Fig. 3.5(d).

While $\beta_c(N; \eta)$ and $\beta_i(N; \eta)$ do not change after subtracting rotation and dilation from the CM velocity, the values of the correlation length and time change, while still growing with N . For the critical line $\beta_c(N; \eta)$, we have found the critical exponents $\nu = 0.43 \pm 0.01$, $\gamma = 0.85 \pm 0.04$ and $z = 1.00 \pm 0.03$, which change but little with respect to the previous values.

The line of maxima of the susceptibility versus confinement curve, $\beta_M(N; \eta)$, is near the end of the first chaotic window and the LLE are small there. $\beta_M(N; \eta)$ goes to infinity with N and the correlation length goes to a finite constant. This phase transition at infinite confinement strength produces a collapse of particles inside bounded and infinitely dense clusters with vanishing LLE and critical exponents given by Eq. (3.13). For this flocking black hole phase transition, we have found $\nu = 0.35 \pm 0.08$, $\gamma = 0.97 \pm 0.08$ for $\eta = 0.5$ and N values up to 2000.

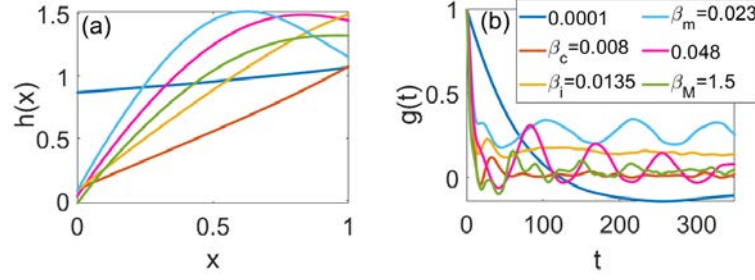


Figure 3.9: **(a)** Flatness function $h(x)$ and **(b)** NDCCF $g(t)$ for $N = 300$, $\eta = 0.5$ and β values indicated in Panel (b) inset.

3.3.2 Flatness function

A feature shared by swarm data and the scale-free-chaos phase transition is that the NDCCF is flat at small times. Fig. 3.9(a) depicts the flatness function $h(x)$ of Eq. (3.11) for a range of $\beta \in (0, \beta_M)$, where (after subtracting rotation and dilation) β_M is at the end of the first chaotic window of Fig. 3.5(b). For $0 < \beta \ll \beta_c(N; \eta)$, $h(x) \sim 1$ (as $x \rightarrow 0$), which implies exponential relaxation of the NDCCF with time, typical of overdamped dynamics. For these small values of β , noise overwhelms coherent dynamics induced by confinement and the LLE is negative. As β increases towards $\beta_c(N; \eta)$, $h(x)$ decreases until it is ≈ 0 for $x \rightarrow 0$. Then, VM dynamics is chaotic and underdamped. Fig. 3.9(a) shows the change in $h(x)$ for different values of β . See Fig. SF4 of (Cavagna, Conti, et al. 2017) for examples of overdamped and underdamped dynamics in the stochastic oscillator. Fig. 3.9(b) shows that the NDCCF exhibits oscillations for underdamped dynamics and a slower decay for overdamped noisy dynamics. The lines NDCCF oscillate at positive values of $g(t)$ for $\beta_i(N; \eta)$ and $\beta_m(N; \eta)$ (this later line corresponds to the local maximum without subtracting rotation and dilation from CM motion), whereas the oscillations have larger amplitude for larger values of β and $g(t)$ may take on negative values. Thus, the flatness function indicates that the confined VM displays underdamped dynamics in the critical region about $\beta_c(N; \eta)$ for the scale-free-chaos phase transition.

Inside the noise region of Fig. 2.3(a), the NDCCF decays exponentially at short times and it is non-flat according to the definition (3.11). This is the case for the noise value $\eta = 5.65$ (in our units) used in Refs. (Attanasi, Cavagna, L. D. Castello, et al. 2014; Attanasi, Cavagna, L. Del Castello, et al. 2014; Cavagna, Conti, et al. 2017). This exponential decay led to the hasty conclusion that the confined VM displays overdamped dynamics (Cavagna, Conti, et al. 2017), and to a subsequent search for convenient underdamped dynamics producing a flat NDCCF near $t = 0$ (Cavagna, Carlo, Giardina, Grigera, Melillo, et al. 2021). However, equations with discrete time dynamics, such as the harmonically confined VM, may exhibit overdamped and underdamped dynamics on different parameter ranges.

In experiments, the smallest measured value of $h(x)$ occurs at $x = 0.1$ and $h(0.1) < 0.3$ for natural swarms (Cavagna, Conti, et al. 2017). At the VM order-disorder phase transi-

tion, $h(0.1) \approx 1 > 0.3$ (exponential decay, clearly non-flat NDCCF) (Cavagna, Conti, et al. 2017). For the confined VM, the transition value occurs at $\eta = 0.9$ in Fig. 3.4(d) and in Fig. 2.3(a), which is close to the change to noise from noisy chaos at $\eta = 1$ (much lower than the noise for the order-disorder phase transition of the VM in a box with periodic boundary conditions (Attanasi, Cavagna, L. Del Castello, et al. 2014; Attanasi, Cavagna, L. D. Castello, et al. 2014; Cavagna, Conti, et al. 2017)). As noise increases, Fig. 3.4(d) shows that the correlation length decreases and $h(0.1)$ increases with increasing η . Thus, observed correlation lengths and flat NDCCFs occur in the region of noisy chaos of the confined VM that contains the scale-free-chaos phase transitions.

3.4 Discussion

Purpose. Here we discuss a hitherto unsuspected and unexplored phase transition of free scale chaos in the harmonically confined 3D Vicsek model. The same model exhibits a different phase transition to clusters of finite size containing infinitely many particles. This work is motivated by observations of natural midge swarms, which comprise at most hundreds of insects and form about a marker (Attanasi, Cavagna, L. D. Castello, et al. 2014; Attanasi, Cavagna, L. Del Castello, et al. 2014; Cavagna, Conti, et al. 2017; Kelley et al. 2013; Gorbonos et al. 2016; Sinhuber et al. 2017). The validation of the scale-free-chaos scenario by experimental data is outside the scope of this thesis.

Experiments and methodology. Cavagna *et al.*'s observations unveiled finite size scaling and power laws in swarms of male midges. They adapted definitions from statistical physics to define correlation functions, correlation lengths and calculate critical exponents from data (Attanasi, Cavagna, L. D. Castello, et al. 2014; Attanasi, Cavagna, L. Del Castello, et al. 2014; Cavagna, Conti, et al. 2017). To interpret data, they used the 'gas' phase of the 3D VM confined in a finite box with periodic boundary conditions and ideas about universality. Contrastingly, midge swarms in an enclosure form a 'condensed' nucleus far from enclosure walls surrounded by a 'vapor' of insects that exit from, return to, and hover about the nucleus (Sinhuber et al. 2017); see Fig. 2.4(b) for a similar configuration of the scale-free-chaos phase in our simulations. While this is different from an gas filling a box with uniform density, definitions from correlation functions, finite size and dynamical scaling apply to both numerical simulations of the model and experimental data (Attanasi, Cavagna, L. D. Castello, et al. 2014; Attanasi, Cavagna, L. Del Castello, et al. 2014; Cavagna, Conti, et al. 2017). We apply the methodology based on correlation functions to our simulations of the confined VM to unveil the scale-free-chaos phase transition.

Dynamical systems tools. As the confinement strength decreases, the VM with fixed number of particles N displays a variety of periodic, quasiperiodic and chaotic attractors, which may be strongly modified by alignment noise. To distinguish chaos, we have calculated the largest Lyapunov exponent directly from the VM using the Benettin algorithm

(Benettin et al. 1980). This is particularly well adapted to the discrete time dynamics of the VM. We have also calculated the LLE by reconstructing the attractor from time traces of the center of mass motion using lagged coordinates. Using only two lagged coordinates, scale-dependent Lyapunov exponents help distinguishing deterministic and noisy chaos from parameter regions where noise is dominant (Gao, Hu, et al. 2006). This is important because the phase transitions exist within the noisy chaos region. While scale-dependent Lyapunov exponents give qualitative information, we need six lagged coordinates to faithfully reconstruct the chaotic attractor and obtain (by the Gao-Zheng algorithm (Gao and Zheng 1994)) the same LLEs as provided by the Benettin algorithm. This methodology will be important to ascertain whether a real system in nature exhibits scale-free-chaos phase transitions.

Statistical physics tools. It is instructive to compare the scale-free-chaos phase transitions in the confined VM to the canonical para-ferromagnetic equilibrium phase transition whose universality class comprises the Ising and ϕ^4 models. A phase is an ergodic measure that exists in the thermodynamic limit (infinite volume and number of particles, finite density) and a phase transition corresponds to a discontinuous change from one to more than one phase as a parameter changes, i.e., to a bifurcation of the measure; see precise definitions and proofs in (Glimm et al. 1987). Pure phases have different values of the magnetization order parameter. At the critical point that ends a line of first order phase transitions at zero external field, the correlation length becomes infinity in the thermodynamic limit (Glimm et al. 1987). The magnetization order parameter undergoes a pitchfork bifurcation at the critical temperature with critical exponent 0.327 instead of 0.5 (Amit et al. 2005; Yeomans 1992).

The main objects to characterize critical points of second-order equilibrium phase transitions are static and dynamic correlation functions. To study flocking and other nonequilibrium phase transitions, we need to adapt the definitions of correlation functions, correlation length, susceptibility, and so on, to models such as Vicsek's. Averages over the number of particles, time averages and averages over realizations replace the ensemble averages of equilibrium statistical mechanics (Cavagna, Giardina, et al. 2018). Since it is important that correlation functions reflect underlying dynamic attractors, velocity fluctuations are about center of mass velocities (which may be chaotic); see (Cavagna, Giardina, et al. 2018) for extended discussion. Subtracting an overall rotation and/or dilation at each time step (Attanasi, Cavagna, L. Del Castello, et al. 2014; Attanasi, Cavagna, L. D. Castello, et al. 2014; Cavagna, Conti, et al. 2017) does not change the critical lines $\beta_c(N; \eta)$ and $\beta_i(N; \eta)$ but the local maxima of the susceptibility versus β curve disappear. We still have a critical line separating single from multicluster chaos followed by a narrow criticality region, both of which tend at the same rate to zero confinement as $N \rightarrow \infty$ and therefore represent the same phase transition; see Appendix 3.A.

The chaotic phases in scale-free-chaos transitions are ergodic (Ott 1993; Cencini et al. 2010). The transitions are second order: as $N \gg 1$, the order parameter is close to zero in the sparse single-cluster chaotic phase and the polarization is positive in the multicluster

chaotic phase. Let us discuss now the different critical lines at finite N that characterize the scale-free-chaos phase transition at $N = \infty$.

As discussed in Section 3.2, it would be ideal if we had a relation between the poles of the susceptibility and the reciprocal correlation time, as it happens in simple models. Then vanishing of the pole would be the same as the correlation time going to infinity (critical slowing down) and this would locate the critical point. In the absence of such a relation, we have first used the correlation time that solves Eq. (3.4) for $k_c = 1/\xi$ as a reasonable substitute. The critical line $\beta_c(N, \eta)$ is the value of β that minimizes τ_{k_c} for fixed N and noise η . Equivalently, it is the maximum value of the continuous extension of a correlation time defined as the first zero of the NDCCF. We have obtained a dynamic scaling exponent $z = 1.01 \pm 0.01$ and critical exponents $\nu = 0.436 \pm 0.009$, $\gamma = 0.92 \pm 0.05$, with $\varphi \approx z\nu$ (critical exponent corresponding to the decay of the largest Lyapunov exponent). For fixed N , $\beta_c(N, \eta)$ is a line on the plane (β, η) within the region of noisy chaos in Fig. 2.3(a). We have checked that the correlation length is proportional to the size of the swarm for all the simulated values of N , and therefore the system is scale free on this critical line. The critical line is inside an interval of confinement values for which the NDCCF is flat and relaxation dynamics is underdamped. Outside this interval, the confined VM exhibits overdamped dynamics. By using topological data analysis, we lend support to the numerical observation that chaos is single-cluster below this critical line and multicluster above it. The phase of single-cluster chaos has the smallest polarization order parameter and is therefore the most symmetric. Multicluster chaos has larger polar order. As $N \rightarrow \infty$, $\beta_c(N, \eta)$ tends to 0 and so does the LLE on that line: chaos disappears, as required by the correlation length becoming infinity and Eq. (3.2) for finite velocity of propagation. Further study involving the invariant measure of the chaotic attractors would be desirable to explore analogies with the phase ergodic measures of equilibrium thermodynamics.

Using the susceptibility of the real-space static correlation function and finite size scaling, we have found other lines $\beta_i(N; \eta)$ and $\beta_m(N; \eta)$, with $\beta_c < \beta_i < \beta_m$, that go to zero at the same rate as $\beta_c(N; \eta)$ for $N \gg 1$, cf Fig. 3.5(d). Thus, they represent the same phase transition and produce the same critical exponents as $N \rightarrow \infty$. For the N values in our simulations, we have checked that the correlation length is proportional to swarm size (therefore they are scale free) and ν is the same. The chaotic attractors are multicluster on the lines $\beta_i(N; \eta)$ and $\beta_m(N; \eta)$ based on the inflection point and the local maximum of the susceptibility, respectively; see Fig. 2.4. This indicates that the swarm center of mass experiences more important rotation and dilation effects than on the single-to-multicluster line $\beta_c(N; \eta)$.

The critical exponent z is different on the three critical lines, which may simply point to the multiple time and length scale involved in the multifractal chaotic attractors of the phase transition, cf Fig. 3.3. That different time scales are involved in the same transition is a common occurrence in codimension two bifurcations of dynamical systems (Kuznetsov 2004); see e.g., the scaled normal form in (Dangelmayr et al. 1987). The mean field version of the standard two-dimensional Vicsek model with periodic bound-

any conditions also involves two time scales near the order-disorder transition. The mean field VM (in a box with periodic boundary conditions) can be described by a discrete-time Enskog-type kinetic equation which preserves the overall number of particles (Ihle 2011). The order-disorder phase transition appears as a supercritical bifurcation of the kinetic equation when one multiplier crosses the unit circle in the complex plane; another multiplier corresponding to particle conservation is always one (Bonilla and Trenado 2018). On the ordered side, the scaled bifurcation equations contain two time scales, one with $z = 1$ (hyperbolic scaling), the other with $z = 2$ (parabolic scaling). At the hyperbolic short time scale, undamped wave propagation and resonance phenomena arise (Bonilla and Trenado 2018), whereas different band patterns appear at the parabolic time scale further from the bifurcation point (Trenado et al. 2022). These patterns exist on the ordered side of the ordering phase transition. They can be found in direct simulations of the standard Vicsek model and include bands (Solon et al. 2015) and crossbands (Kürsten et al. 2020).

In Section 3.3 and Appendix 3.A, we show that subtracting overall rotation and dilation from CM motion in velocity fluctuations does not change the lines $\beta_c(N; \eta)$ and $\beta_i(N; \eta)$ but the line of local maxima $\beta_m(N; \eta)$ disappears. The line of global maxima, $\beta_M(N; \eta)$, appears now at the end of the first chaotic window. On $\beta_M(N; \eta)$, the correlation length is finite and does not change appreciably with N , the average minimal distance between particles tends to zero and the density inside these clusters of finite extension tends to infinity. This transition has $\beta_M(N; \eta) \rightarrow \infty$ as $N \rightarrow \infty$ and therefore it is no longer scale free. Instead, it is analogous to type II gravitational collapse (Gundlach et al. 2007), and it has its own critical exponents, cf Eq. (3.13). In conclusion, subtracting rotation and dilation from CM motion leaves only two critical lines where the system is scale free, namely, $\beta_c(N; \eta)$ and $\beta_i(N; \eta)$. Only these two critical lines need to be taken into consideration when describing the phase transition based on subtracting overall translation, rotation and dilation from particle velocities to define velocity fluctuations. These two lines illustrate the existence of a narrow criticality region following $\beta_c(N; \eta)$ that also collapses to $\beta = 0$ as $N \rightarrow \infty$. Numerical simulations produce the same critical exponent ν as obtained without rotation and dilation but γ changes as explained in Appendix 3.A.

Critical exponents from experiments and theory. In observations of natural swarms, the measured critical exponents are $\nu = 0.35 \pm 0.10$, $\gamma = 0.9 \pm 0.2$ (Attanasi, Cavagna, L. Del Castello, et al. 2014; Attanasi, Cavagna, L. D. Castello, et al. 2014), and $z = 1.12 \pm 0.16$ (Cavagna, Conti, et al. 2017), while the real-space susceptibility is between 0.32 and 5.57 for the measured swarms (Attanasi, Cavagna, L. Del Castello, et al. 2014; Attanasi, Cavagna, L. D. Castello, et al. 2014). More recent observations give an interval $0.93 \leq z \leq 1.42$ of possible values of the dynamical exponent based on a resampling procedure; see Fig. 3 of (Cavagna, Carlo, Giardina, Grigera, Melillo, et al. 2021).

Here we have discussed the scale-free-chaos phase transition of the harmonically confined Vicsek model. For each adequate noise value within the interval of noisy chaos, cf Fig. 2.3(a), three critical lines coalesce at the same rate to $\beta = 0$ as $N \rightarrow \infty$. Thus, they

represent the same phase transition. For $\beta_c(N, 0.5)$, we have found $\nu = 0.436 \pm 0.009$ (correlation length), $\gamma = 0.92 \pm 0.05$ (real-space susceptibility), and $z = 1.01 \pm 0.01$ (dynamic exponent). The critical exponent for the LLE law is approximately $\varphi = z\nu$. These critical exponents change little for $0.1 < \eta < 1$ and are reasonably near experimentally measured ones.

Qualitative features. In addition to reasonable critical exponents, the scale-free-chaos phase transition produces disperse chaotic swarms below $\beta_c(N, \eta)$ that are confined to a bounded region of space with a few particles entering and leaving the nucleus of the swarm, cf. Fig. 2.4. This is akin to the observed condensed and vapor phases of natural swarms (Sinhuber et al. 2017). Furthermore, as shown in Section 3.2, the normalized dynamic correlation function coalesce to a single curve as a function of $k_c^z t$ for an interval $0 < k_c^z t < 4$ (cf. Fig. 3.1), which is similar to that observed in natural swarms; see Fig. 2b of (Cavagna, Conti, et al. 2017). Moreover, the flatness values given by Eq. (3.13) are compatible with those observed in natural swarms (Cavagna, Conti, et al. 2017). Observations of midges in the laboratory indicate that the center of mass of their swarm moves almost randomly (Kelley et al. 2013; Ni, Puckett, et al. 2015), following Lévy flights (Reynolds and Ouellette 2016). To this respect, the connection between chaos and Lévy flights in animal search patterns is intriguing (Reynolds, Bartomeus, et al. 2016) and could indicate that noisy chaos is indeed present in midge swarms. These similitudes to experimental observations and the involved theoretical challenges make worthwhile exploring more fully the confined Vicsek model and the phase transition we have discovered.

Critical exponents from models in the literature. The ordering transition of the VM confined in a finite box with periodic boundary conditions has received much attention; see e.g, the reviews in (Chaté and Mahault 2019; Chaté 2013). Near this transition, the particles form a gas and are distributed in the box with almost constant density (Chaté and Mahault 2019; Chaté 2013). This contrasts with observations of natural swarms in an enclosure where most of the swarm is far from walls (condensed phase) and individual insects hover around the swarm nucleus, enter and exit from it (Sinhuber et al. 2017). It is fair to say that the single-cluster chaotic phase of the confined VM resembles observations better than the ordering transition of the standard VM. Calculated critical exponents near the ordering transition of the VM in a box with periodic boundary conditions are also further away from observations: $\gamma = 1.6 \pm 0.1$, $\nu = 0.75 \pm 0.02$ (Attanasi, Cavagna, L. D. Castello, et al. 2014) for noise $\eta = 0.45 \times 4\pi = 5.65$ in our units), $z = 2$ (Cavagna, Conti, et al. 2017).

Many theoretical works study hydrodynamic equations with white noise forcing terms near a critical point which resembles that of the ordering transition of the standard VM. The idea is that all such descriptions could be analyzed using renormalization group (RG) theory and produce critical exponents compatible with experimental observations. This would then show that the appropriate hydrodynamic-type description belongs to the same universality class as the real natural swarms. These RG theories are based on weakly nonlinear expansions about a simple symmetric state. Chen *et al* study incompressible

Toner-Tu hydrodynamic equations (Toner and Tue 1995; Toner, Tu, et al. 2005) using RG about a unidirectional velocity and produce an exponent $z = 1.72$ in 3D (Chen, Toner, et al. 2015; Chen, Lee, et al. 2018). See also (Cavagna, Carlo, Giardina, Grigera, and Pisegna 2021) for numerical confirmation. Cavagna *et al* consider incompressible Toner-Tu hydrodynamics coupled to underdamped soft spin equations under white noise forces (Cavagna, Carlo, Giardina, Grigera, Melillo, et al. 2021). They study weakly nonlinear expansions about linear stochastic differential equations with constant coefficients and additive noise to obtain RG equations and calculate $z = 1.3$. These values are within the range of experimental observations (Cavagna, Carlo, Giardina, Grigera, Melillo, et al. 2021).

Recently, Holubec *et al* have studied the VM with time delay and periodic boundary conditions. They found $\gamma \approx 1.53$, $\nu \approx 0.75$ (larger than measured in midges) and $z \approx 1$ for very long delay times using an undersampled NDCCF (Holubec et al. 2021). Their NDCCF exhibits regular oscillations as the time delay increases, which are interpreted using a time-delayed reaction-diffusion equation; see Supplementary Information in (Holubec et al. 2021). It is not clear whether there is a single phase transition responsible for these results. In time-delayed ordinary differential equations, oscillations often appear as Hopf bifurcations at critical delays (Hale 1977) and may evolve to relaxation oscillations as delays increase (Bonilla and Liñán 1984). Delayed reaction-diffusion equations can have stable relaxation-type wavetrain solutions that depend on the variable $(x + ct)$, cf (Bonilla and Liñán 1984). This would give a dynamic exponent $z = 1$. Further study of the time-delayed VM may shed light on these connections.

A *universality class* comprises all physical systems that evolve to the same fixed point of the renormalization group equations under a rescaling of space and time and therefore have the same critical exponents (Huang 1987). We have discovered a scale-free-chaos phase transition in the discrete time Vicsek model confined by a harmonic potential, which has qualitative features of natural swarms, underdamped dynamics, and compatible critical exponents. At moderate N , this transition is different from the well-known period-doubling, intermittency and quasiperiodic routes to chaos (which have RGs based on maps (Schuster et al. 2005; Ott 1993; Cencini et al. 2010)) and from the ordering transition of the discrete time Vicsek model confined by a box with periodic boundary conditions (Chaté and Mahault 2019; Chaté 2013). The scale-free-chaos phase transition encompasses phenomena at different time scales, from dynamical exponent $z \approx 1$ to larger z for β_i and β_m , which might require additional theoretical tools to understand. While there are RG calculations about Hopf bifurcations to stable oscillatory states (Bonilla 1988; Risler et al. 2005), it would be desirable to have RG calculations about a single-cluster chaotic attractor, instead of the ordering transition of the standard VM (or related simple states of other models). Would it be possible to derive effective equations near the scale-free-chaos phase transition playing roles similar to amplitude equations in bifurcation theory (Bonilla 1988)? Could these effective equations exhibit new instabilities and coexistence of stable solutions and spinodal lines akin to those found in the Vicsek model with periodic

boundary conditions (Chaté and Mahault 2019; Chaté 2013)? Time will tell.

Summarizing, we have numerically simulated the harmonically confined Vicsek model, which is an idealized description of insect swarms. Depending on confinement strength β and noise η , the model exhibits different periodic, quasiperiodic and chaotic attractors. Our results support the existence of a line of phase transitions in a noisy chaos region of η values as the number of particles N tends to infinity and $\beta \rightarrow 0$. For finite N , there is a line $\beta_c(N; \eta)$ at which the correlation time is minimal and the correlation length is proportional to the system size. Topological data analysis supports the interpretation of $\beta_c(N; \eta)$ as a line separating single from multicluster chaos. The time averaged polarization acts as an order parameter: near $\beta_c(N; \eta)$, it is almost zero for $\beta < \beta_c(N; \eta)$ and positive and increasing with β for $\beta > \beta_c(N; \eta)$. On the line of scale free chaos, the dynamic critical exponent is $z \approx 1$ and the dynamic correlation function collapses on an interval of the same length as in measured swarms. Close to the critical line $\beta_c(N; \eta)$ and for fixed N and η , there are other critical lines obtained from the inflection point and local maximum of the susceptibility versus confinement curve. As $N \rightarrow \infty$, $\beta_c(N; \eta) \approx 0.48\beta_i(N; \eta)$ and $\beta_c(N; \eta) \approx 0.37\beta_m(N; \eta)$. Thus, the three lines represent a narrow criticality region, collapse at the same rate to $\beta = 0$ as $N \rightarrow \infty$ and stand for the same phase transition. Different exponent z on the lines may reflect the multiplicity of time and length scales involved in the chaotic attractors. The particle swarms at the scale-free-chaos phase transition share qualitative features and similar critical exponents of insect swarms. Our simulations also point to a different phase transition reminiscent of gravitational collapse to clusters of finite size containing infinitely many particles.

This work paves the way to studies in many directions. Possible directions consist of exploring other possible transitions on chaotic and non-chaotic windows of the parameter space and the effect of anisotropic confinement on the phase transition studied here. Exploring a possible phase transition to flocking black holes in self-gravitating models of swarms (Gorbonos et al. 2016) might be worth pursuing. On the theoretical side, can we find the invariant measure of the chaotic attractors and characterize scale-free-chaos phase transitions as $N \rightarrow \infty$ in terms of the invariant measure? This could bring together dynamical systems and nonequilibrium statistical mechanics studies and yield fruitful new ideas and methods.

3.5 Summary

We have found two phase transitions within the 3D Vicsek Model confined by a harmonic potential. One of them can yield information on swarms of midges (Scale free chaos) and the other with respect to gravitational collapse (Flocking black hole).

Scale free chaos phase transition:

In this chapter we have found three critical lines within the noisy chaos and near transition from a single chaotic cluster to a chaotic multi-cluster. One critical line refers to the minimum of the correlation (relaxation) time, β_c , another line to the inflection point of the susceptibility versus the control parameter β (maximum chaos), β_i , and a local maximum of the susceptibility versus β , β_m . These three critical lines tend to zero with the same exponents (they decay at the same rate) when $N \rightarrow \infty$. We can therefore calculate the power laws and their respective static critical exponents with any critical line for a sufficiently large value of N . Calculated with respect to the β_c we obtain $\nu = 0.436 \pm 0.009$, $\gamma = 0.92 \pm 0.05$ and $b = 0.58 \pm 0.01$ for the correlation length, susceptibility and the time-averaged order parameter, respectively. Entering into the critical exponents calculated in the midges swarms with their errors: $\nu = 0.35 \pm 0.10$ and $\gamma = 0.9 \pm 0.2$ (Attanasi, Cavagna, L. D. Castello, et al. 2014).

Another important point is the corresponding dynamic correlation function. From there we can obtain the dynamic critical exponent z with β_c , $z = 1.01 \pm 0.01$ with $\beta_i \approx 1.5$ and z with $\beta_m \approx 2$, by means of the collapse of the dynamic correlation function, or the power law $\tau_k \sim k_c^{-z}$ for β_c . Observing that the collapse only takes place at initial times, that the critical exponents are different at different critical lines and that the chaotic attractor has multifractal dimension, we conclude that there are different temporal and spatial scales within the chaotic attractor both theoretically and experimentally. The collapse of the correlation function β_c is identical to that of swarms of midges and the critical exponent $z = 1.12 \pm 0.16$ (Cavagna, Conti, et al. 2017) falls within the value of the exponent with β_c . Another important quality of this phase transition is the flatness at the origin $t = 0$, which is an important property of swarms of midges.

By dealing with a transition from chaos to chaos, we can obtain a new power law with respect to the Largest Lyapunov Exponent: $\lambda_1 \sim \beta^\varphi$. In this way we check that in the thermodynamic limit the critical point is $\lambda_1 \rightarrow 0$. The critical exponent $\varphi = 0.43 \pm 0.03$, conjecturing that $\varphi = z\nu$. This critical exponent needs to be calculated experimentally.

Finally, it has been observed that the results are the same even if the correlation functions are calculated by extracting the dilation and rotation modes as without extracting them.

Flocking black hole phase transition:

This phase transition belongs to the global maximum of the susceptibility versus the control parameter β . In this case flocks of subgroups are found moving around the origin (0,0,0). The correlation length remains constant with respect to the increase in N . That means that the subgroups of correlated particles do not grow in size, and therefore the density of these clusters grows to infinity as $N \rightarrow \infty$. In this way we can capture some critical exponents $\nu = 0.35 \pm 0.08$ and $\gamma = 0.97 \pm 0.08$, being the same ones that exist in

the literature on gravitational collapse.

Appendix 3.A Dynamic and static connected correlation functions

Definitions. Following Refs. (Attanasi, Cavagna, L. Del Castello, et al. 2014; Attanasi, Cavagna, L. D. Castello, et al. 2014), we define the dynamic connected correlation function (DCCF) as

$$\begin{aligned}
 C(r, t) &= \left\langle \frac{\sum_{i=1}^N \sum_{j=1, j \neq i}^N \delta \hat{\mathbf{v}}_i(t_0) \cdot \delta \hat{\mathbf{v}}_j(t_0 + t) \delta[r - r_{ij}(t_0, t)]}{\sum_{i=1}^N \sum_{j=1, j \neq i}^N \delta[r - r_{ij}(t_0, t)]} \right\rangle_{t_0} \quad (3.14) \\
 C(r) &= C(r, 0), \\
 \delta \hat{\mathbf{v}}_i &= \frac{\delta \mathbf{v}_i}{\sqrt{\frac{1}{N} \sum_k \delta \mathbf{v}_k \cdot \delta \mathbf{v}_k}}, \quad \delta \mathbf{v}_i = \mathbf{v}_i - \mathbf{V}, \\
 r_{ij}(t_0, t) &= |\mathbf{r}_i(t_0) - \mathbf{r}_j(t_0 + t)|, \quad \mathbf{r}_i(t_0) = \mathbf{x}_i(t_0) - \frac{1}{N} \sum_{j=1}^N \mathbf{x}_j(t), \\
 \langle f \rangle_{t_0} &= \frac{1}{t_{max} - t} \sum_{t_0=1}^{t_{max}-t} f(t_0, t).
 \end{aligned}$$

In these equations, $\delta(r - r_{ij}) = 1$ if $r < r_{ij} < r + dr$ and zero otherwise, and dr is the space binning factor. The usual dynamic correlation function and susceptibility in statistical mechanics are

$$C(r, t) = \langle (\phi(0, 0) - \langle \phi(0, 0) \rangle) (\phi(\mathbf{r}, t) - \langle \phi(\mathbf{r}, t) \rangle) \rangle, \quad (3.15a)$$

$$\chi = \int C(r, 0) d\mathbf{r} = \hat{C}(0, 0), \quad (3.15b)$$

respectively, where $\langle \dots \rangle$ are averages over the appropriate ensemble average and we have set $t_0 = 0$. In Appendix 3.B, we show two solvable examples indicating the relation between correlation time and susceptibility for different dynamics, which may or may not lead to thermal equilibrium.

In Eq. (3.14), we have replaced arithmetic means instead of the ensemble averages and added a time average. Dropping the condition $j \neq i$ adds one term proportional to $\delta(r)$ to numerator and denominator of Eq. (3.14), which is the choice made in Refs. (Cavagna, Conti, et al. 2017; Cavagna, Giardina, et al. 2018).

The function $C(r, t)$ sums all the products $\delta \mathbf{v}_i(t_0) \cdot \delta \mathbf{v}_j(t_0 + t)$ for those pairs i and j with a distance $r_{ij}(t_0, t)$ between r and $r + dr$, and then divides by the number of such pairs (denominator). It depends only on the distance r at time t because inter-particle interactions are local and distance dependent. The static connected correlation function (SCCF) is the equal time connected correlation function given by Eq. (3.14). As discussed in (Cavagna, Giardina, et al. 2018), these definitions are inspired in statistical mechanics

taking into account $\sum_j \delta \hat{\mathbf{v}}_j = 0$ because ensemble averages have been replaced by averages over the particles.

Susceptibility. For a SCCF that decays exponentially, the correlation length ξ is such that $C(\xi) = 1/e$. In the present work, there is finite size scaling (Attanasi, Cavagna, L. Del Castello, et al. 2014; Attanasi, Cavagna, L. D. Castello, et al. 2014; Cavagna, Conti, et al. 2017) and $C(r)$ or $C(r, t)$ do not decay exponentially with r and can take on negative values. Then the correlation length ξ is the first zero of $C(r)$, corresponding to the first maximum of the cumulative correlation function (Attanasi, Cavagna, L. Del Castello, et al. 2014; Attanasi, Cavagna, L. D. Castello, et al. 2014):

$$Q(r) = \frac{1}{N} \sum_{i=1}^N \sum_{j \neq i}^N \delta \hat{\mathbf{v}}_i \cdot \delta \hat{\mathbf{v}}_j \theta(r - r_{ij}), \quad \chi = Q(\xi), \quad (3.16)$$

$$\xi = \operatorname{argmax} Q(r), \quad C(\xi) = 0 \text{ with } C(r) > 0, \quad r \in (0, \xi),$$

where $\theta(x)$ is the Heaviside unit step function. It turns out that this correlation length ξ is proportional to the swarm size ℓ , which is the hallmark of scale free behavior. At equilibrium, the susceptibility measures the response of the order parameter to changes in an external field linearly coupled to it, and equals the integral of the SCCF (3.15b) with $C(r) > 0$. A susceptibility thus defined would be $Q(\infty)$. However, by Eq. (3.16), $Q(\infty) = Q(\ell) = -1$ because $\theta(\ell - r_{ij}) = 1$ and $\sum_i \delta \hat{\mathbf{v}}_i = 0$. Thus, we cannot define susceptibility by Eq. (3.15b). Instead, we define susceptibility χ as the value of $Q(r)$ at its first maximum, as in Eq. (3.8), and Refs. (Attanasi, Cavagna, L. Del Castello, et al. 2014; Attanasi, Cavagna, L. D. Castello, et al. 2014). For values of N corresponding to insects in measured swarms, our numerical simulations produce susceptibility values defined by Eq. (3.16) between 0.7 and 1.2, which are included in the measured interval (0.32, 5.57) (Attanasi, Cavagna, L. Del Castello, et al. 2014; Attanasi, Cavagna, L. D. Castello, et al. 2014).

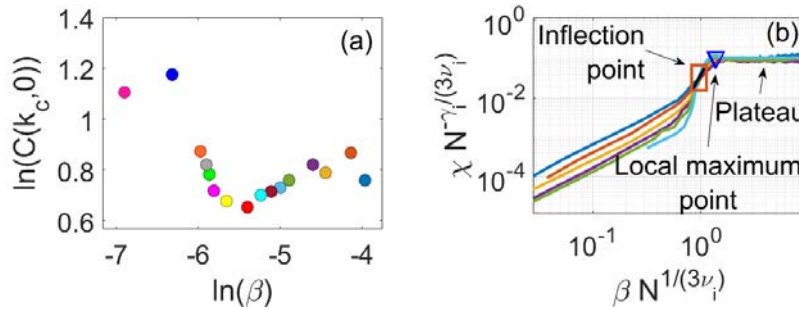


Figure 3.10: **(a)** Log-log scale plot of the susceptibility as given by $\max_k \hat{C}(k, 0)$ of Eq. (3.1) versus β_c . **(b)** Scaled susceptibility versus scaled confinement showing data collapse at the inflection point (square) and the local maximum (triangle) of the susceptibility. The local maximum is followed by a plateau of the scaled confinement. Here $\eta = 0.5$, $\nu_i = 0.44$, $\gamma_i = 1.2$.

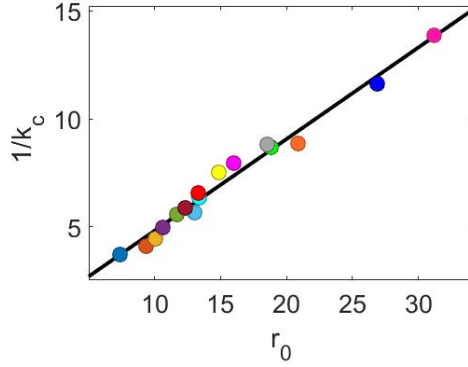


Figure 3.11: The correlation length $\xi = 1/k_c$ computed from the static correlation function in Fourier space as a function of the correlation length $\xi = r_0$ computed from the static correlation function in real space.

At equilibrium and for $N = \infty$, the susceptibility becomes infinity at critical points and it marks a phase transition. The susceptibility scales as

$$\chi(x) \sim (x - x_c)^{-\gamma}, \quad (3.17)$$

where x is the control parameter and x_c the value thereof for $N = \infty$. In our case, $x = \beta_c(N, \eta)$ and $x_c = \beta_c(\infty, \eta) = 0$, which produces $\gamma = 0.92 \pm 0.05$ as shown in Fig. 3.4(b). Eq. (3.1) is related to the Fourier transform of $C(r, t)$, as discussed in (Cavagna, Giardina, et al. 2018). Fig. 3.10(a) shows that $\hat{C}(k, 0)$ of Eq. (3.1) oscillates with $\beta_c(N; \eta)$. Thus, $\max_k \hat{C}(k, 0)$ is not a convenient definition of susceptibility. Contrastingly, Fig. 3.4(b) plots the real-space susceptibility $\max_r Q(r)$ using many more values, $500 \leq N \leq 5000$, which makes this fitting more reliable. Fig. 3.10(b) shows data collapse of scaled susceptibility and scaled confinement at β_i (susceptibility inflection point) and β_m (susceptibility local maximum). For our data, the relation between the correlation length as defined by Eq. (3.16) and $1/k_c$, given by $k_c = \arg\max_k \hat{C}(k, 0)$ is

$$\frac{1}{k_c} = 0.44 r_0 + 0.36; \quad (3.18)$$

see Fig. 3.11. Since our unit of length is 4.68 cm, the straight line in Fig. 3.11 is quite close to that of Fig. SF1 of (Cavagna, Conti, et al. 2017) (Supplementary data) obtained from measurements in natural midge swarms.

The global maximum of the susceptibility gives multicluster behavior as in Fig. 3.12(a). For larger values of β , some particles start being confined in a sphere centered at the origin and their number increases with β , as shown in Figs. 3.12(b-c).

Perception range. Instead of setting $x = \beta$, we can use the rescaled average nearest neighbor distance $x = r_1/R_0$ (perception range, inversely proportional to density), as in (Attanasi, Cavagna, L. Del Castello, et al. 2014; Attanasi, Cavagna, L. D. Castello, et al.

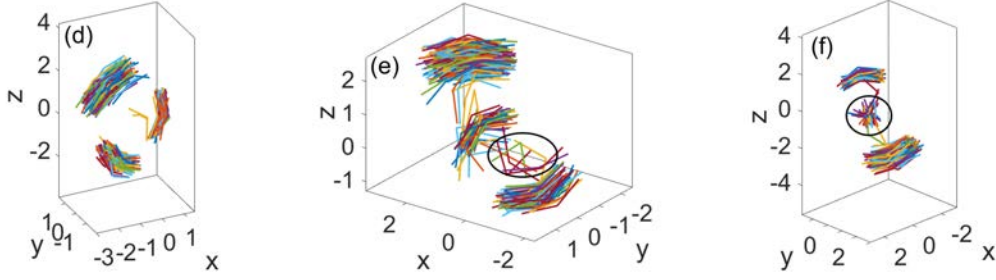


Figure 3.12: Chaotic swarms of $N = 300$ particles showing short trajectories of the particles for confinements and $\eta = 0.5$: **(a)** $\beta = \arg\max \chi(\beta) = 19.8$ (global maximum without subtracting rotation and dilation from CM motion). **(b)** For $\beta = 21$, three chaotic clusters move around a central sphere (located by a black circle) where other particles are confined; and **(c)** for $\beta = 25$, only two chaotic clusters remain and more particles are trapped in the central sphere.

2014). The perception range is calculated as the time average of the arithmetic mean of the minimal distance between each particle and its closest neighbor. We find a critical perception range $x_c = 2.945 \pm 0.047$, with $(x - x_c)$ proportional to β . This is larger than $x_c = 0.421 \pm 0.002$ at the order-disorder transition of the standard VM (Attanasi, Cavagna, L. Del Castello, et al. 2014; Attanasi, Cavagna, L. D. Castello, et al. 2014), indicating a less dense swarm at critical confinement. As $x_c = 12.5 \pm 0.1$ in natural swarms (measured in units of the average insect size) (Attanasi, Cavagna, L. Del Castello, et al. 2014; Attanasi, Cavagna, L. D. Castello, et al. 2014), the critical perception range is 4.2 insect bodies for the scale-free chaotic transition of the confined Vicsek model versus 30 insect sizes at the ordering transition of the VM with periodic boundary conditions. At the phase transition to clusters of finite size containing infinitely many particles, $x \rightarrow 0$ as $x \sim \beta^{-\nu}$ and $\chi \sim \beta^\gamma$, with $\beta_M \rightarrow \infty$ for $N \rightarrow \infty$. The critical exponents for this transition are $\nu = 0.33$ and $\gamma = 1.03$.

As chaos disappears when $\beta \rightarrow 0$, it may seem surprising that an ordered chaotic phase is less dense than the disordered phase at the larger noise of the order-disorder transition for the standard VM with periodic boundary conditions. Recall that density is inversely proportional to the average nearest neighbor distance (perception range). However, the confined VM does not morph seamlessly to the standard VM as $\beta_c(N; \eta) \rightarrow 0$. Firstly, confinement by a harmonic potential and confinement due to a large box with periodic boundary conditions are qualitatively different and they may not produce the same swarm patterns in the thermodynamic limit. Secondly, the standard VM with periodic boundary conditions experiences a crossover to a discontinuous order-disorder phase transition for $N \gg 1$ (Grégoire et al. 2004; Chaté and Mahault 2019; Chaté 2013). Thirdly, the noise values ($\eta = 5.65$ in our units) for which the confined VM and the standard VM with periodic boundary conditions have similar critical behaviors according to (Attanasi, Cavagna, L. D. Castello, et al. 2014; Attanasi, Cavagna, L. Del Castello, et al. 2014; Cavagna, Conti, et al. 2017) are much larger than the noisy chaos interval of Fig. 2.3(a). Thus, we

think that the scale-free-chaos phase transition of the confined VM as $\beta \rightarrow 0$ is not related to the continuous ordering transition of the standard VM.

Numerical calculation of the connected correlation functions. Fixing the parameters N , η and β , we simulate the VM for five different random initial conditions during 10000 iterations. After a sufficiently long transient period, the polarization of Eq. (2.4) fluctuates about a constant value. Once this regime is established, we use the last 2000 iterations to calculate the static correlation function $\hat{C}(k, 0)$, whose first maximum provides the critical wave number k_c . Using the definition in Eq. (3.1) and averaging over the five realizations, we obtain the time dependent correlation function.

Rotation and dilation. In Refs. (Attanasi, Cavagna, L. D. Castello, et al. 2014; Attanasi, Cavagna, L. Del Castello, et al. 2014), the average swarm velocity is defined subtracting overall rotations and dilations from \mathbf{V} at each time step. Note that an overall rotation does not change the distance between trajectories (which are used to calculate Lyapunov exponents) but an overall dilation does. To subtract an overall rotation, we proceed as follows. The fluctuations of the velocity are

$$\delta \mathbf{v}_i(t+1) = \mathbf{y}_i(t+1) - \mathbf{y}_i(t), \quad (3.19a)$$

$$\mathbf{y}_i(t) = \mathbf{x}_i(t) - \mathbf{X}(t), \quad (3.19b)$$

$$\mathbf{X}(t) = \frac{1}{N} \sum_{j=1}^N \mathbf{x}_j(t), \quad (3.19c)$$

$$\mathbf{X}(t+1) - \mathbf{X}(t) = \mathbf{V}(t+1). \quad (3.19d)$$

We can define the optimal rotation matrix as the 3×3 orthogonal matrix \mathbf{U} that minimizes

$$\mathbf{U} = \operatorname{argmin}_{\mathbf{U}^T \mathbf{U} = \mathbf{I}} \left[\frac{1}{2} \sum_{i=1}^N [\mathbf{y}_i(t+1) - \mathbf{U} \mathbf{y}_i(t)]^2 \right]. \quad (3.20a)$$

The optimal dilation is

$$\Lambda = \operatorname{argmin}_{\Lambda} \left[\frac{1}{2} \sum_{i=1}^N [\mathbf{y}_i(t+1) - \Lambda \mathbf{U} \mathbf{y}_i(t)]^2 \right]. \quad (3.20b)$$

From (Kabsch 1976), the optimal rotation matrix for Eq. (3.20a) is

$$U_{ij} = \sum_{k=1}^N B_{ki} A_{kj}, \quad (3.21a)$$

$$B_{ki} = \sum_{n=1}^N \sum_{l=1}^3 Y_{ni}(t+1) Y_{nl}(t) \frac{A_{kl}}{\sqrt{\mu_k}}, \quad (3.21b)$$

where $Y_{ni}(t)$ is the $N \times 3$ matrix formed by the components of the vector $\mathbf{y}_n(t)$. The orthogonal matrix A_{kl} is formed by the orthogonalized eigenvectors of the eigenvalue problem

$$\sum_{lm=1}^N \sum_{n,p=1}^3 [Y_{li}(t) Y_{ln}(t+1) Y_{mp}(t) Y_{mn}(t+1)] A_{kp} = \mu_k A_{ki}, \quad (3.21c)$$

$$\mu_k \geq 0,$$

for the 3×3 positive semidefinite symmetric matrix within square brackets appearing in this expression. In the generic case, the three eigenvalues μ_k are positive. If one eigenvalue is zero, e.g., $\mu_3 = 0$, then Eq. (3.21b) yields only two vectors, B_{1i} , B_{2i} , corresponding to the eigenvectors with nonzero eigenvalues, A_{1i} , A_{2i} . The other eigenvector A_{3i} and B_{3i} are

$$A_{3i} = \sum_{j,k=1}^3 \epsilon_{ijk} A_{1j} A_{2k}, \quad B_{3i} = \sum_{j,k=1}^3 \epsilon_{ijk} B_{1j} B_{2k}, \quad (3.21d)$$

where ϵ_{ijk} is the completely antisymmetric unit tensor with $\epsilon_{123} = 1$ (Kabsch 1976). With these definitions of A_{3i} and B_{3i} , Eq. (3.21a) holds.

To subtract overall dilation, we use the optimal dilation matrix from Eq. (3.21b),

$$\Lambda = \frac{\sum_{j,k=1}^N \sum_{i,l=1}^N Y_{jl}(t+1) B_{ki} A_{kl} Y_{jl}(t)}{\sum_{j,k=1}^N \sum_{i,l=1}^N [B_{ki} A_{kl} Y_{jl}(t)]^2}. \quad (3.21e)$$

Then the fluctuations in Eq. (3.1) are (Attanasi, Cavagna, L. Del Castello, et al. 2014)

$$\delta \mathbf{v}_i(t_0) = \mathbf{y}_i(t_0 + 1) - \Lambda \mathbf{U} \mathbf{y}_i(t_0). \quad (3.22)$$

Note that $\sum_i \delta \mathbf{v}_i(t_0) = \sum_i \mathbf{y}_i(t_0 + 1) - \Lambda \mathbf{U} \sum_i \mathbf{y}_i(t_0) = 0$. Subtracting only overall rotations, we would use $\delta \mathbf{v}_i(t_0) = \mathbf{y}_i(t_0 + 1) - \mathbf{U} \mathbf{y}_i(t_0)$ instead of Eq. (3.22).

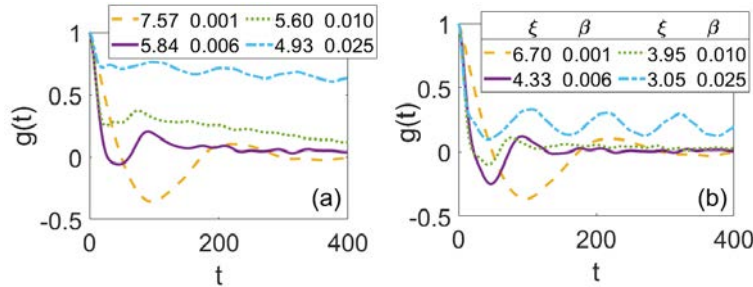


Figure 3.13: Normalized dynamic correlation function with $\xi = 1/k_c$ for different values of β calculated from (a) Eq. (3.1) and (b) from Eq. (3.1) subtracting rotation and dilation in the velocity fluctuations. Here, $N = 300$, $\eta = 0.5$.

Results. Figs. 3.13(a) and 3.13(b) compare the NDCCF $g(t)$ calculated as in Eq. (3.1) and the same function subtracting rotation and dilation. We observe that both functions look alike and that subtracting rotation and dilation changes slightly the times $t_m(\beta, N)$ where $g(t_m) = 0$. Then the critical line $\beta_c(N, \eta)$ is unchanged by subtractions of rotation and dilation; see also Fig. 3.14 for the collapse of the NDCCF with dynamical exponent z . The relation (3.18) becomes $k_c r_0 = 2$ after subtractions. We expect small rotation and dilation for single-cluster chaos and larger rotation and dilation for multicluster chaos.

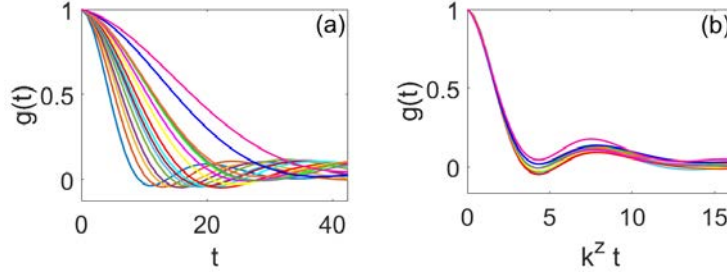


Figure 3.14: Same as Figure 3.1 but calculated subtracting rotation and dilation: NDCCF $g(t)$ versus (a) t and (b) $k^z t$ with $z = 1.00 \pm 0.03$.

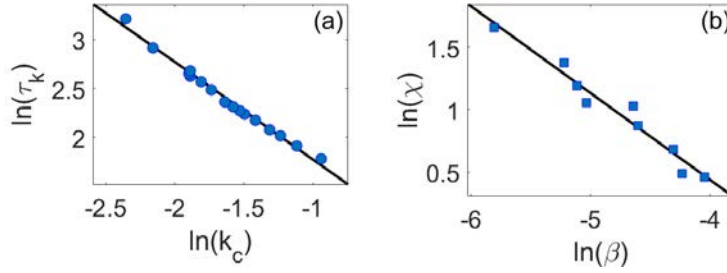


Figure 3.15: (a) Correlation time versus β at the critical line $\beta_c(N; 0.5)$. (b) Susceptibility versus β at the critical line $\beta_i(N; 0.5)$. Both power laws calculated subtracting rotation and dilation from CM motion.

Thus, subtracting rotation and dilation brings down $g(t)$. In in Fig. 3.13, this effect is largest for $\beta = 0.025$, well inside the region of multicluster chaos.

The critical lines $\beta_c(N; \eta)$ and $\beta_i(N; \eta)$ do not change by subtractions from CM motion but the local maxima defining the line $\beta_m(N; \eta)$ disappear. The critical exponent $\nu = 0.45 \pm 0.02$ rests unchanged by subtractions. However, for $N \leq 2000$, $\gamma_i = 0.70 \pm 0.06$ (on the line of inflection points of χ vs β) drops from the value 1.2 obtained without subtractions, cf Fig. 3.15(b). Together with the larger value of the polar order parameter, this confirms that the critical line $\beta_i(N; \eta)$ lies in the multicluster chaos region where rotation and dilation effects are more prominent; see Fig. 2.4(c) and Figs. 3.12 for pictures of swarms splitting into different clusters.

The global maxima $\beta_M(N; \eta)$ of the susceptibility vs confinement curve in Fig. 3.5(a) move to the end of the first chaotic window when subtracting rotation and dilation from CM motion and do not correspond to scale free transitions. Fig. 3.16(a) shows that the correlation length for these states does not change with the number of particles maxima and is no longer proportional to the swarm size. At the line $\beta_M(N; \eta)$, chaos is multicluster and rotation and dilation effects are stronger. As shown in Figs. 2.4 and 3.16(b), these chaotic clusters are not connected, and their correlation length remains unchanged with N : it takes on a value similar to the diameter of the sphere of influence (2.5 versus 2, in nondimensional units). In conclusion, using the critical lines $\beta_c(N; \eta)$ and $\beta_i(N; \eta)$ (for which rotation and dilation effects are very minor), and not $\beta_m(N; \eta)$, is crucial to unveil

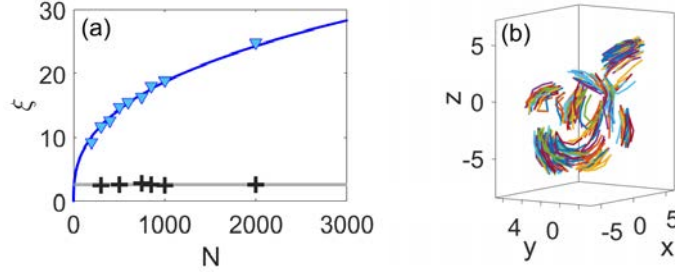


Figure 3.16: (a) Correlation length versus N obtained without (triangles) and with (crosses) subtraction of rotation and dilation from CM velocity at confinements corresponding to the susceptibility maximum. (b) Chaotic swarm showing short trajectories of 300 particles for $\beta_M(N; \eta)$: Subtractions shift the critical line to larger confinement well inside the multicluster chaos region. Here, $\eta = 0.5$.

the scale-free-chaos phase transition in the limit of infinitely many particles.

Appendix 3.B Susceptibility and correlation time

Here we illustrate the relations between reciprocal correlation time and singularities of the susceptibility by solvable examples. Note that these examples could be linearizations of stochastic equations about a time-independent homogeneous state. Thus, they are still far from the phase transition about a chaotic spatially non-homogeneous state and are not directly applicable to the confined VM.

I. Consider the diffusive and noisy overdamped oscillator

$$\frac{\partial \phi}{\partial t} = D \nabla^2 \phi - \omega_0^2 \phi + \sqrt{2T} \xi(x, t), \quad (3.23a)$$

where $\xi(x, t)$ is a zero mean delta correlated white noise. The equilibrium probability density corresponding to Eq. (3.23a) is $Z^{-1} e^{-\int H dx/T}$, with hamiltonian density $H = (D|\nabla \phi|^2 + \omega_0^2 \phi^2)/2$ and temperature T . The Fourier transformed solution and the Fourier transformed correlation function are

$$\hat{\phi}(k, t) = \int_{-\infty}^t e^{-(\omega_0^2 + Dk^2)(t-s)} \hat{\xi}(s, k) ds, \quad (3.23b)$$

$$\begin{aligned} \hat{C}(k, t) &= 2T \int_{-\infty}^{t_0} e^{-(\omega_0^2 + Dk^2)(t_0-s)} e^{-(\omega_0^2 + Dk^2)(t_0+t-s)} ds \\ &= \frac{T}{\omega_0^2 + Dk^2} e^{-(\omega_0^2 + Dk^2)t}. \end{aligned} \quad (3.23c)$$

Here we have taken the initial time to be $-\infty$ and a zero initial condition. Instability of the trivial state $\phi = 0$ is reached when $\omega_0^2 = 0$, $k \propto 1/L = 0$, which is pole of the susceptibility, $\hat{C}(0, 0) = T/\omega_0^2$, and, equivalently, infinite value of the maximal correlation time, $1/\omega_0^2$. The nonlinear version of Eq. (3.23a),

$$\frac{\partial \phi}{\partial t} = D \nabla^2 \phi - \omega_0^2 \phi - \zeta \phi^3 + \sqrt{2T} \xi(x, t), \quad (3.23d)$$

produces an equilibrium probability density corresponding to the Landau-Wilson hamiltonian density $H = (D|\nabla\phi|^2 + \omega_0^2\phi^2)/2 + \zeta\phi^4/4$, which has a paradigmatic second order phase transition provided ω_0^2 may become negative (Amit et al. 2005).

II. To ascertain the influence of dynamics, consider the underdamped version of Eq. (3.23a):

$$\frac{\partial^2\phi}{\partial t^2} + 2\omega_d \frac{\partial\phi}{\partial t} = D\nabla^2\phi - \omega_0^2\phi + \sqrt{4\omega_d T} \xi(x, t). \quad (3.24a)$$

Proceeding as before, we find

$$\hat{\phi}(k, t) = \int_{-\infty}^t G(t-s; k) \hat{\xi}(s, k) ds, \quad (3.24b)$$

$$G(t; k) = e^{-\omega_d t} \frac{\sin[\Omega(k)t]}{\Omega(k)} \theta(t), \quad (3.24c)$$

$$\Omega(k) = \sqrt{\omega_0^2 + Dk^2 - \omega_d^2}, \quad (3.24d)$$

$$\begin{aligned} \hat{C}(k, t) &= 4T\omega_d' \int_0^\infty G(s; k)G(t+s; k) ds \\ &= \frac{T\omega_d' e^{-\omega_d t}}{\omega_0^2 + Dk^2} \left(\frac{\cos[\Omega(k)t]}{\omega_d} + \frac{\sin[\Omega(k)t]}{\Omega(k)} \right), \end{aligned} \quad (3.24e)$$

$$\chi = \hat{C}(0, 0) = \frac{T\omega_d'}{(\omega_0^2 + Dk^2)\omega_d}. \quad (3.24f)$$

Here we assume $\Omega(k)^2 > 0$. For $\omega_d' = \omega_d$, the underdamped dynamics about thermal equilibrium yields the same susceptibility as Eq. (3.23c). The pole of the susceptibility is again $\omega_0(k)^2 = \omega_0^2 + Dk^2$. Allowing ω_0^2 to change sign and adding a nonlinearity as in Eq. (3.23d) leads to the same equilibrium phase transition as Eq. (3.23a). However, for $0 < \omega_d' \neq \omega_d$, $\omega_0^2 > 0$, and allowing ω_d to change sign, the system cannot reach thermal equilibrium as it did in the overdamped case. We have an additional pole of the susceptibility (3.24f), ω_d , which coincides with the reciprocal relaxation time of Eq. (3.24e). Adding a nonlinearity $-\zeta\phi^2\partial\phi/\partial t$ to the right hand side of Eq. (3.24a) may produce a quite different van der Pol-like instability and phase transition for $\omega_d < 0$. Certainly, the van der Pol limit cycle appears as a supercritical Hopf bifurcation (Kuznetsov 2004) and the corresponding nonequilibrium phase transition would be similar to that analyzed in (Risler et al. 2005) by RG calculations. For this nonequilibrium phase transition, vanishing of the reciprocal relaxation time coincides with vanishing of the pole $\omega_d = 0$.

Immersed boundary approach to biofilm spread on surfaces

4.1 Introduction

In this chapter, we propose a computational model of bacterial biofilms (see Section 1.2) that combines an immersed boundary (IB) description of cellular arrangements and mechanical interactions with a dynamic energy budget (DEB) representation of bacterial activity and chemical processes, including the action of toxicants. Modeling biofilm response to antibiotics is a crucial issue in their study (Høiby et al. 2010). The chapter is organized as follows. Section 4.2 introduces the submodels for the different mechanisms. Section 4.3 nondimensionalizes the equations. Computational issues are discussed in Section 4.4, while presenting numerical simulations for horizontal spread of spherical and rod-like bacteria. In configurations of spatial competition between spherical and rod-shaped bacteria, rod-shaped bacteria seem to dominate. Rod-like bacteria tend to align. We are able to study geometrical arrangements, formation of porous structures and interactions with inner flow processes. Section 4.5 considers spread of slices on barriers. While variations in the limiting concentration lead to finger formation, addition of toxicants results in shrinking aggregates. Finally, Section 4.6 shows how biofilm extinction can be achieved combining two types of antibiotics, one targeting active cells in the outer layers and another one targeting dormant cells in the biofilm core. Section 4.7 summarizes our conclusions.

4.2 Model

Taking the IB point of view (Peskin and McQueen 1995; Peskin 2002), we consider the biofilm as a collection of spherical or rod-like cells, represented by their boundaries, immersed in a viscous fluid and subject to forces representing interactions, which are influenced by cell activity as we describe next. We will formulate the model in 2D.

4.2.1 Immersed boundary representation

Let us first describe the basic geometrical arrangement. To fix ideas, we consider the schematic structure depicted in Figure 1.2, a region Ω containing fluid and bacteria. We characterize bacteria by immersed boundaries representing their membranes. We assume the immersed boundaries have zero mass and are permeated by fluid. This liquid containing dissolved substances is considered incompressible. To simplify, we assume that the properties of the liquid are uniform.

The governing equations are established in (Peskin and McQueen 1995; Peskin 2002). We summarize them here, including variations to adapt them to our biofilm framework:

- *Incompressible Navier-Stokes equations* in Ω with friction

$$\frac{\partial \mathbf{u}}{\partial t} + \mathbf{u} \cdot \nabla \mathbf{u} = \nu \Delta \mathbf{u} - \frac{1}{\rho} \nabla p + \frac{1}{\rho} \mathbf{f} - \frac{\alpha}{\rho} \mathbf{u}, \quad \text{div}(\mathbf{u}) = 0, \quad (4.1)$$

where $\mathbf{u}(\mathbf{x}, t)$ and $p(\mathbf{x}, t)$ are the fluid velocity and pressure, while ρ , $\nu = \frac{\mu}{\rho}$ and α stand for the fluid density, kinematic viscosity and friction coefficient, respectively. The source \mathbf{f} represents the force density, that is, force per unit volume.

- *Force spread.* The force $\mathbf{f}(\mathbf{x}, t)$ created by the immersed boundary (IB) on the fluid is given by

$$\mathbf{f}(\mathbf{x}, t) = \int_{\Gamma} \mathbf{F}(\mathbf{q}, t) \delta(\mathbf{x} - \mathbf{X}(\mathbf{q}, t)) d\mathbf{q}, \quad (4.2)$$

where $\mathbf{X}(\mathbf{q}, t)$ is the parametrization of an immersed boundary Γ , and $\mathbf{F}(\mathbf{q}, t)$ the force density on it. The integration parameters \mathbf{q} represent 3D angles.

- *Velocity interpolation.* The evolution equation for the IB

$$\frac{\partial \mathbf{X}}{\partial t} = \int_{\Omega} \mathbf{u}(\mathbf{x}, t) \delta(\mathbf{x} - \mathbf{X}(\mathbf{q}, t)) d\mathbf{x} + \lambda((\mathbf{F}_g \cdot \mathbf{n})\mathbf{n} + \mathbf{F}_{ext}), \quad (4.3)$$

is obtained correcting the no-slip condition with a term representing the contribution of the growth forces \mathbf{F}_g on the IB. \mathbf{n} stands for the unit outer vector. Notice that elastic forces within the IB do not contribute to this term because they are tangent to the normal $\mathbf{F}_e \cdot \mathbf{n} = 0$. \mathbf{F}_{ext} represents additional external forces that move bacteria as blocks, it includes at least interaction forces \mathbf{F}_i . The adjusting factor λ has units $\frac{s}{kg}$.

Fluid-structure interaction is mediated by delta functions δ . In practice, the δ function is replaced for computational purposes with approximations which scale with the mesh-width like $1/L^3$ in $3D$. Adequate regularizations are discussed in (Peskin and McQueen 1995; Peskin 2002). We locate the immersed boundaries far from the borders of the computational domain, and enforce periodic boundary conditions for the fluid on them.

The above equations differ from standard IB models in two respects. First, we include friction in Navier-Stokes equations (4.1) as a way to represent the presence of polymeric threads hindering bacterial displacement. We could include threads joining the cells as part of the immersed structures, but we have chosen to represent their influence through friction in the fluid and interaction forces between the bacteria, to be described later. Second, we consider that the forces on the immersed boundaries are more general than just the elastic forces within it. This results in the addition of the term $(\mathbf{F}_g \cdot \mathbf{n})\mathbf{n}$ in equation (4.3) for their dynamics and allows to connect the growth forces to a description of cell metabolism.

4.2.2 Forces

In our case, the IB \mathbf{X} is composed of many disjoint boundaries \mathbf{X}_j , $j = 1, \dots, N$, representing the membranes of individual bacteria. The total force density \mathbf{F} on the IB is the sum of several contributions.

- *Elastic forces \mathbf{F}_e .* In general, the elastic forces take the form $\mathbf{F}_e = -\frac{\partial E}{\partial \mathbf{X}}$, where $E(\mathbf{X})$ is an elastic energy functional defined on the immersed boundary configuration \mathbf{X} .

In a two dimensional setting, and assuming the boundary is formed by Hookean springs with zero rest length and parametrized by the angle θ , the force would be

$$\mathbf{F}_e = \frac{\partial}{\partial \theta} \left(K \frac{\partial \mathbf{X}}{\partial \theta} \right), \quad (4.4)$$

for an elastic parameter K (spring constants have units N/m). If we modify formula (4.2) to calculate a force per unit area \mathbf{f}

$$\mathbf{f}(\mathbf{x}, t) = \int_0^{2\pi} \mathbf{F}(\theta, t) \delta(\mathbf{x} - \mathbf{X}(\theta, t)) d\theta, \quad (4.5)$$

then δ should include units $1/L^2$. These forces are calculated on each component \mathbf{X}_j , $j = 1, \dots, N$.

- *Interaction forces \mathbf{F}_i .* Bacteria adopt typically spherical (*coccus*), rod-like (*Bacillus*, *Pseudomonas*) or spiral (*Vibrio*) shapes. We focus on the first two types here. Bacteria in a biofilm lose their cilia and flagella, that is, their ability to move on their own. On one hand, there are repulsive forces between membranes that prevent bacteria from colliding. On the other, polymeric threads keep bacteria together. As mentioned earlier, we might add a thread network. However, we choose to represent

their action by means of a friction term in Navier-Stokes equations. In this way, we avoid adding thread networks to keep cells together. We just need to separate the cells as they grow or divide.

When the distances between bacteria are below a critical distance, repulsion forces act fast. The repulsion force $\mathbf{F}_{i,j}$ acting on each bacterium with boundary \mathbf{X}_j , $j = 1, \dots, N$, depends on the distance between all pairs. For spherical bacteria, we set the force as follows:

$$\mathbf{F}_i = \sum_{j=1}^N \mathbf{F}_{i,j} \delta_j, \quad \mathbf{F}_{i,j} = \begin{cases} \sum_{n=1, n \neq j}^N \frac{\sigma}{d_{min}} \mathbf{n}_{cm,n,j} & \text{if } d_{j,n} \leq d_{min}, \\ \sum_{n=1, n \neq j}^N \frac{\sigma \left(1 + \tanh\left(\frac{s_p - d_{j,n}}{v_p}\right)\right)}{2d_{j,n}} \mathbf{n}_{cm,n,j} & \text{if } d_{j,n} > d_{min}, \end{cases} \quad (4.6)$$

where σ is the repulsion parameter with appropriate units, $d_{j,n}$ is the smallest distance between the curves defining bacteria j and n , N is the number of bacteria, and $\mathbf{n}_{cm,n,j} = \frac{\mathbf{X}_{c,j} - \mathbf{X}_{c,n}}{\|\mathbf{X}_{c,j} - \mathbf{X}_{c,n}\|}$ is the unit vector that joins the centers of mass, oriented from n to j . Here, δ_j takes the value 1 at the nodes of the cell boundary \mathbf{X}_j and vanishes on other cell boundaries. Additional parameters govern the minimum value d_{min} that $d_{j,n}$ can take, the order of magnitude of this force s_p , and the decay as the distance decreases v_p . These forces are similar for spheres and rods, changing the parameter values, see Table 4.3.

- *Growth forces \mathbf{F}_g .* Growth of spherical bacteria is described through variations in their radius, whereas rod-like bacteria grow in length. Assuming the rate of growth of their radius (resp. lengths) are known, the effect on each cell boundary would be, for spheres,

$$\frac{dR_j}{dt} \frac{\mathbf{X}_j - \mathbf{X}_{c,j}}{\|\mathbf{X}_j - \mathbf{X}_{c,j}\|} = \frac{dR_j}{dt} \mathbf{n}, \quad j = 1, \dots, N, \quad (4.7)$$

where R_j and $\mathbf{X}_{c,j}$ denote the radius and center of the bacterium \mathbf{X}_j . For rods, growth forces act on the edges, forcing a change of length

$$\frac{1}{2} \frac{dL_j}{dt} \mathbf{l}, \quad j = 1, \dots, N, \quad (4.8)$$

where \mathbf{l} is an outer unit vector along the rod axis. Notice that for spheres $(\frac{dR_j}{dt} \mathbf{n} \cdot \mathbf{n}) \mathbf{n} = \frac{dR_j}{dt} \mathbf{n}$ whereas for rods $(\frac{dL_j}{dt} \mathbf{l} \cdot \mathbf{n}) \mathbf{n} \sim 0$ except on the rod edges. We take \mathbf{F}_g proportional to these growth factors.

Our description of cell metabolism in Section 4.2.3 provides the required equations for the time dynamics of radii R_j and lengths L_j .

Finally, the total force we have to spread to the fluid through (4.2) or (4.5) is the sum of all the forces $\mathbf{F} = \mathbf{F}_e - \mathbf{F}_i + \mathbf{F}_g$.

4.2.3 Cellular activity

We describe bacterial metabolism by means of a dynamic energy budget approach (Birnie et al. 2018; Kooijman 2008; Klanjscek et al. 2012):

- *Dynamic energy budget equations for cell metabolism.* Bacteria transform nutrients and oxygen in energy, which they use for maintenance, growth and division. In a biofilm, some cells undergo phenotypical changes and start performing new tasks. For instance, some become producers of exopolysaccharides, that is, the extracellular polymeric substances forming the biofilm EPS matrix. This is more likely for cells with scarce resources (Høiby et al. 2010; Chai et al. 2011) to sustain normal reproduction and growth.

Given an aggregate formed by N bacteria, their energy e_j and volume V_j , $j = 1, \dots, N$, evolve according to

$$\frac{de_j}{dt} = \nu' \left(\frac{S}{S+K_S} - e_j \right), \quad \nu' = \nu e^{-\gamma \varepsilon} \left(1 + \frac{C_{out}}{K_V} \right)^{-1}, \quad (4.9)$$

$$\frac{dV_j}{dt} = \left(r_j \frac{a_j}{a_M} - h_j \right) V_j, \quad r_j = \left(\frac{\nu' e_j - mg}{e_j + g} \right)^+, \quad (4.10)$$

where ν is the energy conductance, ν' the conductance modified by exposure to a toxicant, m the maintenance rate, g the investment ratio, a_M the target acclimation energy, K_S a half-saturation coefficient, K_V the noncompetitive inhibition coefficient and γ the environmental degradation effect coefficient. The factor r_j denotes the bacterial production rate. The symbol $^+$ stands for ‘positive part’, which becomes zero for negative values. The variables S , C_{out} , ε denote the limiting nutrient/oxygen concentration, the concentration of toxic products, and the environmental degradation, respectively. Note that, for spherical bacteria with radius R_j , we have $V_j = \frac{4}{3}\pi R_j^3$. In 2D, $V_j = \pi R_j^2$, and (4.10) implies

$$2 \frac{dR_j}{dt} = \left(r_j \frac{a_j}{a_M} - h_j \right) R_j. \quad (4.11)$$

For rod-like bacteria of radius R and length L_j , $V_j \sim \pi R^2 L_j$. In 2D, $V_j \sim 2R L_j$. For ellipsoidal approximations, $V_j = \pi b L_j$, where b is the small and L_j the great semi-axes, with

$$\frac{dL_j}{dt} = \left(r_j \frac{a_j}{a_M} - h_j \right) L_j. \quad (4.12)$$

These equations must be complemented with equations for cell response to the degradation of the environment and the accumulation of toxicants. The cell undergoes damage, represented by aging q_j and hazard h_j variables, as well as acclimation, represented by the variable a_j . For $j = 1, \dots, N$, these additional variables

are governed by

$$\frac{dq_j}{dt} = e_j(s_G \rho_x \frac{V_j}{V_T} q_j + h_a)(v' - r_j) + k_{tox} C_{in,j} - (r_j + r_{e,j}) q_j, \quad (4.13)$$

$$\frac{dh_j}{dt} = q_j - (r_j + r_{e,j}) h_j, \quad (4.14)$$

$$\frac{dp_j}{dt} = -h_j p_j, \quad (4.15)$$

$$\frac{dC_{in,j}}{dt} = k_{in} C_{out} - k_{out} C_{in,j} - (r_j + r_{e,j}) C_{in,j}, \quad (4.16)$$

$$\frac{da_j}{dt} = (r_j + r_{e,j}) \left(1 - \frac{a_j}{a_M}\right)^+, \quad (4.17)$$

where ρ_x is the cell density, s_G a multiplicative stress coefficient, h_a the Weibull aging acceleration, and k_{tox} , k_{in} , k_{out} the toxicity, influx coefficient and efflux coefficient of toxicants, respectively. The variable $C_{in,j}$ denotes the toxicant cellular density inside the cell and p_j its probability of survival at time t . The factor $r_{e,j}$ is non zero only when the cell is an EPS producer (the values of the parameters m and g may be slightly different for such cells). In that case the rate of EPS production $r_{e,j} = kr_j + k'$, where k is the growth associated yield whereas k' is the non growth associated yield. The produced EPS is then

$$\frac{dV_{e,j}}{dt} = r_{e,j} V_j. \quad (4.18)$$

A fraction $1 - \eta$ of the produced EPS stays around the cell, while a fraction $\eta \in (0, 1)$ diffuses taking the form of a concentration of monomers C_e .

- *Equations for concentrations.* System (4.9)-(4.17) describes the metabolic state of each bacterium, and is coupled to reaction-diffusion equations for the relevant concentrations in Ω :

$$\frac{\partial S}{\partial t} = -v' \frac{S}{S + K_S} \rho_x \sum_j \frac{V_j}{V_T} \delta_j + d_s \Delta S - \mathbf{u} \cdot \nabla S, \quad (4.19)$$

$$\frac{\partial C_e}{\partial t} = \eta \rho_x \sum_j r_{e,j} \frac{V_j}{V_T} \delta_j + d_e \Delta C_e - \mathbf{u} \cdot \nabla C_e, \quad (4.20)$$

$$\frac{\partial C_{out}}{\partial t} = -C_{out} \sum_j r_j \delta_j + d_c \Delta C_{out} - \mathbf{u} \cdot \nabla C_{out}, \quad (4.21)$$

$$\frac{\partial \varepsilon}{\partial t} = v_\varepsilon \rho_x \sum_j (r_j + v_m m) \frac{V_j}{V_T} \delta_j + d_\varepsilon \Delta \varepsilon - \mathbf{u} \cdot \nabla \varepsilon, \quad (4.22)$$

where v_ε is the environmental degradation coefficient, v_m is the maintenance respiratory coefficient and d_ε , d_s , d_e , d_c the diffusion coefficients for degradation ε , limiting oxygen/nutrient concentration S , monomeric EPS C_e , and toxicants C_{out} , respectively. Here δ_j equals one in the region occupied by cell j , it vanishes otherwise. V_T is a reference volume. These equations are typically solved in the computational domain with no flux boundary conditions, except for S , which has a constant supply at the borders, and C_{out} which is supplied at the borders as prescribed.

- *Spread of cellular fields and interpolation of concentration fields.* The system of ordinary differential equations (4.9)-(4.18) and reaction-diffusion equations (4.19)-(4.22) are coupled using a similar philosophy as that in IB models. However, now we transfer information not between curves and a two dimensional region but between confined regions occupied by bacteria and the whole computational domain:
 - Spread of fields defined on bacteria: Equations (4.19)-(4.22) use the cell volumes and rates as sources and sinks for the concentrations.
 - Interpolation of global fields on the bacteria: For each bacterium, system (4.9)-(4.18) uses the averaged values of S , C_{out} , ε in the region occupied by the cell. C_{out} represents the dissolved (extracellular) concentration of toxicants.

4.3 Nondimensionalization of the equations

For computational purposes, it is essential to nondimensionalize properly these sets of equations. This allows us to identify relevant time scales for the different sets of equations, as well as controlling parameters. To remove dimensions we have to choose characteristic values for the different magnitudes. The characteristic length L will tell us what part of the problem we want to focus on, that is, if we prefer to study what happens with the whole set of bacteria and do not want to spend a lot of computational time solving for details, or if we want to give more importance to what happens in the smaller areas. In our case we are interested in small cell aggregates, so we will have a characteristic length of $L = 10[\mu\text{m}]$ (microns, $1\mu\text{m} = 10^{-6}\text{m}$), because it is about the maximum length of rod-like bacteria. In general, it will be the size of a small group of them. Time scales vary: microseconds for fluid processes, seconds for diffusion processes, and hours for cellular processes.

Let us first consider the IB submodel. We set a characteristic time $T = 10^{-6}[\text{s}]$. In equation (4.1), the terms $(u_t + u \cdot \nabla u)$, $\nu \Delta u$ have the same units, regardless of dimension. Let us set $p' = \frac{p}{\rho}$, $\alpha' = \frac{\alpha}{\rho}$. Then, $\mathbf{f}' = \frac{\mathbf{f}}{\rho}$ has units of acceleration. Formally, one can just suppress one dimension in the variables and derivatives and use in 2D:

$$\frac{\partial \mathbf{u}}{\partial t} + \mathbf{u} \cdot \nabla \mathbf{u} = \nu \Delta \mathbf{u} - \nabla p' + \mathbf{f}' - \alpha' \mathbf{u}. \quad (4.23)$$

As a reference acceleration, we set $a_0 = \frac{E}{\rho L} = \frac{E_s}{\rho_s L}$, where E_s is a longitudinal tension in units $[\frac{\text{N}}{\text{m}}]$ (Young modulus for springs) and ρ_s surface density in units $[\frac{\text{kg}}{\text{m}^2}]$. We know 3D values for the parameters. The Young modulus E for bacterial membranes (Tuson et al. 2012) lies in the range 100 – 200 [MPa]. We set $E = 150 \text{ MPa} = 150 \times 10^6 [\frac{\text{N}}{\text{m}^2}]$. The density of water/biomass ρ (Seminara et al. 2012) is about $10^3 [\frac{\text{kg}}{\text{m}^3}]$. In this way, we find a value for a_0 . Regarding the forces (4.2), for the elastic contribution we use (4.4) and (4.5) in 2D, which relates force per unit area to force with δ in units of $\frac{1}{L^2}$.

Name	Symbol	Values	Units
Biomass density	ρ	10^3	[kg/m ³]
Biomass viscosity	μ	100	[kg/(m s)]
Bacterial membrane Young Modulus	E	150×10^6	[kg/(m s ²)]

Table 4.1: Values for dimensional parameters of the IB submodel expressed in their standard units taken from (Tuson et al. 2012) and (Seminara et al. 2012).

Performing the changes of variables indicated in Table 4.2 and dropping the \sim symbol for ease of notation we find the dimensionless IB system with parameters given by Tables 4.1-4.3:

$$\frac{\partial \mathbf{u}}{\partial t_1} + \mathbf{u} \cdot \nabla \mathbf{u} = \frac{1}{Re} \Delta \mathbf{u} - \nabla p + F_c \mathbf{f} - \alpha_0 \mathbf{u}, \quad \text{div}(\mathbf{u}) = 0, \quad (4.24)$$

$$\mathbf{f}(\mathbf{x}, t_1) = \int_0^{2\pi} \mathbf{F}(\theta, t_1) \delta(\mathbf{x} - \mathbf{X}(\theta, t_1)) d\theta, \quad \mathbf{X} = \cup_{j=1}^N \mathbf{X}_j, \quad (4.25)$$

$$\frac{\partial \mathbf{X}}{\partial t_1} = \int_{\Omega} \mathbf{u}(\mathbf{x}, t_1) \delta(\mathbf{x} - \mathbf{X}(\mathbf{q}, t_1)) d\mathbf{x} + \lambda_0 ((\mathbf{F}_g \cdot \mathbf{n})\mathbf{n} + \mathbf{F}_{ext}), \quad (4.26)$$

$$\mathbf{F} = \mathbf{F}_e + \mathbf{F}_g - \mathbf{F}_i, \quad (4.27)$$

$$\mathbf{F}_e = \frac{\partial}{\partial \theta} \left(K_0 \frac{\partial \mathbf{X}}{\partial \theta} \right), \quad \mathbf{F}_{ext} = \mathbf{F}_i, \quad (4.28)$$

$$\mathbf{F}_i = \begin{cases} \sum_{j=1}^N \sum_{n=1, n \neq j}^N \frac{\sigma_0 \delta_j}{d_{min,0}} \mathbf{n}_{cm,n,j} & \text{if } d_{j,n} \leq d_{min,0}, \\ \sum_{j=1}^N \sum_{n=1, n \neq j}^N \frac{\sigma_0 \left(1 + \tanh \left(\frac{s_{p,0} - d_{j,n}}{v_{p,0}} \right) \right) \delta_j}{2d_{j,n}} \mathbf{n}_{cm,n,j} & \text{if } d_{j,n} > d_{min,0}. \end{cases} \quad (4.29)$$

The growth term \mathbf{F}_g would be noticeable in the time scale of hours. In this scale, it is negligible. The effect of growth would come through the boundaries, which move in the time scale of hours due to cellular processes. Here $\lambda_0 \mathbf{F}_g \sim \frac{T}{3600} \sim 10^{-10}$. We can remove \mathbf{F}_g from these equations. The effect of cell metabolism on bacterial boundaries will be calculated directly from the dynamic energy budget (DEB) equations.

$t = T \tilde{t}_1$	$x = L \tilde{x}$	$u = U \tilde{u}$	$\frac{\rho}{\rho} = P \tilde{p}$	$\mathbf{F} = F \tilde{\mathbf{F}}$	$\frac{\mathbf{f}}{\rho} = \frac{\mathbf{f}_s}{\rho_s} = a_0 \tilde{\mathbf{f}}$
$\delta = \frac{1}{L^2} \tilde{\delta}$	$K = K_0 E_s$	$U = \frac{L}{T}$	$P = \frac{L^2}{T^2}$	$F = E_s L$	$a_0 = \frac{E}{L\rho} = \frac{E_s}{L\rho_s}$
$\alpha = \alpha_0 \frac{\rho}{T}$	$\lambda = \frac{\lambda_0}{E_s T}$	$d_{j,n} = L \tilde{d}_{j,n}$	$\sigma = \sigma_0 E_s L^2$	$s_p = s_{p,0} L$	$v_p = v_{p,0} L$

Table 4.2: Change of variables used to nondimensionalize the IB equations. The \sim symbols are dropped for ease of notation after it. Dimensionless parameters K_0 , α_0 , σ_0 , λ_0 , $s_{p,0}$, $v_{p,0}$, as well as the dimensionless numbers Re , F_c and dimensional values for ρ , μ , E are given in Tables 4.1 and 4.3. The unknown value E_s scales out. We assume $E/\rho = E_s/\rho_s$.

Next, we consider the DEB equations for each cell. Recall that the variables e , a , V_j , p_j , C_{in} are dimensionless. Hazard h and aging q have units hour⁻¹ and hour⁻², respectively. We

$Re = \frac{\rho L^2}{\mu T}$	$F_c = \frac{T^2 E}{L^2 \rho}$	α_0	λ_0	K_0	σ_0	$d_{min,0}$	$s_{p,0}$	$v_{p,0}$
10^{-3}	1.5×10^3	10^{-3}	10^4	0.15	0.05	0.01	0.01	0.01

Table 4.3: Dimensionless control parameters for the IB submodel (4.24)-(4.29) when $L = 10^{-5}$ [m] and $T = 10^{-6}$ [s].

remove the dimensions in the variables as indicated in Table 4.4. Taking into account the parameter values listed in Table 4.5, the remaining dimensions for parameters and rates are consistent. We work in a timescale $\tau = 1$ hour, which is the natural step. Dropping again the symbol \sim for ease of notation we find for each cell j

$$\frac{de_j}{dt_2} = \tau v' \left(\frac{s}{s+1} - e_j \right), \quad v' = v e^{-\gamma \varepsilon} \left(1 + \frac{C_{out} K_S}{K_v} \right)^{-1}, \quad (4.30)$$

$$\frac{dV_j}{dt_2} = \left(\tau r_j \frac{a_j}{a_M} - h_j \right) V_j, \quad r_j = \left(\frac{v' e_j - mg}{e_j + g} \right)^+, \quad (4.31)$$

and

$$\frac{dq_j}{dt_2} = e_j (s_G \rho_x V_j q_j + h_a \tau^2) \tau (v' - r_j) + \tau^3 k_{tox} C_{in,j} - \tau (r_j + r_{e,j}) q_j, \quad (4.32)$$

$$\frac{dh_j}{dt_2} = q_j - \tau (r_j + r_{e,j}) h_j, \quad (4.33)$$

$$\frac{dp_j}{dt_2} = -h_j p_j, \quad (4.34)$$

$$\frac{dC_{in,j}}{dt_2} = \tau k_{in} K_S C_{out} - \tau k_{out} C_{in,j} - \tau (r_j + r_{e,j}) C_{in,j}, \quad (4.35)$$

$$\frac{da_j}{dt_2} = \tau (r_j + r_{e,j}) \left(1 - \frac{a_j}{a_M} \right)^+. \quad (4.36)$$

For round bacteria in 2D, $V_j = \pi R_j^2$. Equation (4.31) provides the evolution of $\frac{dR_j}{dt_2}$. The evolution of the boundary due to cell metabolism is given by

$$\frac{\partial \mathbf{X}_j}{\partial t_2} = \frac{dR_j}{dt_2} \frac{\mathbf{X}_j(\mathbf{q}, t_2) - \mathbf{X}_{c,j}(t_2)}{\|\mathbf{X}_j(\mathbf{q}, t_2) - \mathbf{X}_{c,j}(t_2)\|}. \quad (4.37)$$

In a similar way, if the cell is rod-like, its boundary evolves as given by (4.12).

$t = \tau t_2$	$h_j = \tilde{h}_j \tau^{-1}$	$q_j = \tilde{q}_j \tau^{-2}$	$V_j = \tilde{V}_j L^2$	$C_{out} = \tilde{C}_{out} K_S$	$V_T = L^2$
----------------	-------------------------------	-------------------------------	-------------------------	---------------------------------	-------------

Table 4.4: Change of variables for nondimensionalization of the DEB model. We set $\tau = 1$ [hour].

Finally, let us consider next the diffusion problems. The variable ε is dimensionless. The concentrations S , C_e , C_{out} have units mg/l . We set $C = K_S \tilde{C}$ for all the concentrations, $t = T_d \tilde{t}_d$ and same spatial scaling as before, as indicated in Table 4.6. Removing \sim for ease

Symbol	Values	Units
ν	0.84768	[hour ⁻¹]
γ	1	[n.d.]
K_V	154.82	[mg/l]
K_S	0.1	[mg/l]
C_{out}	0.3, 0.7, 3	[mg/l]
g	0.9766	[n.d]
m	0.1266	[hour ⁻¹]
ν_m	0.054703	[n.d.]
a_M	1.6703	[n.d.]
s_G	$0.8921 \cdot 10^{-5}$	[l/mg]
h_a	$1.4192 \cdot 10^{-4}$	[hour ⁻²]
ν_ε	0.23566/12000	[l/mg]
k	2.2371	[mg _{polymer} /mg _{cell}]
k'	0.29	[mg _{polymer} /(mg _{cell} hour)]
η	1/2	[n.d.]
k_{out}	0.17251	[hour ⁻¹]
k_{in}	5.16×10^{-4}	[$\frac{1}{\text{mg hour}}$]
k_{tox}	5.416×10^3	[hour ⁻³]
ρ_x	47000	[mg/l]

Table 4.5: Parameters of the DEB submodel (4.30)-(4.36) expressed in their standard units, adapted from (Klanjscek et al. 2012) and (Birbir et al. 2018). Note that $[mg/l] = [10^{-6}kg/10^{-3}m^3]$. When inserted in the equations, all must be written in the same units of choice. Special attention must be paid to time units, which will be either hours or seconds, which requires multiplying or dividing by 3600.

$t = T_d \tilde{t}$	$x = L \tilde{x}$	$V_j = L^2 \tilde{V}_j$	$S = K_S \tilde{S}$	$C_e = K_S \tilde{C}_e$	$C_{out} = K_S \tilde{C}_{out}$
$V_T = L^2$	$D_c = D \frac{T_d}{L^2}$	$\nu^* = \frac{\nu'}{3600}$	$m^* = \frac{m}{3600}$	$r_j^* = \frac{r_j}{3600}$	$r_{e,j}^* = \frac{r_{e,j}}{3600}$

Table 4.6: Change of variables used to nondimensionalize the equations for concentrations. The \sim symbols are dropped for ease of notation after it.

$d_{\varepsilon,0} = 22$	$d_{s,0} = 10$	$d_{c,0} = 5$	$d_{e,0} = 5$	$D_c = 10$
--------------------------	----------------	---------------	---------------	------------

Table 4.7: Dimensionless parameters used in the concentration submodel (4.38)-(4.41) when $T_d = 1$ [s] and $D = 10^{-9}$ [m²/s].

of notation again, we find the dimensionless equations:

$$\frac{dS}{dt_d} = -T_d \nu^* \frac{S}{S+1} \frac{\rho_x}{K_S} \sum_j V_j \delta_j + d_{s,0} D_c \Delta S - \frac{T_d}{T} \mathbf{u} \cdot \nabla S, \quad (4.38)$$

$$\frac{dC_e}{dt_d} = \eta \frac{\rho_x}{K_S} \sum_j T_d r_{e,j}^* V_j \delta_j + d_{e,0} D_c \Delta C_e - \frac{T_d}{T} \mathbf{u} \cdot \nabla C_e, \quad (4.39)$$

$$\frac{dC_{out}}{dt_d} = -C_{out} \sum_j T_d r_j^* \delta_j + d_{c,0} D_c \Delta C_{out} - \frac{T_d}{T} \mathbf{u} \cdot \nabla C_{out}, \quad (4.40)$$

$$\frac{d\varepsilon}{dt_d} = \nu_\varepsilon \rho_x T_d \sum_j (r_j^* + \nu_m m^*) V_j \delta_j + d_{\varepsilon,0} D_c \Delta \varepsilon - \frac{T_d}{T} \mathbf{u} \cdot \nabla \varepsilon, \quad (4.41)$$

with parameters given in Tables 4.5 and 4.7. Notice that v' , m , r_j and $r_{e,j}$ have units hour^{-1} . To be used in these equations, they have to be expressed in units of s^{-1} , that is, divided by 3600. We denote those values by v'^* , m^* , r_j^* and $r_{e,j}^*$. The new diffusion coefficients will be large, the same as $\frac{1}{Re}$. Both systems for fluids and concentrations should relax fast to an equilibrium. We are interested in stationary solutions, to be more precise, quasi-stationary, in the sense that they change with time when the immersed boundaries grow/split/die or the sources vary. That happens in a much longer time scale of hours.

4.4 Computational model for unconstrained spread

As said earlier, we are interested in two kinds of two dimensional reductions of three dimensional geometries representing biofilm spread on a surface. The first one consists of top views of early biofilm stages, see Figure 1.2. In the second one, we consider a 2D diametral slice of a 3D biofilm, see Figure 1.3. Let us focus on the first one, which can be handled with the equations and nondimensionalizations summarized in the previous two sections. The second one requires additional details that we will explain later.

To fix ideas, we consider that the computational region has a reference size around $100 \times 100 [\mu\text{m}]$, that is, $10L \times 10L$ when $L = 10 [\mu\text{m}]$. We place a few bacteria at the center of this region, and let nutrients and toxicants diffuse from the boundaries. While a biofilm spreads on an interface with air, bacteria barely move, except when pushed by the rest. They grow up to their division or shrink until their death. The bacterial cluster tends to spread in the direction of the nutrient/oxygen concentration gradient. As they divide, bacteria occupy the free space and remain at a small distance from their neighbors. The average diameter of spherical bacteria is about $0.5 - 2.0 [\mu\text{m}]$. For rod-shaped or filamentous bacteria, the average length is about $1 - 10 [\mu\text{m}]$ and diameter is about $0.25 - 1.0 [\mu\text{m}]$. In our simulations we have taken for spheres $R = 0.025 - 0.1 [\mu\text{m}]$, and for rods diameter $0.05 - 0.1 [\mu\text{m}]$ and length $0.1 - 1 [\mu\text{m}]$, nondimensionalized divided by the reference length L . Figure 4.1 illustrates some simulations.

Once we have fixed an initial bacterial arrangement and set initial conditions for all the variables we distinguish three blocks of equations. The DEB equations for each cell (4.30)-(4.37) are solved in the time scale of hours. In that time scale, the IB equations (4.24)-(4.29) and the equations for chemical processes (4.38)-(4.41) are quasistationary, changes are induced by growth, division, or destruction or boundaries according to the DEB submodel and the criteria for division, death or interaction. We solve them using time relaxation, that is, we solve the time dependent problems until the solutions relax to a stationary state. More precisely, we proceed as follows. First, we integrate the DEB system for all cells. Then, we relax the Ib2d model with interaction force to a stationary state, and finally the concentrations relax to their stationary state in the diffusion time scale. The process is schematized in Flowcharts 4.2 and 4.3. We next give details about the discretization and the initialization procedures.

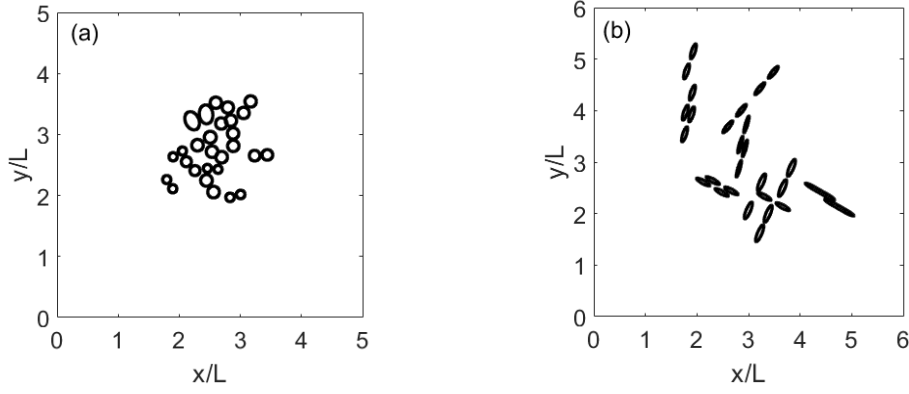


Figure 4.1: Snapshots of the evolution of a few bacteria with initial random sizes varying in the ranges specified in the text. Clusters formed by (a) round and (b) rod-like bacteria, see Video1 and Video2.

4.4.1 Discretization

We define in the computational region a square mesh $\mathbf{x}_{i,j} = (x_i, y_j)$, $i, j = 0, \dots, N$, with step $dx = dy = h$ and nodes $x_i = x_0 + idx$, $y_j = y_0 + jdy$, where $x_0 = y_0 = 0$, $x_N = y_N = \mathcal{L}$. We keep this mesh for all the submodels. However, the three submodels use different time discretizations. The main time mesh is $t_\ell = \ell dt$, $\ell = 0, \dots, M$, up to the final time $\mathcal{T} = Mdt$. For each cell, the systems of ordinary differential equations (4.30)-(4.37) are discretized by a classical Runge-Kutta 2 or 4 scheme (Isaacson et al. 1994) on that mesh with step $dt = 0.01$. For the other two submodels we seek stationary solutions. We use the time dependence to implement time relaxation schemes to approximate them with adapted time steps. The reaction-diffusion equations (4.38)-(4.41) are discretized by classical explicit finite difference schemes (Isaacson et al. 1994). We use first order explicit progressive differences in time and second order approximations for the diffusion and transport terms. The whole set of equations for the immersed boundaries (4.24)-(4.28) are discretized using the finite difference schemes, quadrature rules and discrete δ_h functions described in (Peskin 2002).

The immersed boundaries are parametrized by the angle $\theta \in [0, 2\pi]$. We use a mesh $\theta_k = kd\theta$, $k = 0, \dots, \mathcal{K}$, on them. To prevent the distances between mesh points which form the immersed boundaries becoming too large as they grow, we increase the number of points in each of them at a certain rate, adding single points (in the case of round shapes) or opposite couples in the lateral walls (in the case of elongated shapes), at the sites where the distance between two neighboring mesh points is larger. This deserves further explanation, since it leads to work with a non uniform angle mesh and with angle dependent elastic moduli, which change as points are added. Given a mesh θ_k for a boundary \mathbf{X}_j , with steps $d\theta_k = \theta_k - \theta_{k-1}$, $k = 1, \dots, \mathcal{K}$, we include a new point between sites $i-1$ and i as follows:

- Set $d\theta_i = d\theta_i/2$, $d\theta_{i+1} = d\theta_i/2$, and $d\theta_{i+m} = d\theta_{i+m-1}$, $1 < m < \mathcal{K} - i + 1$.

- Set $\theta_i = \theta_{i-1} + d\theta_i$, $\theta_{i+1} = \theta_i + d\theta_{i+1}$, and $\theta_{i+m} = \theta_{i+m-1}$, $1 < m < \mathcal{K} - i + 1$.
- Set $\mathbf{X}_j(\theta_i) = \frac{\mathbf{X}_j(\theta_{i-1}) + \mathbf{X}_j(\theta_i)}{2}$, and $\mathbf{X}_j(\theta_{i+m}) = \mathbf{X}_j(\theta_{i+m-1})$, $0 < m < \mathcal{K} - i + 1$.
- Set $K_j(\theta_i) = 2K_j(\theta_i)$, $K_j(\theta_{i+1}) = 2K_j(\theta_i)$, and $K_j(\theta_{i+m}) = K_j(\theta_{i+m-1})$, $1 < m < \mathcal{K} - i + 1$, to prevent the reduction in the angle from changing the continuum limits.
- Set $\mathcal{K} = \mathcal{K} + 1$.

Additionally, we need rules for killing cells and dividing cells, which we detail next.

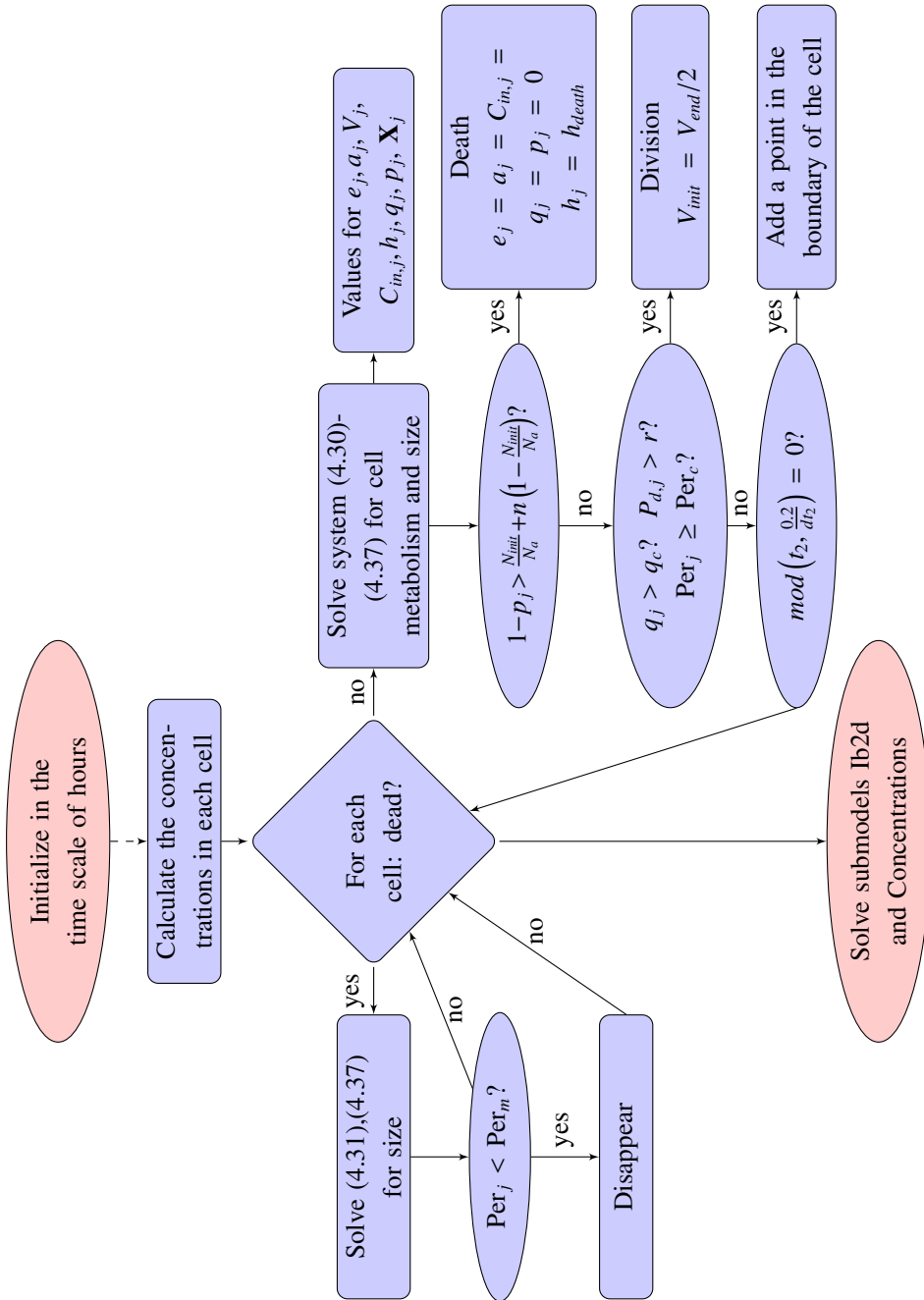


Figure 4.2: Flowchart for cell evolution in the time scale of hours.

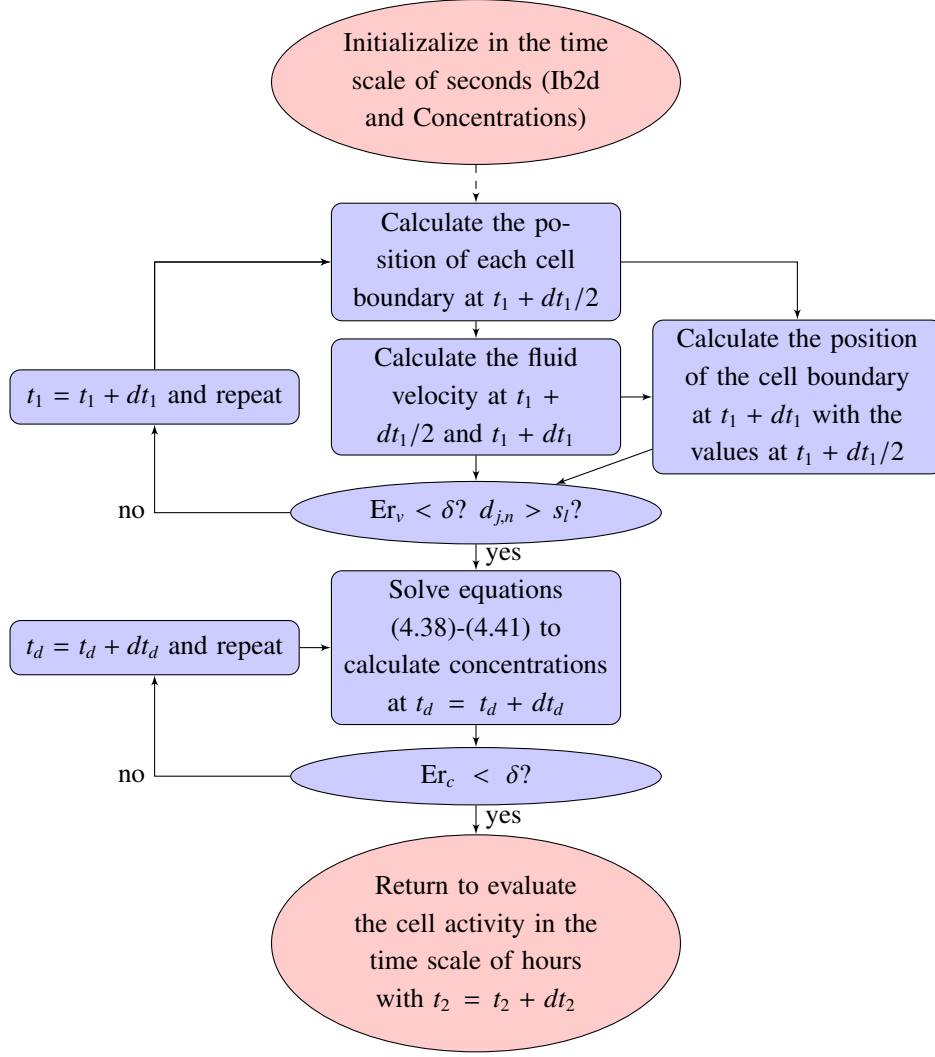


Figure 4.3: Flowchart for the submodels governing IB and chemical processes.

4.4.2 Rules for division and death

Once the size of a bacterium \mathbf{X}_j surpasses a critical perimeter, the cell divides with probability $P_{d,j} = \frac{S_j}{S_{j+1}}$, S_j being the averaged value of the limiting concentration at the cell location, provided their aging acceleration q_j is larger than a critical value q_c (a way to indicate age, not to kill newborn cells). More precisely, for each cell boundary \mathbf{X}_j :

- We check whether $q_j > q_c = 10^{-8}$.
- We check whether its length Per_j is larger than a critical perimeter $\text{Per}_c = 1.4 \text{Per}_{\text{init,max}}$ for spheres and $\text{Per}_c = 1.5 \text{Per}_{\text{init,max}}$ for rod-like bacteria, where $\text{Per}_{\text{init,max}}$ is the maximum perimeter in the initialization step.
- We generate a random number $r \in (0, 1)$ and check whether $P_{d,j} > r$.

Figures 4.4 and 4.5 illustrate the division process for spherical and rod-like bacteria. Division is completed in a few steps: the cell elongates and then splits conserving area. For

spherical bacteria, if $V_{init} = \pi R_{init}^2$ is the volume before division, we have radius $R_{end} = \frac{R_{init}}{\sqrt{2}}$ for the two daughters. For rod-like bacteria, with initial volume $V_{init} = \pi b a_{init}$, being b the smallest semi-axis, we have $a_{end} = \frac{a_{init}}{2}$ for the two daughters, because b is constant. We reset all the cell variables to their initial values after division, see Section 4.4.3.

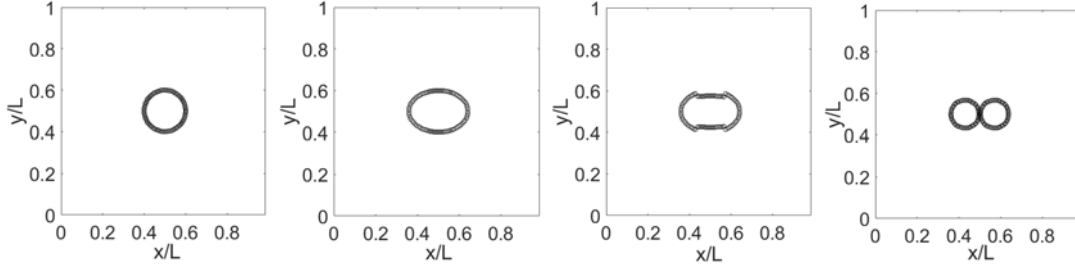


Figure 4.4: Snapshots of the division of a spherical bacterium.

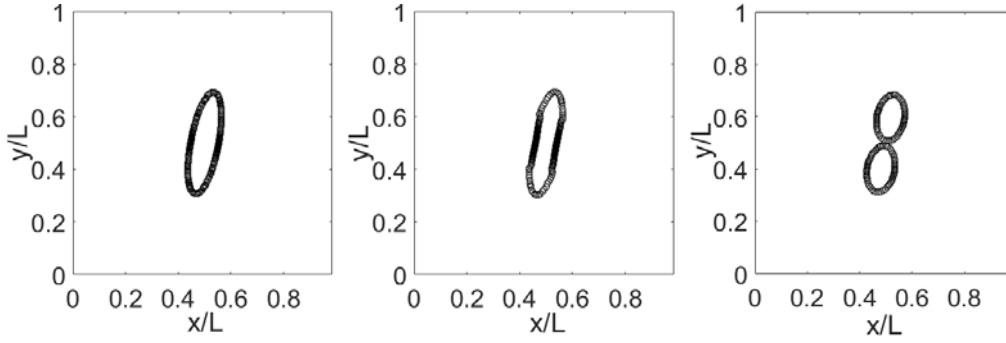


Figure 4.5: Snapshots of the division of a rod-like bacterium.

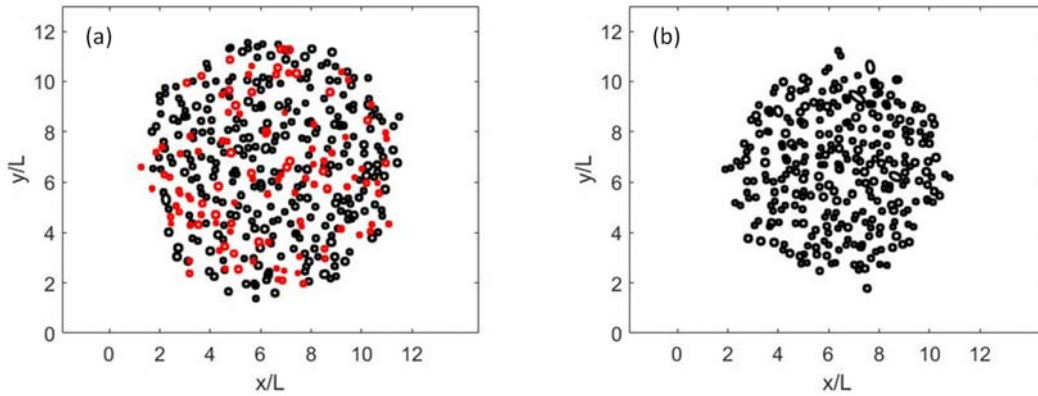


Figure 4.6: Snapshots of the evolution of a circular biofilm formed by 100 cells under the same conditions but different death treatment: (a) Shrinking dead cells (represented in red). We have 292 alive cells and 108 dead ones. (b) Erasing dead cells. We have 294 alive cells and have erased 86.

Similarly, the cell \mathbf{X}_j dies with probability defined by p_j , $j = 1, \dots, N$. We kill \mathbf{X}_j when $1 - p_j > \frac{N_{init}}{N_a} + r \left(1 - \frac{N_{init}}{N_a}\right)$, where N_a is the current number of bacteria, N_{init} the initial number of bacteria and $r \in (0, 1)$ a random number. The rationale behind this criterion

is as follows. The individual probability $p(t)$ gives the probability of a cell being alive at time t . If we chose to kill cells with probability $1 - p(t)$, the final number of cells which survive during the simulation depends on how often we check its dead or alive status. Instead, this kind of rules removes that spurious phenomenon. These criteria can be adjusted to reproduce experimental counts or trends of the number alive bacteria under different environmental situations (Birnir et al. 2018; Ishida et al. 1998), as we will discuss later.

When a bacterium dies we have two options: 1) erase the cell immediately, 2) keep it and solve only equations (4.31) for the volume, so that it shrinks slowly due to reabsorption, see Figure 4.6. The latter option may produces a more realistic evolution in some cases, to account for necrotic regions which otherwise would be erased. We solve the whole set of equations (4.30)-(4.37) for the living cells, but only Eq. (4.31) for the dead cell, fixing $h = h_{death}$. For spheres, when the dead cell's perimeter is below a minimum threshold $Per_m = \pi dx$, dx being the spatial discretization step, the cell disappears. For rod-like bacteria we take $Per_m = 2\pi b$, being b the shortest semi-axis. The parameter h_{death} governs the speed of the perimeter decrease. We choose to increase h_{death} with the number of alive cells surrounding the dead one, since it represents reabsorption. More precisely, we set $h_{death,j} = h_{death,j} + dt Nc_{C_i < Rd}$, where $Nc_{C_i < Rd}$ is the number of cells whose center lies at a distance smaller than $Rd = 3/L$ for cell j and $dt = dt_2$.

4.4.3 Initialization and boundary conditions

A typical geometry initialization is represented in Figure 4.7(a). We define N non overlapping immersed boundaries (either spheres or rods) in the region $13L \times 13L$ for sphaera and $17L \times 17L$ for rod-like bacteria, located inside a circle of a given radius. The centers, dimensions, axis orientation (when required), and number of points forming the boundaries, vary randomly about given values. Next,

- We create the cubic mesh of step dx in that region to discretize the fluid and the reaction-diffusion equations.
- We set the initial velocity \mathbf{u} equal to zero everywhere and periodic boundary conditions for the fluid velocity.
- A reference value $S_0 = 10$ is fixed as initial and Dirichlet boundary condition for the concentration at the borders of the computational region.
- We set $C_e(0) = 0$ and $\varepsilon(0) = 0$ everywhere and enforce zero Neumann boundary conditions for them.
- For the first simulations, we set $C_{out}(0) = 0$ everywhere and enforce zero Dirichlet boundary conditions. Once the biofilm seed has evolved for some time, we switch to a Dirichlet boundary condition $C_{out} = 3, 7, 30$ on the borders of the computational

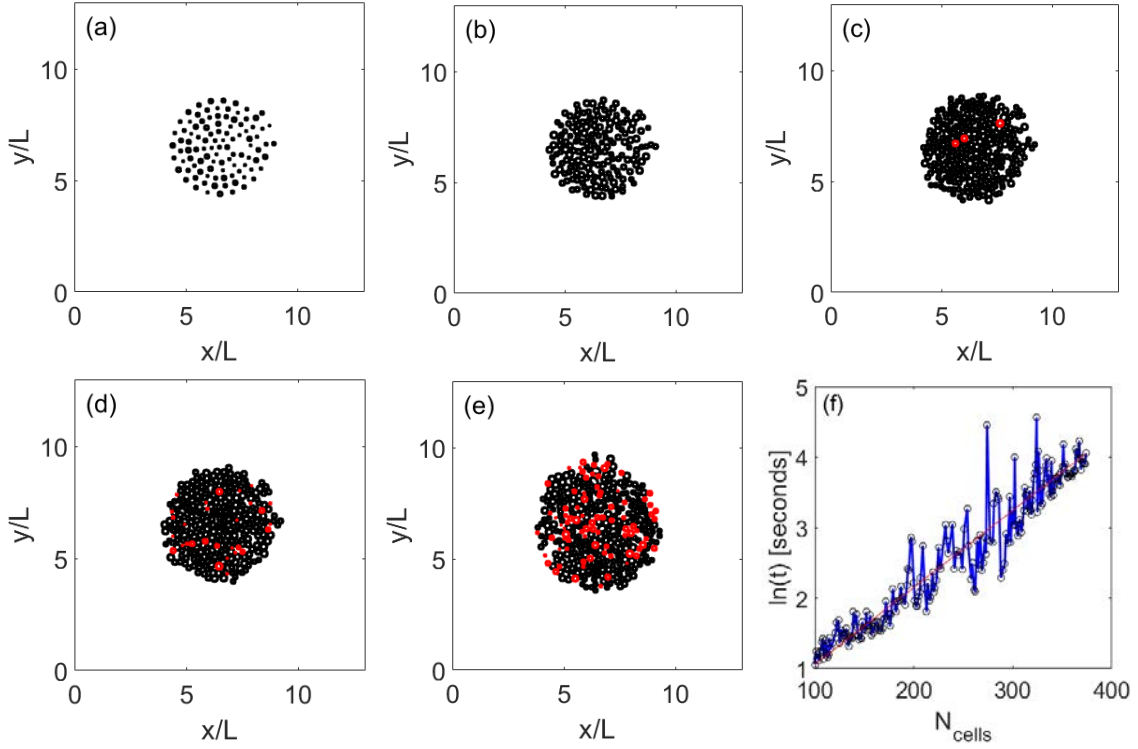


Figure 4.7: (a) Initial arrangement. Evolution at (b) $t = 9$ h, (c) $t = 12$ h, (d) $t = 14$ h, (e) $t = 20$ h. The simulation starts with 100 cells and ends up with 286 cells alive, 81 dead (red) and 179 already erased, see Video3. Panel (f) represents the computational time for one iteration as a function of the number of spheres, as the number of cells grows during a simulation (coded in Matlab). An exponential fit (red) indicates that the computational time for one whole step grows as $Ce^{\gamma N}$, where $C = 1.04[s]$, $\gamma = 0.0106$, and N is the number of spheres. One step with 350 spheres takes about 40 seconds.

region. As initial condition for C_{out} we use the profile obtained by relaxation of (4.40) with the boundary condition and without the convective term.

- For $j = 1, \dots, N$ we set $V_j(0)$ equal to the initial dimensionless areas, $e_j(0) = \frac{S_j(x_j, 0)}{S_j(x_j, 0) + 1}$, x_j being the center of cell j , $V_{e,j}(0) = 0$, $q_j(0) = 0$, $h_j(0) = 0.6$, $p_j(0) = 1$, $a_j(0) = 0$, and $C_{in,j}(0) = 0$. When we divide a cell, they start with the same initial conditions, except $C_{in,j}$ in the presence of a toxicant, which divides a random percentage to one and the opposite to the other.

As said earlier, we use a specific discretization of the Immersed Boundary model, solving (4.24)-(4.29) by Fourier transforms (Peskin and McQueen 1995; Peskin 2002). We use the time t_1 as an artificial time until the system relaxes to a stationary state, with step $dt_1 = 10^{-6}$. When the relative errors of the fluid-IB variables Er_v fall below a tolerance δ , we use the time t_d as an artificial time until the concentration system relaxes to a stationary state with a step $dt_d = 10^{-9}$ for spheres and $dt_d = 10^{-11}$ for rods, due to the convection factor $T_d/T = 10^6$. When the relative errors Er_c fall below a tolerance δ , we stop. We set $\delta = 10^{-3}$. We also demand that the cells remain at a certain distance s_l , in

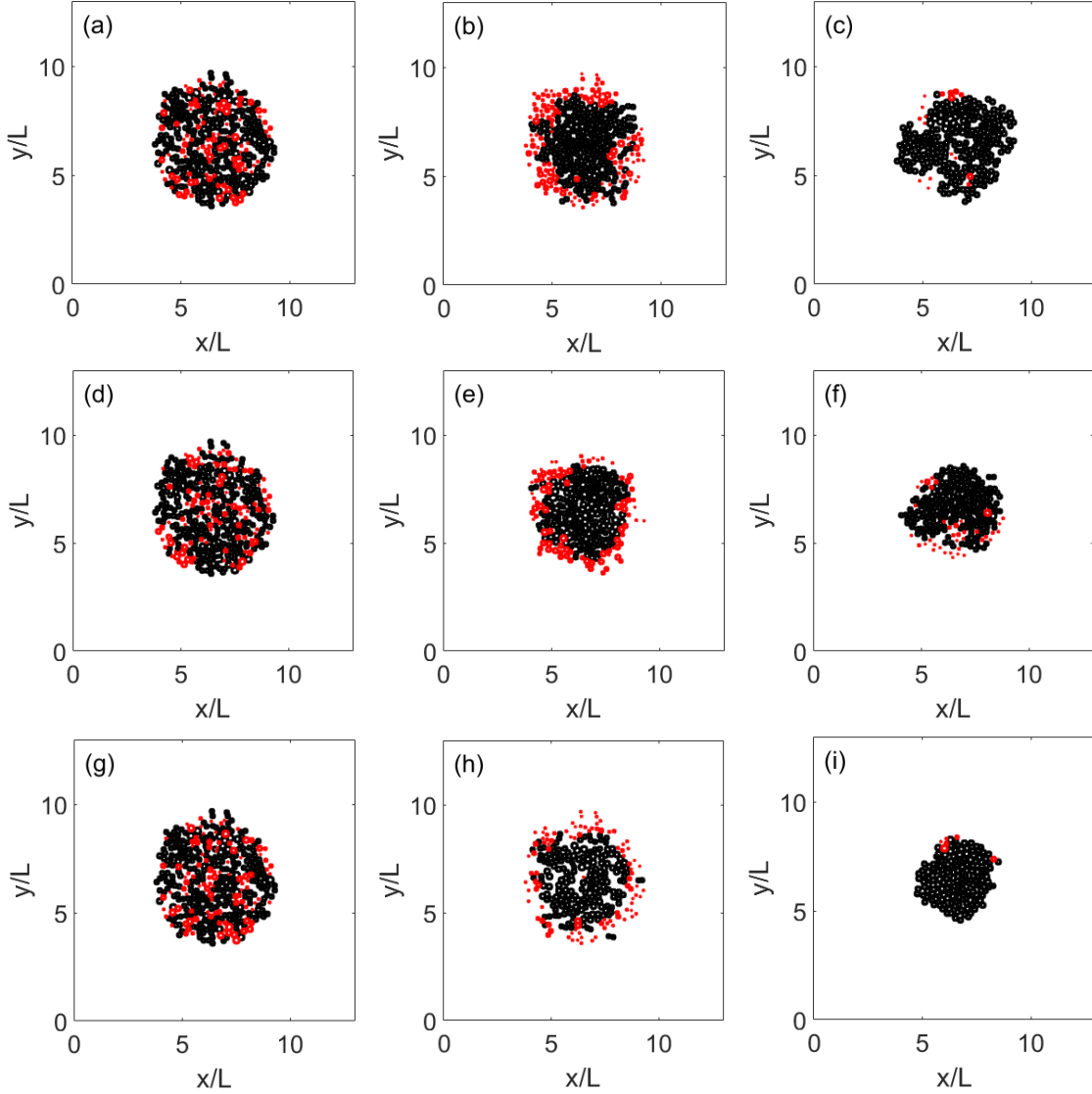


Figure 4.8: Evolution of the final configuration reached in Fig. 4.7 under the action of antibiotics. Snapshots for $C_{out} = 3$ at (a) $t = 1$ h, (b) $t = 6$ h, and (c) $t = 12$ h. The simulation ends with 260 cells alive, 17 dead (red) and 419 already erased, see Video3a. Snapshots for $C_{out} = 7$ at (d) $t = 1$ h, (e) $t = 5$ h, and (f) $t = 12$ h. The simulation ends with 213 cells alive, 38 dead (red) and 390 already erased, see Video3b. Snapshots for $C_{out} = 30$ at (g) $t = 1$ h, (h) $t = 3.5$ h, and (i) $t = 10$ h. The simulation ends with 162 cells alive, 6 dead (red) and 354 already erased, see Video3c. If we do not erase them, we have a necrotic outer layer of increasing thickness.

these tests we have set $s_I = 0$.

4.4.4 Dynamics of incipient biofilms

Figures 4.7-4.8 show a few snapshots of the evolution of an incipient circular biofilm formed by spherical bacteria, without antibiotic and with antibiotics, respectively, see also

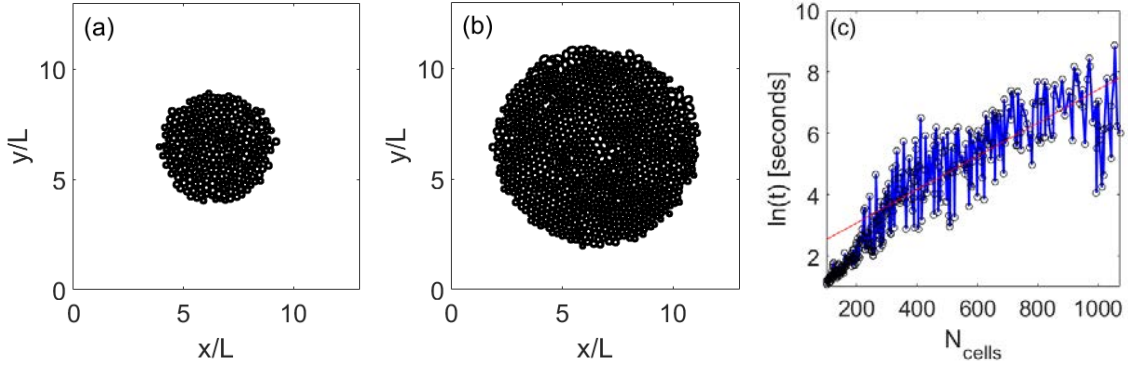


Figure 4.9: Biofilm growth without cell death ($h_0 = 0$). (a) $t = 10$ h, (b) $t = 16$ h, reaching 1116 cells. Panel (c) represents the computational time for one iteration as a function of the number of cells, as the number of cells grows during a simulation (coded in Matlab). An exponential fit (red) indicates that the computational time for one whole step grows as $Ce^{\gamma N}$, where $C = 7.372[s]$, $\gamma = 0.0054$, and N is the number of cells. One step with 1000 cells takes about 28 minutes, much slower than initial stages with 300.

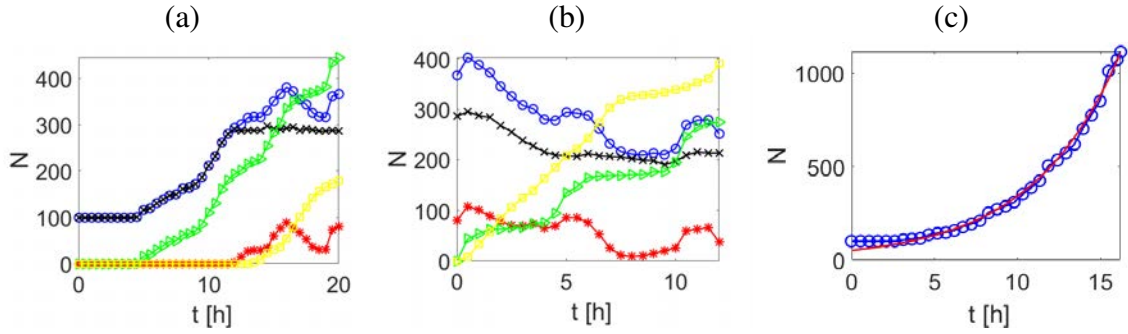


Figure 4.10: Counts of cell types versus time for different simulations: (a) Spheres in Figure 4.7. (b) Spheres with antibiotics in Figure 4.8(d-f). The blue circles, black crosses, red asterisks, yellow squares and green triangles represent total number of cells (live and dead), live cells, dead cells, accumulation of new cells and accumulation of erased cells, respectively. (c) Alive cells in Figure 4.9, without death. The solid line represents the fitting $N \sim Ce^{\gamma t}$, being t in hours and $C = 51.5321$, $\gamma = 0.1894[h^{-1}]$.

Videos 3, 3a, 3b, 3c. The action of antibiotics would vary depending on parameters we have fixed, such as the toxicity, and the parameters governing the flux inside and outside the cells. We see that as the antibiotic presence is increased, growth slows down, less cells remain, and an outer necrotic region appears, that finally dissolves in the surrounding fluid and is absorbed by the remaining cells. However, the secreted polymeric substances still remain in that region. The dynamics of dead cells depends on the governing parameters we choose to govern the reabsorption process. Figure 4.10 shows the evolution of the number of alive and dead cells, as well as the cumulative numbers of erased and newborn cells. We calibrated the death parameters to reach a certain aggregate size in the absence of antibiotics, as a result of a balance between dead and newborn cells (as it happens in many tissues). When we set $h_0 = 0$, the size of the aggregate grows continuously, see

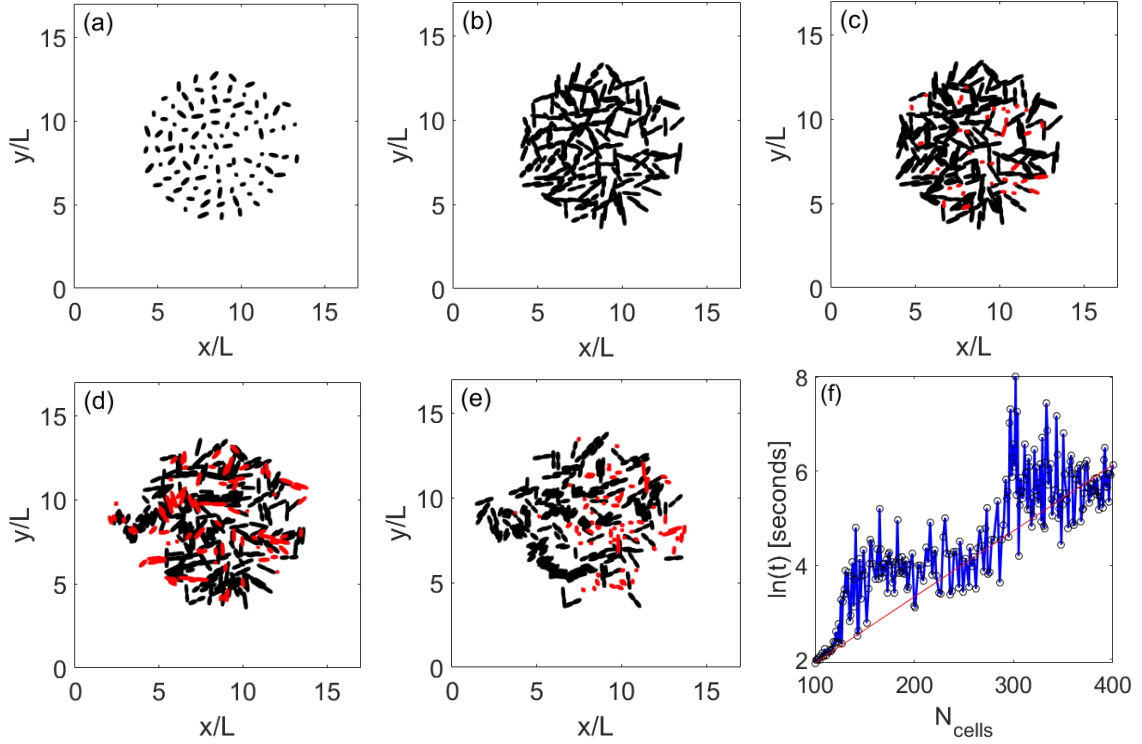


Figure 4.11: (a) Initialization. Evolution at (b) $t = 9.5$ h, (c) $t = 12$ h, (d) $t = 14$ h and (e) $t = 20$ h, without antibiotics. We started with 100 bacteria, and ended with 289 alive, 68 dead (red) and 267 disappeared, see Video4. Panel (f) represents the computational time for one iteration as a function of the number of rods, as the number of cells grows during a simulation (coded in Matlab). An exponential fit (red) indicates that the computational time for one whole step grows as $Ce^{\gamma N}$, where $C = 1.86[s]$, $\gamma = 0.0138$, and N is the number of rods. One step with 350 rods takes about 3 – 4 minutes. Oscillations are due to variations in the time required to calculate the interactions depending on the overall rod orientation and arrangement.

Figure 4.9. Figures 4.11-4.12 illustrate the evolution for rod-like bacteria, see also Videos 4, 4a, 4b, 4c.

The computational times indicated in Figures 4.7(f), 4.9(c) and 4.11(f) are obtained for Matlab Codes, with partial parallelization using 12 threads. Only the resolution of systems of ordinary differential equations for the cells, the conversions of cell positions to vector structure used for vectorization of fluid and concentration equations, the computation of elastic forces for cells, and the membrane growth have been parallelized in these computations. Paralellizing cell division, cell death and cell interactions is much more involved and we have not implemented it.

We can adapt the previous framework to investigate spatial competition between spherical and rod-shaped bacteria in the biofilm. To do so, we add a new variable (Type) to each cell, which takes values 0 for spheres and 1 for rods. Then, the two previous codes for spheres and rods are merged. We include also the interaction sphere-rod, which is calcu-

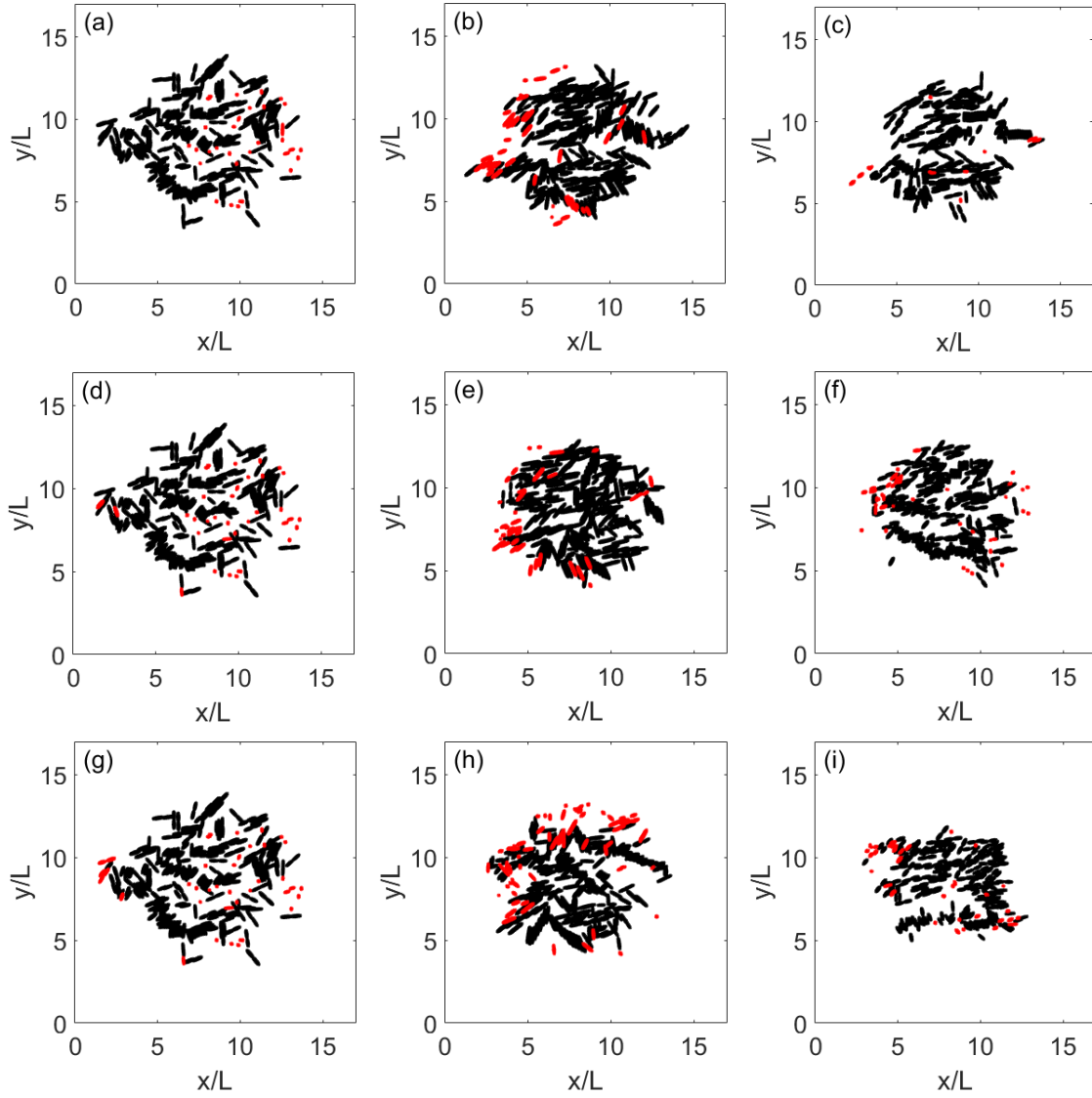


Figure 4.12: Evolution of the final configuration reached in Fig. 4.11 under the action of antibiotics. Snapshots for $C_{out} = 3$ at (a) $t = 1$ h, (b) $t = 7.5$ h, and (c) $t = 10$ h with 284 alive, 14 dead (red) and 358 erased, see Video4a. Snapshots for $C_{out} = 7$ at (d) $t = 1$ h, (e) $t = 7.5$ h, and (f) $t = 10$ h with 278 alive, 40 dead (red) and 340 erased, see Video4b. Snapshots for $C_{out} = 30$ at (g) $t = 1$ h, (h) $t = 3$ h, and (i) $t = 10$ h with 246 alive, 34 dead (red) and 346 erased, see Video4c.

lated as the interaction rod-rod. Figure 4.13 shows how rod-like bacteria dominate, see also videos Video_h1, Video_h2. Notice the tendency of rods to align. Compare Fig. 4.13, and also Fig. 4.1, to the experimental images in Fig. 1.2.

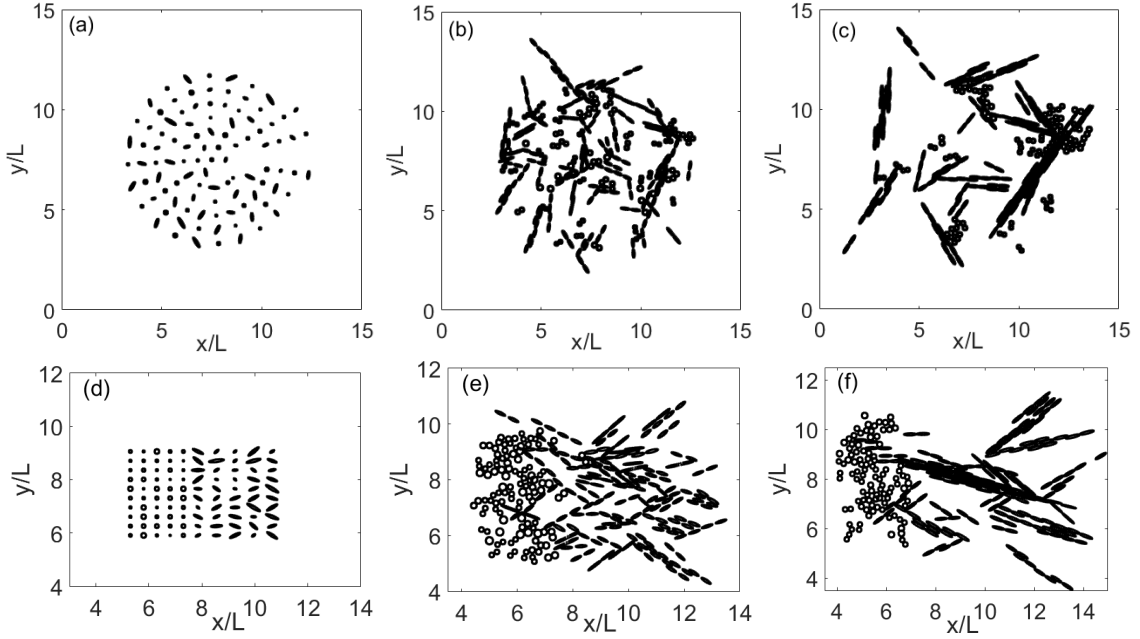


Figure 4.13: Evolution of a hybrid aggregate formed by spherical and rod-like bacteria starting from randomly distributed shapes (a)-(c) and from clusters of different shapes (d)-(f). Panels (a) and (d) represent the initial configuration. Panels (b), (e) and (c), (f) represent configurations at times 20 h , 40 h, respectively. They have been drawn ignoring the dead cells. Rod-like bacteria conquer more space, and achieve larger numbers of alive cells. Starting with 50 bacteria of each type, we reach 183 and 184 live rod-like bacteria compared to 105 and 103 live spheres, in the first row and second row respectively.

4.5 Computational model in the presence of barriers

As mentioned earlier, we are interested in two kinds of two dimensional reductions. So far, we have considered the horizontal spread of a two dimensional cluster. We focus here on the arrangement depicted in Figure 1.3: a biofilm slice expanding on a surface. The model equations remain the same as in Sections 4.3 and 4.4. The main change concerns the geometry: we introduce a boundary orthogonal to the biofilm slice representing the interface on which it grows. We place bacteria on a semi-circle on top of it, see Figure 4.14(a). We will exploit the strategy developed in Section 4.4, including additional equations for the horizontal barrier. We impose on it the same equations as for the cell boundaries, without the growth force, and without interaction force (bacteria do not move the barrier). On the other hand, cells do notice the presence of the barrier and the corresponding interaction is included for them. Moreover, in equation (4.5), in front of the integral, we add a factor 0.001 to account for higher density of the barrier and almost negligible barrier mobility due to fluid.

The main variations arise when working with rod-like bacteria. We set $dt_d = 10^{-10}$. In this case, forces can generate a moment that rotate bacteria. This force creates a torque, \mathbf{M}_f , that then varies the angular momentum \mathbf{L} , and knowing the moment of inertia $\mathbf{L} =$

$\mathbf{I}\mathbf{w}$, we obtain the angular velocity \mathbf{w} , \mathbf{I} being the body's inertia tensor.

$$\mathbf{M}_f = \mathbf{X} \times \mathbf{F}_i, \quad \frac{d\mathbf{w}}{dt} = \mathbf{I}^{-1}\mathbf{M}_f. \quad (4.42)$$

In two-dimensions, directions of \mathbf{M}_f and \mathbf{w} are perpendicular to the plane. Thus, we only need the moment of inertia of the axis perpendicular to the plane, which is $I = \frac{1}{4}M(a^2 + b^2)$ for elliptical shapes, where a is the long semi-axis, and b the short one. M is the mass of the bacteria, $M = \rho_x V$, where ρ_x is bacterial density and V its volume. In two-dimensions, they become surface density and area. In this way, we can add in Eq. (4.3) the following expression

$$\frac{\partial \mathbf{X}}{\partial t} = \mathbf{w} \times \mathbf{X}. \quad (4.43)$$

When we nondimensionalize, we need to include in the right hand side of Eq. (4.26) the term $\mathbf{w} \times \mathbf{x}$ with

$$\frac{d\mathbf{w}}{dt} = C_f \mathbf{I}_0^{-1} \mathbf{M}_f, \quad \mathbf{M}_f = \mathbf{x} \times \mathbf{F}_i, \quad (4.44)$$

where all terms are dimensionless, and $C_f = T^2 \frac{E_s L^2}{\rho_{x,s} L^2} = \frac{150}{47} 10^{-6}$ is a dimensionless number, calculated using $\frac{E_s}{\rho_{x,s}} = \frac{E}{\rho_x}$. Moreover, $\mathbf{I}_0 = \frac{1}{4}M_0(a_0^2 + b_0^2)$, where $M_0 = V$, $V = \pi a_0 b_0$ is dimensionless bacterial area and $a_0 = a/L$, $b_0 = b/L$.

A new feature we wish to represent in this new set-up is the observation that fluid flows upwards through the horizontal barrier because the bacterial biofilm seed swells. We are representing the threads keeping together bacteria in the biofilm as interaction forces keeping bacteria at a distance. When the biofilm swells, those threads swell and elongate too. We model this fact changing the minimum distance between bacteria in the biofilm.

For spherical bacteria, we modify the repulsive force because it is not the same to push upwards than horizontally without the force of gravity. The force is of lesser magnitude and the repulsion occurs more gradually:

$$\mathbf{F}_i = \sum_{j=1}^N \mathbf{F}_{i,j} \delta_j, \quad \mathbf{F}_{i,j} = \sum_{n=1, n \neq j}^{N-1} \sigma_b e^{-\frac{d_{jn}^2}{l_{sp}}} \mathbf{n}_{cm,n,j}, \quad (4.45)$$

σ_b is the repulsive parameter, and l_{sp} sets the maximum distance, where the cells begin to repel. The latter term changes over time, as swelling causes the strings that separate the cells to grow. We have set

$$l_{sp} = l_{max} \frac{1 + \tanh(v_s(t - T_p))}{2} \quad s_{p2} = \sqrt{-\ln(v_{min})} l_{sp}, \quad (4.46)$$

where $l_{max} = -\frac{s_{max}^2}{\ln(v_{min})}$ and v_s is related to the growth of this distance. It saturates at a certain time, we use an inflection point T_p , and a certain maximum length l_{max} . This value depends on the maximum separation of the cells s_{max} and a minimum variation v_{min} .

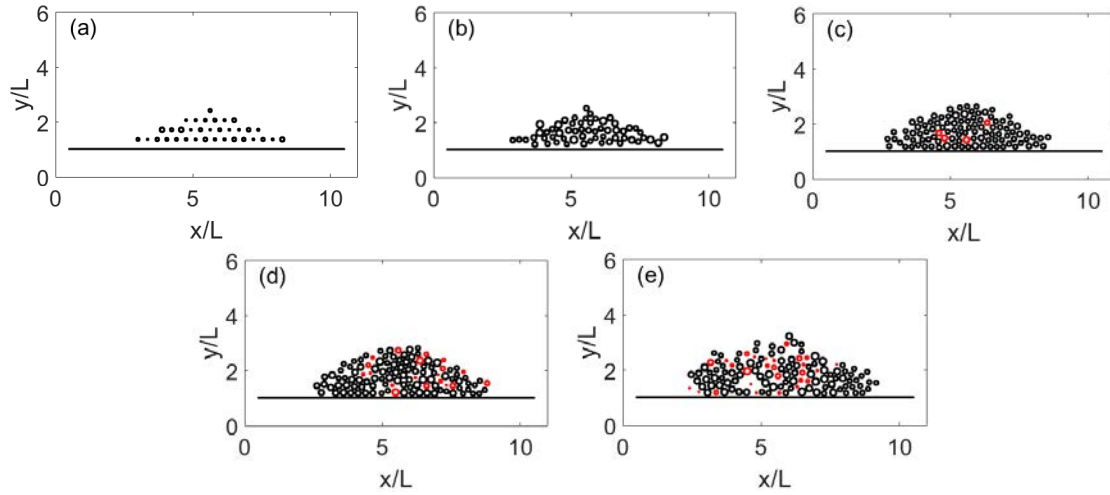


Figure 4.14: (a) Initial arrangement. Evolution at (b) $t = 9$ h, (c) $t = 12$ h, (d) $t = 15$, (e) $t = 20$ h. The simulation starts with 34 cells and ends with 97 alive cells, 27 dead cells (red) and 58 cells already erased, see Video5.

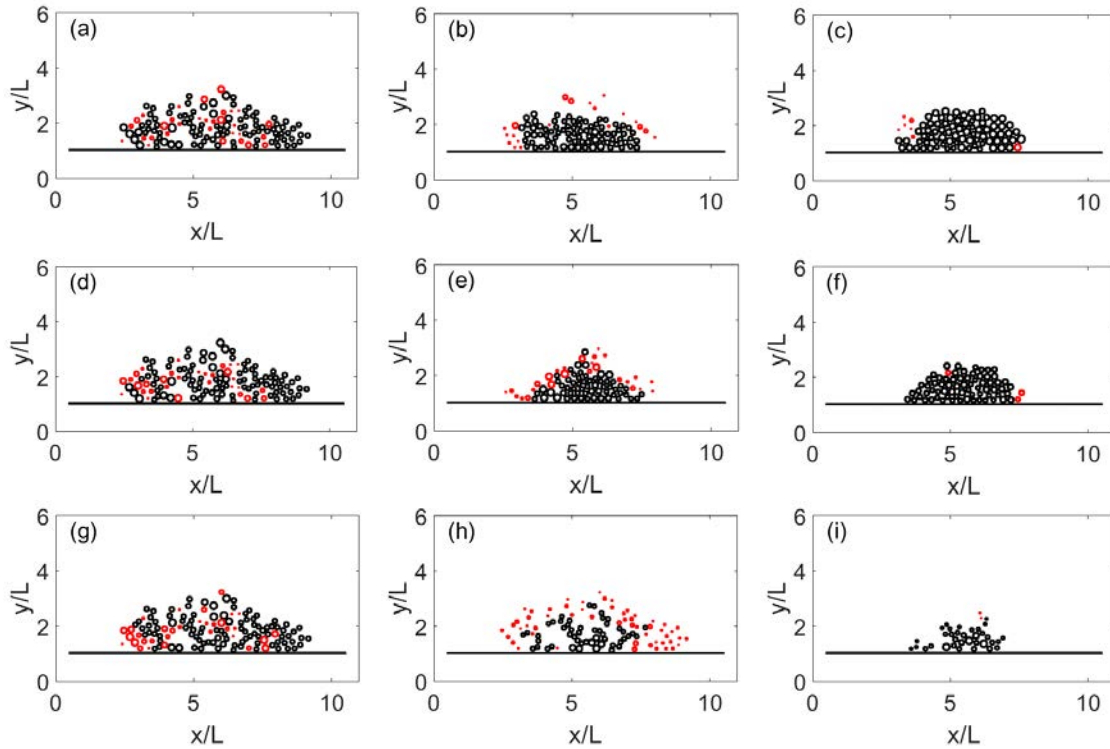


Figure 4.15: Evolution of the final configuration reached in Fig. 4.14 under the action of antibiotics. Snapshots for $C_{out} = 3$ at (a) $t = 1$ h, (b) $t = 7.5$ h, and (c) $t = 10$ h. The simulation ends with 77 cells alive, 7 dead (red) and 120 erased, see Video5a. Snapshots for $C_{out} = 7$ at (d) $t = 1$ h, (e) $t = 7$ h, and (f) $t = 10$ h. The simulation ends with 69 cells alive, 3 dead (red) and 125 erased, see Video5b. Snapshots for $C_{out} = 30$ at (g) $t = 1$ h, (h) $t = 3.5$ h, and (i) $t = 10$ h. The simulation ends with 34 cells alive, 2 dead (red) and 116 erased, see Video5c.

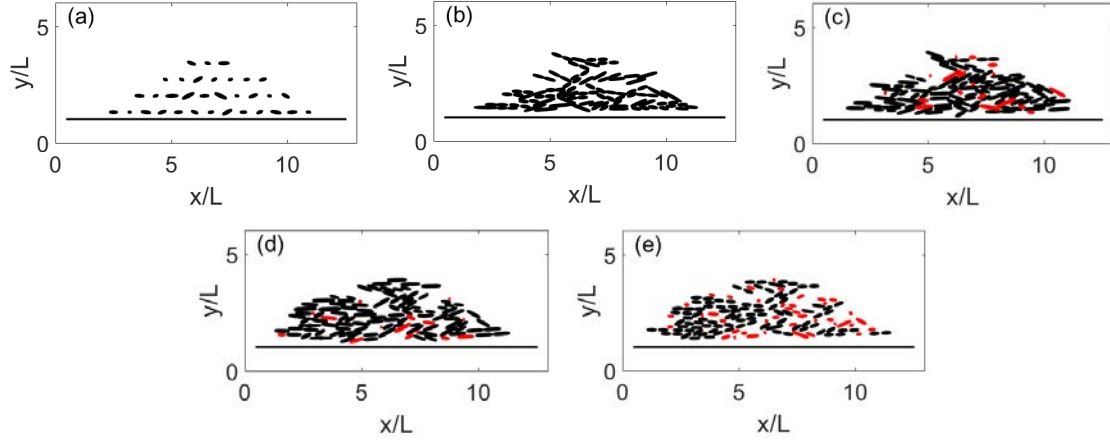


Figure 4.16: (a) Initial arrangement. Evolution at (b) $t = 10$ h, (c) $t = 14$ h, (d) $t = 18$ h, (e) $t = 20$ h. The simulation starts with 33 cells and ends with 96 cells alive, 41 dead and 75 erased, see Video6.

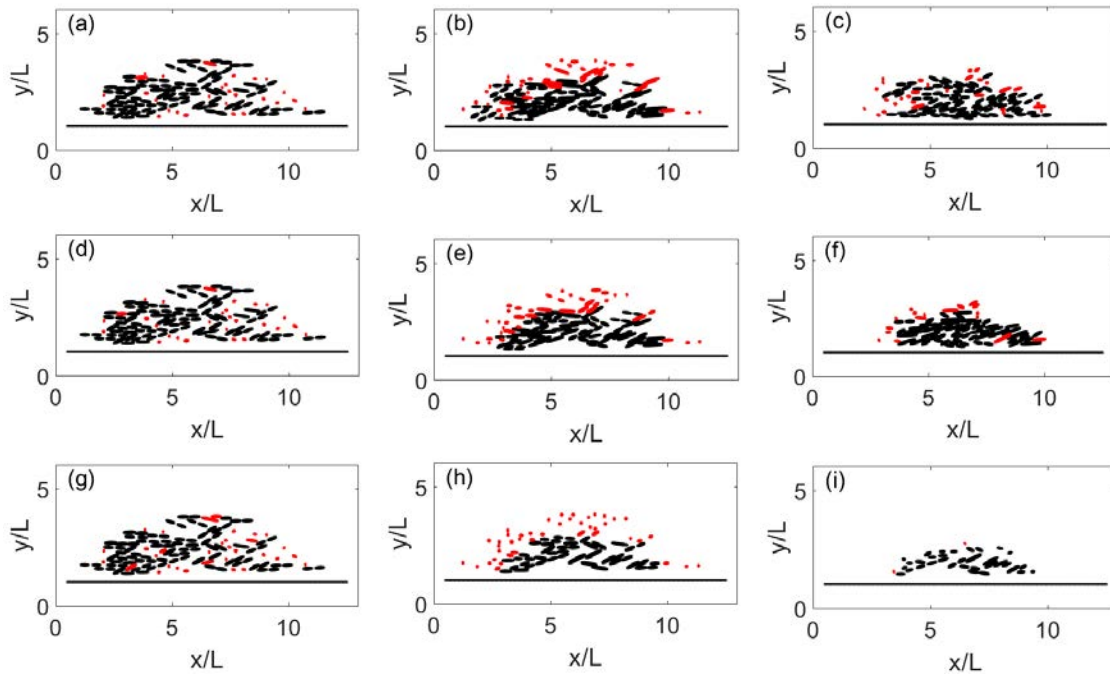


Figure 4.17: Evolution of the final configuration reached in Figure 4.16 under the action of antibiotics. Snapshots for $C_{out} = 3$ at (a) $t = 1$ h, (b) $t = 4$ h, and (c) $t = 10$ h. The simulation ends with 84 cells alive, 29 dead (red) and 108 erased, see Video6a. Snapshots for $C_{out} = 7$ at (d) $t = 1$ h, (e) $t = 4$ h, and (f) $t = 10$ h with 58 alive, The simulation ends with 17 cells dead (red) and 115 erased, see Video6b. Snapshots for $C_{out} = 30$ at (g) $t = 1$ h, (h) $t = 3.5$ h, and (i) $t = 10$ h. The simulation ends with 33 cells alive, 2 dead (red) and 105 erased, see Video6c.

All of this affects the critical distance s_{p2} . All cells tend to be more or less equal apart.

Removing dimensions, the interaction force is as follows:

$$\mathbf{F}_i = \sum_{j=1}^N \sum_{n=1, n \neq j}^N \sigma_{b,0} e^{-\frac{d_{jn}^2}{l_{sp}}} \delta_j \mathbf{n}_{cm,n,j}, \quad (4.47)$$

where $\sigma_b = \sigma_{b,0} L E_s = 20 E_s$, so $\sigma_{b,0} = 20/L$. And $\tilde{l}_{sp}(t_1) = l_{sp}(t_1)/L^2$. We drop the symbol \sim for ease of notation. Parameters are collected in Table 4.8.

For rods there is anisotropy, the vertical direction being different from the horizontal one. We set

$$s_{p2} = t \frac{s_{p,m}}{T_m}, \quad (4.48)$$

where $\frac{s_{p,m}}{T_m}$ is the slope to which the distance with respect to time ascends. We do not have to change the force because the interaction in one plane and the other are similar, the only difference being the growth of the distance. Removing dimensions

$$s_{p2} = t_2 \frac{s_{pm,0}}{T_{pm,0}}. \quad (4.49)$$

In either case, spheres or rods, we set $s_l = s_{p2}$ in the flowchart.

$s_{max,0} = \frac{s_{max}}{L}$	$l_{m,0} = -\frac{s_{max}^2}{\ln(v_{min})L^2}$	$T_{p,0} = \frac{T_p}{\tau dt_2}$	v_{min}
0.04	$-\frac{1.6 \times 10^{-3}}{\ln(v_{min})}$	$\frac{6.5}{dt_2}$	$\frac{dt_2}{2dt_1 \lambda_0 \sigma_{b,0}}$
$s_{pm,0} = \frac{s_{pm}}{L}$	$T_{pm,0} = \frac{T_{pm}}{\tau dt_2}$	$v_{s,0} = \tau v_s$	
0.04	$\frac{11}{dt_2}$	5×10^{-3}	

Table 4.8: Additional parameters for the simulations in the presence of an horizontal barrier.

In this second geometry, nutrients flow to bacteria from the bottom, through the horizontal immersed boundary on top of which they grow, whereas toxicants flow from the top. As for the initialization, besides the N immersed boundaries representing bacteria, we include a lower barrier which does not touch the borders of the computational region. Boundary conditions for concentrations change. We fix Dirichlet boundary conditions for S and C_e on the lower computational border, and on the lateral ones up to the height of the horizontal immersed boundary. Zero Neumann boundaries are imposed on the rest. For C_{out} , the situation is reversed. Zero Neumann boundary conditions on the lower part, and Dirichlet on the upper one.

Figures 4.14 and 4.15 illustrate the evolution in the case of spherical bacteria, with and without antibiotics. Notice the formation of inner gaps or channels in the structure, in agreement with (Wilking et al. 2013). These computational studies allow us to investigate porosity variations in the inner structure, as well as the formation of inner gaps due to cell death and reabsorption which eventually fill with fluid. When antibiotics are added, an outer necrotic region which is finally erased appears too. Figures 4.16 and 4.17 illustrate the evolution in the case of rod-like bacteria.

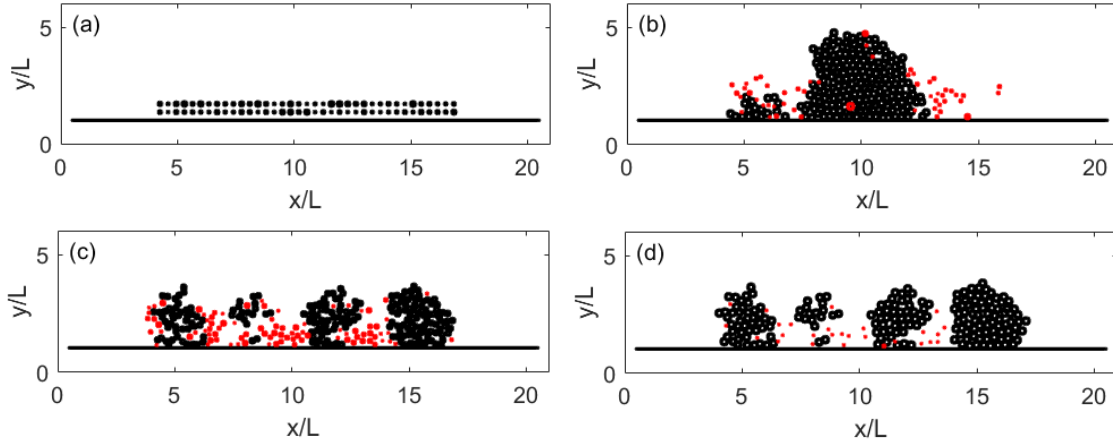


Figure 4.18: Irregular patterns formed lowering nutrients/consumption. (a) Initial arrangement, with 74 cells. (b) Configuration at $t = 47.5$ h, for $\nu^*/K_S = 2.35 \times 10^{-3}$ (same values as before). (c) Same as (b) for $\nu^*/K_S = 2.08 \times 10^4$. (d) Evolution of (c) at $t = 50.5$ h, showing finger formation.

Figure 4.18 considers a slightly different configuration in which nutrients flow from the top, in the absence of toxicants, the interaction force is the same as the top view, and the critical distance is always zero. Notice the formation of fingers due to scarceness of resources, in agreement with previous observations (Purevdorj et al. 2002; Hermanowicz 2001). Figure 4.19 represents contour curves for substrate and toxicant fields. The geometrical arrangement and the number of bacteria influence the contours, compare panel (b) with 367 cells to (c) with 72. Also, the behavior of the fluid flow undergoes variations. While in the free spread configuration velocities remain very small, in the barrier configuration velocities increase locally around dense areas, influencing cell groupings.

4.6 Biofilm extinction

In this Section, we consider the possibility of driving a biofilm to extinction by an adequate combination of antibiotics (Højby et al. 2010). The death criterion we employed in the previous sections allows the biofilm to grow but it prevents the total number of bacteria from dropping below the initial value. For decaying biofilms, the death criterion used in (Birbir et al. 2018) is more adequate: we kill a cell \mathbf{X}_j when $p_j < r \frac{N_a}{N_{init}}$, being N_{init} the number of bacteria just before administering the antibiotics. In Figure 4.20, we revisit simulations (a)-(c) and (d)-(f) from Figure 4.7 with this new criterion. Clinical tests (Højby et al. 2010) point out the convenience of combining antibiotics targeting different types of cells within the biofilm to be able to eradicate them. We consider here a cocktail of two antibiotics. One of them targets dormant cells with little energy, which are located in the inner biofilm core (the antibiotic colistin, for instance). We represent that effect using a toxicity coefficient $k_{tox,1,j}$ which decreases with the cell energy. The other one targets cells with high energy, which divide actively, and tend to be located in

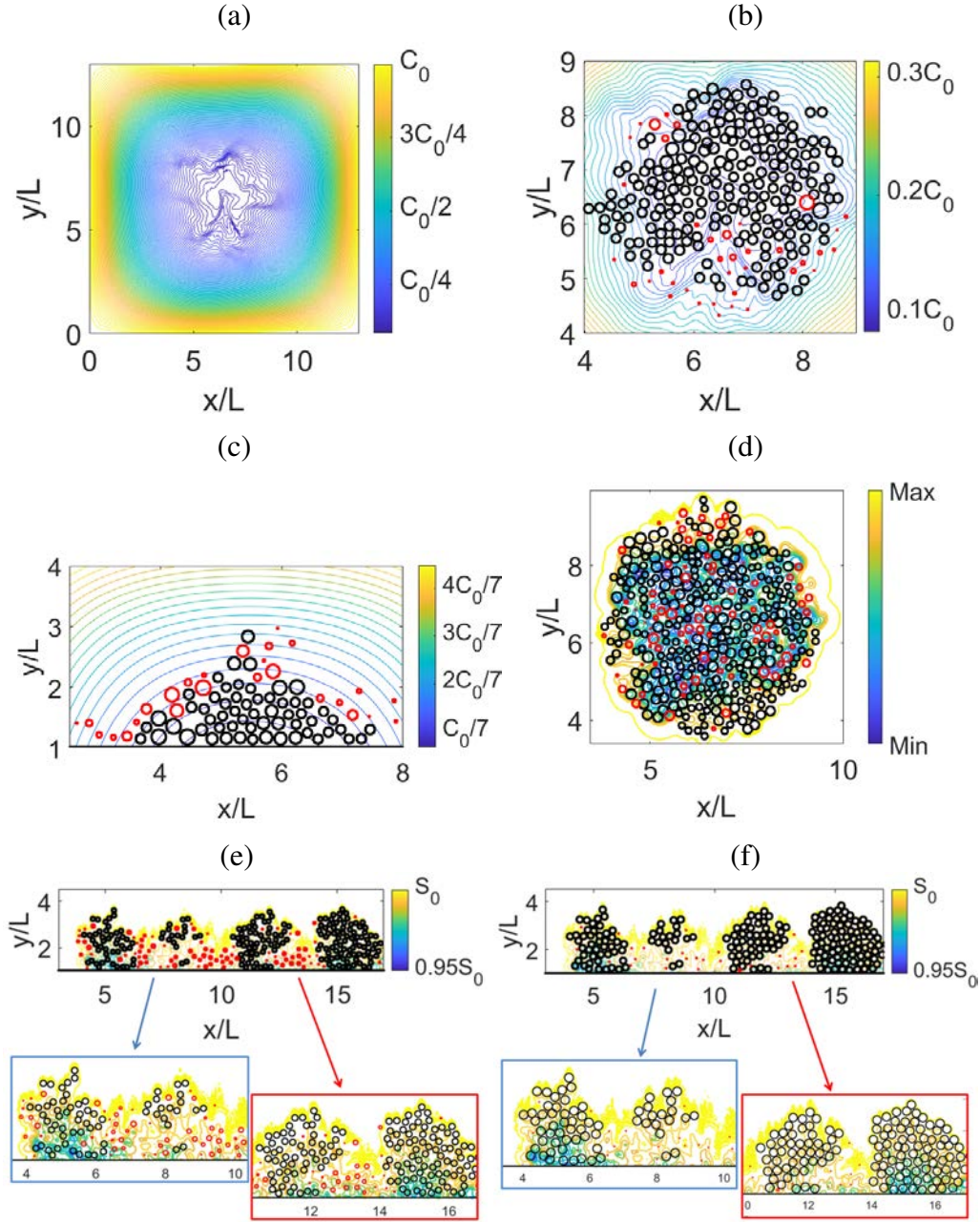


Figure 4.19: Contour fields for substrate and toxicant: (a)-(b) are toxicant contour fields for figure 4.8(f). (c) Toxicant contour field for figure 4.15(e). (d) Substrate contours for figure 4.7(e), $\text{Max} = S_0 = 10$ and $\text{Min} = 0.99999997S_0$. (e)-(f) Substrate contours for figure 4.18(c)-(d).

the outer biofilm regions (penicillins, for instance). We represent that effect by a toxicity coefficient $k_{tox,2,j}$ which increases with the cell energy. More precisely, we have used the following expression

$$k_{tox,1,j} = k_{tox} e^{10(e_m - e_j)}, \quad k_{tox,2,j} = k_{tox} e^{10(e_j - e_m)}, \quad e_m = 0.5. \quad (4.50)$$

We modify the model to include two equations similar to (4.40) for the antibiotic concentration with toxicity coefficients (4.50) and the corresponding two equations (4.35) for the

antibiotic concentration inside the cells. Also, we set $C_{out} = C_{out,1} + C_{out,2}$ in the definition of (4.30) for ν' and replace in eq. (4.32) the term $k_{tox}C_{in,j}$ by $k_{tox,1,j}C_{in,1,j} + k_{tox,2,j}C_{in,2,j}$. Revisiting the simulations in Figure 4.7 with these new choices, we are able to drive the biofilm to extinction, see Figure 4.20 (g)-(i). These simulations reproduce behaviors experimentally observed, compare to Fig. 6 in Reference (Høiby et al. 2010).

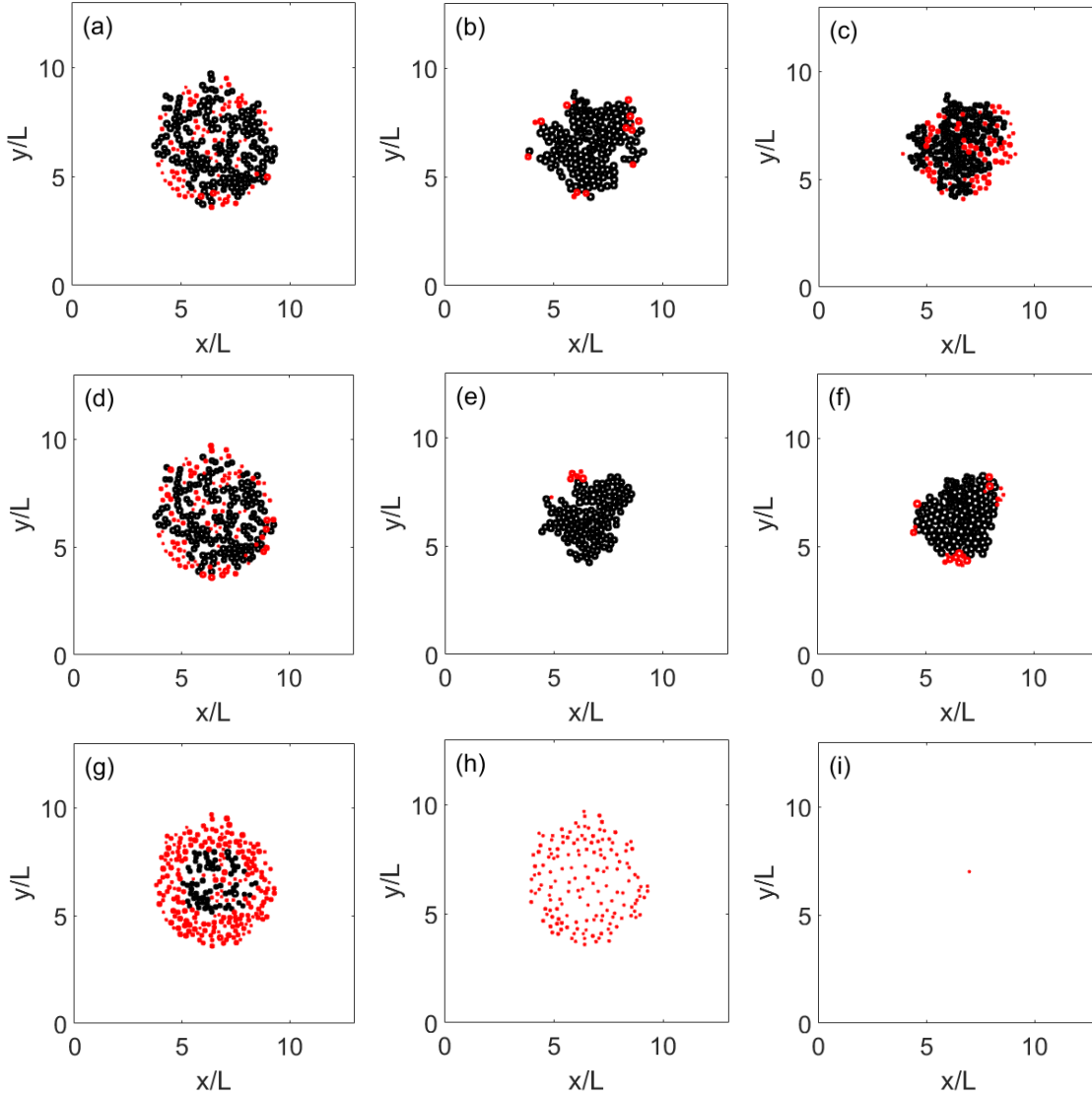


Figure 4.20: Equivalent of snapshots (a)-(c) and (d)-(f) with the modified death criterion: (a), (d), (g) $t = 2.5$ h, (b), (e), (h) $t = 8.5$ h, and (c), (f), (i) $t = 10$ h. Snapshots (a)-(c) for $C_{out} = 3$ end with 184 cells alive, 66 dead (red) and 320 erased, see Video7. Snapshots (d)-(f) for $C_{out} = 7$ end with 141 cells alive, 20 cells (red) and 327 erased, see Video8. Finally, panels (g)-(i) represent the extinction of the same initial configuration with the modified death criterion and a combination of two antibiotics with $C_{out} = 3$ and variable k_{tox} . The simulation ends with 0 cells alive, 1 dead (red) and 385 erased, see Video9.

4.7 Summary

This chapter presents a model for bacterial biofilms that includes the geometry of the individual bacterium, a polymeric matrix, a fluid and the concentrations belonging to the environment. We have successfully modelled the interactions of bacteria of two different geometries, spherical and rod-like. We have recreated the biofilm in a two-dimensional plane with a top view, and from the front with a barrier simulating the surface.

Death probability fluctuates locally according to availability of resources and space. When we introduce the antibiotic, small necrotic zones are generated around the biofilm. In this way the core of the biofilm remains intact and protected because the necrotic regions act as a shield. The model captures antibiotic resistance intrinsically. In addition, the model also contains experimentally found patterns such as the rod-like alignment of the bacteria and the voids generated by the fluid within the biofilm in the front view. On the other hand, we have been able to model up to just over 1100 cells.

Other interesting things about the model is the possible simulation of a competition between bacterial types. In this case we have represented a competition between spherical bacteria and rod-like bacteria. We have seen that the rod bacteria capture more nutrients by generating more agents than the other type, and that they take up more space than the other type. So in our model the rod bacteria are dominant. We also controlled the amount of nutrients to observe two different biofilm growths. With many nutrients we find a single compact biofilm, and with few nutrients, a dispersion of regions with bacteria and others without bacteria is generated, recreating a separate biofilm in different clusters. Another interesting result is the control of antibiotics in order to extinguish the biofilm. By adding two types of antibiotics, one for the more energetic bacteria such as penicillins, and another for the less energetic bacteria such as colistin, we can extinguish the biofilm as in experiments.

Overall conclusions

In this thesis we have addressed two important issues of the collective behavior of biological aggregates. Qualitative features and power laws in swarms of male midges and spreading bacterial biofilms and their response to environmental modifications. In this chapter we write our final conclusions and comments on the most relevant results of each research.

Scale free chaos and midges swarms

The first main result of this thesis is the discovery of a hitherto unsuspected and unexplored phase transition of free scale chaos in the harmonically confined 3D Vicsek model. This result is discussed in Chapters 2 and 3 and it is based on our publication (González-Albaladejo et al. 2023). The harmonically confined Vicsek model (HCVM) also exhibits a different phase transition to clusters of finite size containing infinitely many particles, which we have called flocking black holes. Our work is motivated by observations of natural midge swarms and of swarms in the laboratory, which comprise at most hundreds of insects and form about a marker (Attanasi, Cavagna, L. D. Castello, et al. 2014; Attanasi, Cavagna, L. Del Castello, et al. 2014; Cavagna, Conti, et al. 2017; Kelley et al. 2013; Gorbosnos et al. 2016; Sinhuber et al. 2017). The main conclusions and novel aspects of the work on insect swarms are as follows.

I. For finitely many particles, the 3D HCVM exhibits periodic, quasiperiodic and chaotic attractors modified by the alignment noise. The control parameters for the model are confinement and noise. As confinement decreases, there is a region of chaotic attractors characterized by positive values of the largest Lyapunov exponent. Depending on the magnitude of the noise, chaos is either deterministic, noisy, or swamped by noise, de-

pending on the noise strength. The scale-dependent Lyapunov exponent decides the type of chaotic attractor (Gao, Hu, et al. 2006), as explained in Chapter 2, which also explains the Benettin and other algorithms used to calculate Lyapunov exponents (Benettin et al. 1980; Gao and Zheng 1994).

II. Inside the region of noisy chaos and for N particles, there is a line of confinement versus noise that separates single cluster from multicluster chaos. These different attractors can be distinguished using topological data analysis (González-Albaladejo et al. 2023), as explained in Chapter 2. More quantitatively, we adopt in Chapter 3 the definitions of dynamic and static correlation functions used by (Attanasi, Cavagna, L. D. Castello, et al. 2014; Cavagna, Conti, et al. 2017; Cavagna, Giardina, et al. 2018) to calculate critical lines and critical exponents from experimental observations of natural swarms. These definitions are adapted from those in equilibrium phase transitions (Amit et al. 2005; Halperin et al. 1969). The critical line is found by finding the minimum of the correlation time. On it, the correlation length is proportional to the swarm size, which means that chaos is scale free on the critical line. Using the finite size hypothesis, we calculate power laws and critical exponents from numerical simulations with increasing values of N . Close to the critical line, we find another line on which the static correlation function has an inflection point and the largest Lyapunov exponent is maximal. Both critical lines collapse onto zero confinement as N goes to infinity, thereby indicating that they correspond to the same phase transition, which we call scale-free-chaos phase transition. We find the dynamic critical exponent and critical exponents for the correlation length, susceptibility and largest Lyapunov exponent in terms of confinement. They are compatible with known measured values for natural swarms.

The conventional way to finding a critical line using finite size scaling is to follow the maxima of the susceptibility calculated from the static correlation function. For the HCVM, there are local maxima inside the region of noisy chaos and global maxima. The local maxima disappear when we subtract overall rotation and dilation when calculating correlation functions. The global maxima correspond to a different phase transition. Thus, we have used the correlation time and the inflection point of the susceptibility, which are the same whether we carry out subtractions or not.

III. In Chapter 3, we have found a different phase transition at the global maxima of the susceptibility that is characterized by the formation of clusters of finite correlation length admitting an ever increasing number of particles (the flocking black holes, (González-Albaladejo et al. 2023)). This phase transition is akin to gravitational collapse (Chavanis et al. 2020).

IV. *Qualitative features captured by the HCVM.* In addition to reasonable critical exponents, the scale-free-chaos phase transition produces disperse chaotic swarms below the critical line that are confined to a bounded region of space with a few particles entering and leaving the nucleus of the swarm, cf. Fig. 2.4. This is akin to the observed condensed and vapor phases of natural swarms (Sinhuber et al. 2017). Furthermore, as

shown in Section 3.2, the normalized dynamic correlation function coalesce to a single curve as a function of $k_c^z t$ for an interval $0 < k_c^z t < 4$ (cf. Fig. 3.1), which is similar to that observed in natural swarms (Fig. 2b of (Cavagna, Conti, et al. 2017)). Moreover, the flatness values given in Chapter 3 are compatible with those observed in natural swarms (Cavagna, Conti, et al. 2017). Observations of midges in the laboratory indicate that the center of mass of their swarm moves almost randomly (Kelley et al. 2013; Ni, Puckett, et al. 2015), following Lévy flights (Reynolds and Ouellette 2016). To this respect, the connection between chaos and Lévy flights in animal search patterns is intriguing (Reynolds, Bartomeus, et al. 2016) and could indicate that noisy chaos is indeed present in midge swarms. These similitudes to experimental observations and the involved theoretical challenges make worthwhile exploring more fully the confined Vicsek model and the phase transition we have discovered.

This work paves the way to studies in many directions. Possible directions consist of exploring other possible transitions on chaotic and non-chaotic windows of the parameter space and the effect of anisotropic confinement on the phase transition studied here. Exploring a possible phase transition to flocking black holes in self-gravitating models of swarms (Gorbonos et al. 2016) might be worth pursuing. On the theoretical side, can we find the invariant measure of the chaotic attractors and characterize scale-free-chaos phase transitions as $N \rightarrow \infty$ in terms of the invariant measure? This could bring together dynamical systems and nonequilibrium statistical mechanics studies and yield fruitful new ideas and methods. Another interesting research venue is to explore the connection between our topological data analysis characterization of the scale-free-chaos phase transition in Chapter 2 and the topological characterization of equilibrium phase transitions as geometrical changes in underlying manifolds (Franzosi et al. 2007a; Franzosi et al. 2007b; G. Pettini et al. 2019; Gori, Franzosi, G. Pettini, et al. 2022).

Biofilms

Studying the dynamics of cellular aggregates such as bacterial biofilms faces the challenge of dealing with complicated geometries and interactions. Many approaches have been proposed to that effect, with advantages and disadvantages. Cellular automata allow us to represent many microscopic and macroscopic processes (Laspidou et al. 2014; Carpio, Cebrián, and Vidal 2019), but ignore bacterial shapes and interactions. Individual based models seem effective for large biofilms growing in flows (Lardon et al. 2011), but become exceedingly complicated for biofilms spreading on surfaces as the ones we consider here (Storck et al. 2014; Grant et al. 2014). Immersed boundary methods provide a very flexible alternative to study mechanical interactions in these complex geometries (Dillon, Fauci, et al. 1996; Li et al. 2012; Rejniak 2007). Here, the immersed boundaries provide the basic geometrical skeleton, while the interaction with the medium is represented by forces governed by a set of equations coupling metabolic and physico-chemical processes. Cell growth, division, and death, is managed through additional rules on the evolution of

the discrete boundaries. Unlike previous IB approaches to multicellular tissues, we do not include heuristical sources. Boundaries move as a result of cellular activity as dictated by a dynamic energy budget model, letting flow in and out through them.

We have applied our model to reproduce initial stages of the spread of a biofilm seed formed by a few spherical or/and rod-like bacteria in two dimensional geometries. Simulating rod-like bacteria is more expensive computationally. Computing the interactions of rods requires small steps to let configurations adapt as cells grow and divide, avoiding overlaps. We observe that rod-like bacteria tend to align, which is in agreement with experimental observations (Kirsch 2017; Seminara et al. 2012). In spatial competition with spherical bacteria, rods dominate. In radial horizontal views, we see how crowded areas trigger the death of scattered bacteria, which are reabsorbed. For vertical slices expanding on an horizontal barrier, we see also gaps created by death bacteria near the barrier. In this case, we have implemented a mechanism to allow water flow inside the biofilm, so that gaps are filled with fluid and the separation between bacteria increases. When antibiotics are applied, bacteria located in the borders are first to die, forming small necrotic regions. We have shown that combining antibiotics which target either active or dormant cells within the layered biofilm structure we are able to drive the biofilm to complete extinction, in agreement with experimental observations (Høiby et al. 2010). We also observe the formation of fingering interfaces varying the uptake rates and nutrients.

The specific results of the simulations depend on the parameters we choose. Most of parameters appearing in the model equations are taken from experimental measurements and fittings to population counts for some bacteria (Seminara et al. 2012; Tuson et al. 2012; Klanjscek et al. 2012; Birnir et al. 2018). However, there are a number of parameters in the representation of interaction forces, division and death criteria which are selected to produce adequate results, avoiding artifacts. Whether the whole set of parameters can be fitted to data counts for the time evolution of biofilm seeds of bacteria deserves further research. From a practical point of view, it would be important to be able to implement control strategies using the antibiotic supply as control variables to extinguish the whole biofilm seed in finite time.

Our model has more spatial resolution compared to cellular automata or particle based modeling traditional techniques because we can capture individual cell deformation and cell-fluid interactions. We can study geometrical arrangements, for instance, we identify a tendency to align of rod-like bacteria, which might have consequences for the microstructure and emerging behaviors of biofilms. Also, we observe the formation of inner gaps (due the cell death and reabsorption) which fill with fluid, resulting in porous structures conditioned by geometrical interactions between cells and possible barriers, in agreement with experiments (Asally et al. 2012; Seminara et al. 2012; Wilking et al. 2013).

The present framework is useful to investigate incipient stages of biofilm evolution and how to eradicate or prevent them in those stages. However, it is computationally expensive if one intends to grow large numbers of cells to see emerging behaviors at larger

scales, eventually coupling to macroscopic mechanical descriptions (Carpio, Cebrián, and Vidal 2019). This burden would be reduced resorting to High Performance Computing networks or exploiting GPUs to speed up the process and allow for an increasing number of cells.

Bibliography

- Alberti, G. and P.H. Chavanis (2020). “Caloric curves of classical self-gravitating systems in general relativity”. In: *Phys. Rev. E* 101, p. 052105.
- Amit, D. J. and V. Martin-Mayor (2005). *Field theory, the renormalization group and critical phenomena*. World Scientific, Singapore.
- Asally, M. et al. (2012). “Localized cell death focuses mechanical forces during 3D patterning in a biofilm”. In: *Proc. Natl. Acad. Sci. USA* 109, p. 18891.
- Attanasi, A., A. Cavagna, L. D. Castello, et al. (2014). “Finite-Size Scaling as a Way to Probe Near-Criticality in Natural Swarms”. In: *Phys. Rev. Lett.* 113, p. 238102.
- Attanasi, A., A. Cavagna, L. Del Castello, et al. (2014). “Collective Behaviour without Collective Order in Wild Swarms of Midges”. In: *PLoS Comput. Biol.* 10.7, e1003697.
- Be’er, A. et al. (2015). “A phase diagram for bacterial swarming”. In: *Annual Review of Condensed Matter Physics* 3.66.
- Benettin, G. et al. (1980). “Lyapunov Characteristic Exponents for smooth dynamical systems and for hamiltonian systems; a method for computing all of them. Part 2: Numerical application”. In: *Meccanica* 15, pp. 21–30.
- Bertin, E., M. Droz, and G. Grégoire (2006). “Boltzmann and hydrodynamic description for self-propelled particles”. In: *Phys. Rev. E* 74, p. 022101.
- (2009). “Hydrodynamic equations for self-propelled particles: microscopic derivation and stability analysis”. In: *J. Phys. A: Math. Theor* 98, p. 445001.
- Birnir, B. et al. (2018). “Dynamic energy budget approach to evaluate antibiotic effects on biofilms”. In: *Commun Nonlinear Sci Numer Simulat* 54, pp. 70–83.
- Bohr, T. (1990). “Chaos and turbulence”. In: *Applications of Statistical and Field Theory Methods to Condensed Matter*. Ed. by D. Baeriswyl, A. R. Bishop, and J. Carmelo. Plenum, New York.
- Bonilla, L. L. (1988). “Two nonequilibrium phase transitions: Stochastic Hopf bifurcation and onset of relaxation oscillations in the diffusive sine-Gordon model”. In: *Far*

- from equilibrium phase transitions*. Ed. by L. Garrido. Lecture Notes in Physics 319, Springer, Berlin.
- Bonilla, L. L. and A. Liñán (1984). “Relaxation oscillations, pulses and traveling waves in the diffusive Volterra delay-differential equation”. In: *SIAM Journal on Applied Mathematics* 44, pp. 369–391.
- Bonilla, L. L. and C. Trenado (2018). “Crossover between parabolic and hyperbolic scaling, oscillatory modes and resonances near flocking”. In: *Phys. Rev. E* 98, p. 062603.
- (2019). “Contrarian compulsions produce exotic time-dependent flocking of active particles”. In: *Phys. Rev. E* 99, p. 012612.
- Bulashenko, O. M. et al. (1999). “Multifractal dimension of chaotic attractors in a driven semiconductor superlattice”. In: *Phys. Rev. B* 60, pp. 5694–5697.
- Carpio, A. and E. Cebrián (2020). “Incorporating cellular stochasticity in solid-fluid mixture biofilm models”. In: *Entropy* 22, p. 188.
- Carpio, A., E. Cebrián, and P. Vidal (2019). “Biofilms as poroelastic materials”. In: *International Journal of Non-Linear Mechanics* 109, pp. 1–8.
- Carpio, A. and R. González-Albaladejo (2022). “Immersed Boundary approach to biofilm spread on surfaces”. In: *Communications in Computational Physics* 31, pp. 257–292.
- Cavagna, A., L. Di Carlo, I. Giardina, T. S. Grigera, S. Melillo, et al. (2021). “Natural Swarms in 3.99 Dimensions”. In: *arXiv:2107.04432*.
- Cavagna, A., L. Di Carlo, I. Giardina, T. S. Grigera, and G. Pisegna (2021). “Equilibrium to off-equilibrium crossover in homogeneous active matter”. In: *Phys. Rev. Res.* 3, p. 013210.
- Cavagna, A., D. Conti, et al. (2017). “Dynamic scaling in natural swarms”. In: *Nat. Phys.* 13.9, pp. 914–918.
- Cavagna, A., I. Giardina, and T.S. Grigera (2018). “The physics of flocking: Correlation as a compass from experiments to theory”. In: *Phys. Rep.* 728, pp. 1–62.
- Cencini, M., F. Cecconi, and A. Vulpiani (2010). *Chaos. From simple models to complex systems*. World Scientific, New Jersey.
- Chai, L., H. Vlamakis, and R. Kolter (2011). “Extracellular signal regulation of cell differentiation in biofilms”. In: *MRS Bulletin* 36, pp. 374–379.
- Chaté, H. (2013). “Dry aligning dilute active matter”. In: *Ann. Rev. Cond. Matter Phys.* 85, pp. 189–212.
- Chaté, H. and B. Mahault (2019). “Dry, aligning, dilute, active matter: A synthetic and self-contained overview”. In: *arXiv:1906.05542*.
- Chavanis, P.H. and G. Alberti (2020). “Gravitational phase transitions and instabilities of self-gravitating fermions in general relativity”. In: *Phys. Lett. B* 801, p. 135155.
- Chen, L., C. F. Lee, and J. Toner (2018). “Incompressible polar active fluids in the moving phase in dimensions $d > 2$ ”. In: *New J. Phys.* 20, p. 113035.
- Chen, L., J. Toner, and C. F. Lee (2015). “Critical phenomenon of the order-disorder transition in incompressible active fluids”. In: *New J. Phys.* 17, p. 042002.
- Ciofu, o. et al. (2022). “Tolerance and resistance of microbial biofilms”. In: *Nat Rev Microbiol* 20, pp. 621–635.

- Costerton, J. W. et al. (1995). “Microbial Biofilms”. In: *Annual Review of Microbiology* 49.1, pp. 711–745.
- Cross, M. C. and P. C. Hohenberg (1993). “Pattern formation outside of equilibrium”. In: *Rev. Mod. Phys.* 65, pp. 851–1112.
- Dangelmayr, G. and E. Knobloch (1987). “The Takens-Bogdanov bifurcation with $O(2)$ -symmetry”. In: *Phil. Trans. R. Soc. Lond. A.* 322, pp. 243–279.
- De Gennes, P. G. (1974). “Coil-stretch transition of dilute flexible polymers under ultra-high velocity gradients”. In: *J. Chem. Phys.* 60, p. 5030.
- (1991). “Soft matter”. In: *Nobel Lecture*.
- Dillon, R., L. Fauci, et al. (1996). “Modeling biofilm processes using the immersed boundary method”. In: *Journal of Computational Physics* 129, pp. 57–73.
- Dillon, R., M. Owen, and K. Painter (2008). “A single-cell-based model of multicellular growth using the immersed boundary method”. In: *Moving Interface Problems and Applications in Fluid Dynamics*. Ed. by B. C. Khoo, Z. Li, and P. Lin. (Contemporary Mathematics). American Mathematical Society.
- Drescher, K. et al. (2013). “Biofilm streamers cause catastrophic disruption of flow with consequences for environmental and medical systems”. In: *Proc. Natl. Acad. Sci. USA* 35, pp. 4345–4350.
- Edelsbrunner, H. and J. Harer (2010). *Computational Topology: An Introduction*. American Mathematical Society.
- Einstein, A. (1905). “Über die von der molekularkinetischen Theorie der Wärme geforderte Bewegung von in ruhenden Flüssigkeiten suspendierten Teilchen”. In: *Ann. Phys.* 322, pp. 549–560.
- Flemming, H. C. et al. (2016). “Biofilms: an emergent form of bacterial life”. In: *Nature Reviews Microbiology* 14, pp. 563–575.
- Flemming, H.C. and J. Wingender (2010). “The biofilm matrix”. In: *Nat. Rev. Microbiol.* 8, pp. 623–633.
- Franzosi, R., M. Pettini, and L. Spinelli (2007a). “Topology and phase transitions I. Preliminary results”. In: *Nucl. Phys. B* 782, pp. 189–218.
- (2007b). “Topology and phase transitions II. Theorem and a necessary relation”. In: *Nucl. Phys. B* 782, pp. 219–240.
- Gao, J. B., J. Hu, et al. (2006). “Distinguishing chaos from noise by scale-dependent Lyapunov exponent”. In: *Phys. Rev. E* 74, p. 066204.
- Gao, J. B. and Z. M. Zheng (1994). “Direct dynamical test for deterministic chaos and optimal embedding of a chaotic time series”. In: *Phys. Rev. E* 49, pp. 3807–3814.
- Glimm, J. and A. Jaffe (1987). *Quantum Physics. A Functional Integral Point of View*. Springer.
- González-Albaladejo, R., A. Carpio, and L. L. Bonilla (2023). “Scale free chaos in the confined Vicsek flocking model”. In: *Phys. Rev. E* 107, p. 014209.
- Gorbonos, D. et al. (2016). “Long-range acoustic interactions in insect swarms: an adaptive gravity model”. In: *New J. Phys.* 18, p. 073042.

- Gori, M., R. Franzosi, G. Pettini, et al. (2022). “Topological theory of phase transitions”. In: *J. Phys. A: Math. Theor.* 55, p. 375002.
- Gori, M., R. Franzosi, and M. Pettini (2018). “Topological origin of phase transitions in the absence of critical points of the energy landscape”. In: *J. Stat. Mech.* 2018, p. 093204.
- Grant, M. A. A. et al. (2014). “The role of mechanical forces in the planar-to-bulk transition in growing *Escherichia coli* microcolonies”. In: *J. R. Soc. Interface* 11, p. 20140400.
- Grassberger, P. and I. Procaccia (1983). “Measuring the strangeness of strange attractors”. In: *Physica D* 9, pp. 189–208.
- Grégoire, G. and H. Chaté (2004). “Onset of Collective and Cohesive Motion”. In: *Phys. Rev. Lett.* 92, p. 025702.
- Gundlach, C. and J. M. Martín-García (2007). “Critical Phenomena in Gravitational Collapse”. In: *Living Rev. Relativity* 10.5.
- Hale, J. K. (1977). *Theory of Functional Differential Equations*. Springer.
- Halperin, B. I. and P. C. Hohenberg (1969). “Scaling laws for dynamic critical phenomena”. In: *Phys. Rev.* 177, pp. 952–971.
- Hermanowicz, S.W. (2001). “A simple 2D biofilm model yields a variety of morphological features”. In: *Mathematical Biosciences* 169, pp. 1–14.
- Højby, N. et al. (2010). “Antibiotic resistance of bacterial biofilms”. In: *Int J Antimicrob Agents* 35, pp. 322–332.
- Holubec, V. et al. (2021). “Finite-Size Scaling at the Edge of Disorder in a Time-Delay Vicsek Model”. In: *Phys. Rev. Lett.* 127, p. 258001.
- “How bird flocks are like liquid helium” (2014). In: URL: <https://www.science.org/content/article/how-bird-flocks-are-liquid-helium>.
- Huang, K. (1987). *Statistical Mechanics*. Wiley, NY.
- Huxley, J. S. (1912). *The individual in the animal kingdom*. Cambridge University Press.
- Ihle, T. (2011). “Kinetic theory of flocking: Derivation of hydrodynamic equations”. In: *Phys. Rev. E* 83, 030901(R).
- “Insect Swarms Go Critical” (2014). In: URL: <https://physics.aps.org/articles/v7/120>.
- Isaacson, E. and H.B. Keller (1994). *Analysis of Numerical methods*. Dover.
- Ishida, H. et al. (1998). “In vivo and in vitro activities of levofloxacin against biofilm producing *Pseudomonas aeruginosa*, antimicrob”. In: *Agents Chemother* 42, pp. 1641–5.
- Kabsch, W. (1976). “A solution for the best rotation to relate two sets of vectors”. In: *Acta Cryst. A* 32, pp. 922–923.
- Kastner, M. and D. Mehta (2011). “Phase transitions detached from stationary points of the energy landscape”. In: *Phys. Rev. Lett.* 107, p. 160602.
- Kelley, D. H. and N. T. Ouellette (2013). “Emergent dynamics of laboratory insect swarms”. In: *Sci. Rep.* 3, p. 1073.
- Kirsch, D. (2017). “This bacterial discovery could prevent biofilms, Medical Design & Outsourcing”. In: URL: <https://www.medicaldesignandoutsourcing.com/discovery-prevent-biofilms-texas/>.

- Klanjscek, T. et al. (2012). “Modeling physiological processes that relate toxicant exposure and bacterial population dynamics”. In: *PLoS One* 7.2, e26955.
- Kleman, M. and O. D. Lavrentovich (2003). *Soft matter physics : an introduction*. Springer, NY.
- Kooijman, S.A.L.M. (2008). *Dynamic energy budget theory for metabolic organization*. Cambridge University Press.
- Kürsten, R. and T. Ihle (2020). “Dry Active Matter Exhibits a Self-Organized Cross Sea Phase”. In: *Phys. Rev. Lett.* 125, p. 188003.
- Kuznetsov, Y. A. (2004). *Elements of Applied Bifurcation Theory*. Springer, New York.
- Lappin-Scott, H., S. Burton, and P. Stoodley (2014). “Revealing a world of biofilms — the pioneering research of Bill Costerton”. In: *Nat Rev Microbiol* 12, pp. 781–787.
- Lardon, L. A. et al. (2011). “iDynoMiCS: next-generation individual-based modelling of biofilms”. In: *Environ. Microbiol.* 13, pp. 2416–34.
- Laspidou, C. S. et al. (2014). “Material modeling of biofilm mechanical properties”. In: *Math. Biosci.* 251, pp. 11–15.
- Le Bon, G. (1895). *Psychologie des foules*. Germer Baillière, Paris.
- (1897). *The crowd: a study of the popular mind*. London, T. Fisher Unwin.
- Li, Y., A. Yun, and J. Kim (2012). “An immersed boundary method for simulating a single axisymmetric cell growth and division”. In: *Journal of Mathematical Biology* 65, pp. 653–675.
- Long, W. J. (1919). *How animals talk: And other pleasant studies of birds and beasts*. Bear & Co.
- Lopez, U. et al. (2012). “From behavioural analyses to models of collective motion in fish schools”. In: *Interface Focus* 2, pp. 693–707.
- Marchetti, M. C. et al. (2013). “Hydrodynamics of soft active matter”. In: *Rev. Mod. Phys.* 85, pp. 143–1189.
- Miller, R. C. (1921). “The Mind of the Flock”. In: *The Condor* 23, pp. 183–186.
- Miritello, G., A. Pluchino, and A. Rapisarda (2009). “Phase transitions and chaos in long-range models of coupled oscillators”. In: *Europhys. Lett.* 85, p. 10007.
- Ni, R. and N. T. Ouellette (2016). “On the tensile strength of insect swarms”. In: *Phys. Biol.* 13.4.
- Ni, R., J. G. Puckett, et al. (2015). “Intrinsic fluctuations and driven response of insect swarms”. In: *Phys. Rev. Lett.* 115, p. 118104.
- Okubo, A. (1986). “Dynamical aspects of animal grouping: Swarms, schools, flocks, and herds”. In: *Adv. Biophys.* 22, pp. 1–94.
- Okubo, A. and S. A. Levin (2001). *Diffusion and Ecological Problems: Modern Perspective*. Springer, NY.
- Ott, E. (1993). *Chaos in dynamical systems*. Cambridge University Press, Cambridge UK.
- Ouellette, N. T. (2022). “A physics perspective on collective animal behavior”. In: *Phys. Biol.* 19.2.
- Parrish, J. K. and L. Edelstein-Keshet (1999). “Complexity, Pattern, and Evolutionary Trade-Offs in Animal Aggregation”. In: *Science* 284.5411.

- Parsek, M. R. and E.P. Greenberg (2005). “Sociomicrobiology: the connections between quorum sensing and biofilms”. In: *Trends in Microbiology* 13.1, pp. 27–33.
- Pawelzik, K. and H. G. Schuster (1987). “Generalized dimensions and entropies from a measured time series”. In: *Phys. Rev. A* 35, pp. 481–484.
- Peskin, C.S. (2002). “The immersed boundary method”. In: *Acta Numerica* 11, pp. 479–517.
- Peskin, C.S. and D.M. McQueen (1995). “A general method for the computer simulation of biological systems interacting with fluids”. In: *Symposia of the Society for Experimental Biology* 49, pp. 265–76.
- Pettini, G. et al. (2019). “On the origin of phase transitions in the absence of symmetry-breaking”. In: *Physica A* 516, pp. 376–392.
- Puckett, J. G. and N. T. Ouellette (2014). “Determining asymptotically large population sizes in insect swarms”. In: *J. Roy. Soc. Interface* 11, p. 20140710.
- Purevdorj, B., J. W. Costerton, and P. Stoodley (2002). “Influence of Hydrodynamics and Cell Signaling on the Structure and Behavior of *Pseudomonas aeruginosa* Biofilms”. In: *Appl. Environ. Microbiol.* 68, pp. 4457–4464.
- Rejniak, K.A. (2007). “An immersed boundary framework for modelling the growth of individual cells: an application to the early tumour development”. In: *Journal of Theoretical Biology* 247, pp. 186–204.
- Reynolds, A. M., F. Bartomeus, et al. (2016). “Signatures of chaos in animal search patterns”. In: *Sci. Rep.* 6, p. 23492.
- Reynolds, A. M. and N. T. Ouellette (2016). “Swarm dynamics may give rise to Lévy flights”. In: *Sci. Rep.* 6, p. 30515.
- Risler, T., J. Prost, and F. Jülicher (2005). “Universal critical behavior of noisy coupled oscillators: A renormalization group study”. In: *Phys. Rev. E* 72, p. 016130.
- Rodriguez, D., B. Einarsson, and A. Carpio (2012). “Biofilm growth on rugose surfaces”. In: *Phys. Rev. E* 86, p. 061914.
- “Scene-Independent Group Profiling in Crowd” (2014). In: URL: <https://crowdbehaviordotorg.wordpress.com/>.
- Scherberger, John (2018). “Identifying and eradicating biofilm. Steps to eliminate an age-old hazard from the health care environment”. In: *ASHE Health Facilities Management magazine*. URL: <https://www.hfmmagazine.com/articles/3372-identifying-and-eradicating-biofilm>.
- Schuster, H. G. and W. Just (2005). *Deterministic chaos. An introduction*. Wiley-VCH, Weinheim.
- Seminara, A. et al. (2012). “Osmotic spreading of *Bacillus subtilis* biofilms driven by an extracellular matrix”. In: *Proc. Natl. Acad. Sci. USA* 109, pp. 1116–1121.
- Silvertown, Jonathan et al. (2011). “Citizen Science Reveals Unexpected Continental-Scale Evolutionary Change in a Model Organism”. In: *PLOS ONE* 6, e18927.
- Sinhuber, M. and N. T. Ouellette (2017). “Phase Coexistence in Insect Swarms”. In: *Phys. Rev. Lett.* 119, p. 178003.

- Solon, A.P., H. Chaté, and J. Tailleur (2015). “From Phase to Microphase Separation in Flocking Models: The Essential Role of Nonequilibrium Fluctuations”. In: *Phys. Rev. Lett.* 114, p. 068101.
- Storck, T. et al. (2014). “Variable cell morphology approach for individual-based modeling of microbial communities”. In: *Biophysical Journal* 106, pp. 2037–2048.
- Stotsky, J.A. et al. (2016). “Variable viscosity and density biofilm simulations using an immersed boundary method, Part II: Experimental validation and the heterogeneous rheology-IBM”. In: *Journal of Computational Physics* 317, pp. 204–222.
- Sudarsan, R. et al. (2016). “Simulating biofilm deformation and detachment with the immersed boundary method”. In: *Communications in Computational Physics* 19, pp. 682–732.
- Sumpter, D. J. T. (2010). *Collective Animal Behavior*. Princeton University Press.
- Theriault, D. H. et al. (2014). “A protocol and calibration method for accurate multi-camera field videography”. In: *J. Exp. Biol.* 217, pp. 1843–1848.
- Toner, J., Y. Tu, and S. Ramaswamy (2005). “Hydrodynamics and phases of flocks”. In: *Ann. Phys.* 318, p. 170.
- Toner, J. and Y. Tu (1995). “Long-Range Order in a Two-Dimensional Dynamical XY Model: How Birds Fly Together”. In: *Phys. Rev. Lett.* 75, p. 4326.
- Trenado, C., L. L. Bonilla, and A. Marquina (2022). “Bifurcation theory captures band formation in the Vicsek model of flock formation”. In: *arXiv:2203.14238*.
- Tuson, H.H. et al. (2012). “Measuring the stiffness of bacterial cells from growth rates in hydrogels of tunable elasticity”. In: *Mol. Microbiol* 84, pp. 874–891.
- Vicsek, T., A. Czirók, et al. (1995). “Novel type of phase transition in a system of self-driven particles”. In: *Phys. Rev. Lett.* 75, pp. 1226–1229.
- Vicsek, T. and A. Zafeiris (2012). “Collective motion”. In: *Phys. Rep* 517, pp. 71–140.
- Wang, C. (1992). “Physically correct direct lighting for distribution ray tracing”. In: *Graphics Gems III*. Ed. by L. Garrido. Academic Press Professional.
- Wilking, J. N. et al. (2013). “Liquid transport facilitated by channels in *Bacillus subtilis* biofilms”. In: *Proc. Natl. Acad. Sci. USA* 110, p. 848.
- Wilson, D. S. and E. Sober (1989). “Reviving the superorganism”. In: *J. Theor. Biol.* 136.3, pp. 337–356.
- Yeomans, J. M. (1992). *Statistical Mechanics of Phase Transitions*. Oxford Science Publications, Oxford UK.
- Zomorodian, A. and G. Carlsson (2005). “Computing persistent homology”. In: *Discrete Comput. Geom.* 33, pp. 249–274.